Dissertation

submitted to the
Combined Faculty of Natural Sciences and Mathematics
of the Ruperto-Carola-University Heidelberg, Germany
for the degree of
Doctor of Natural Sciences

Put forward by
Shuyuan Hu, MSc.
born in: St. Petersburg

Oral examination: Dec 13th, 2023

Attosecond dynamics of dipole-coupled doubly excited states in helium

Referees: Prof. Dr. Thomas Pfeifer
Dr. Wolfgang Quint

Abstract

Within this work, electron dynamics in atoms are experimentally and numerically investigated on their natural attosecond time scales. To access these dynamics, ultrashort and moderately intense few-cycle laser pulses are superposed with attosecond pulsed radiation in the extreme-ultraviolet spectral region In particular, a bound two-electron wave packet in helium on attosecond time scales was experimentally observed. A novel experiment is presented to simultaneously measure resonant photoabsorption spectra of laser-coupled doubly excited states in helium and the streaked photoelectron spectra. It provides the advantage of obtaining an absolute calibration of the time-delay zero for absorption spectra, where delay-dependent phase information is extracted.

List of Publications

Parts of this work have been published or prepared in the following references:

S. Hu, M. Hartmann, A. Harth, C. Ott, and T. Pfeifer. *Noise effects and the impact of detector responses on the characterization of extreme ultra- violet attosecond pulses.* Appl. Opt. 59 (2020).

S. Hu, Y. He, G. D. Borisova, M. Hartmann, P. Birk, C. Ott, and T. Pfeifer *Extracting relative dipole moments from a laser-driven two-electron wave packet in helium by combining attosecond streaking and transient absorption spectroscopy* (in preparation)

Further publications with own contributions:

G. D. Borisova, P. Belda, S. Hu, P. Birk, V. Stooß, M. Hartmann, D. Fan, R. Moshammer, A. Saenz, C. Ott, and T. Pfeifer. *Laser control of an excited-state vibrational wave packet in neutral H2.* (submitted to Phys. Rev. Lett.)

M. Hartmann, L. Hutcheson, G. D. Borisova, P. Birk, S. Hu, A. Brown, H. Hart, C. Ott, and T. Pfeifer. *Core-resonance lineshape analysis of atoms undergoing strong-field ionization.* J. Phys. B: At. Mol. Opt. Phyis. 55 (2022)

Contents

Chapter 1

Introduction

Science originates from observing fundamental phenomena in nature and summarizing their underlying principles, it is based on evidence that can be observed, measured, and tested. After its development over many years, research has entered the scope of observing events on a smaller and smaller timescale, this in turn provided a deeper understanding of the structure and dynamics of matter.

The 2023 Nobel Prize in Physics was awarded to attosecond science for "experimental methods that generate attosecond pulses of light for the study of electron dynamics in matter". It marks a significant recognition of this field and its contributions to understanding electron dynamics in matter. Attosecond pulses have opened up exciting possibilities for studying ultrafast processes at the quantum level. In this field of research, people are interested in the fastest motions on the microscopic scale. Dynamics, for instance, happening inside the smallest indivisible unit of matter - an atom, is on the timescale of femtoseconds (1 fs = 10^{-15} s) and down to attoseconds (1 as = 10^{-18} s). In Bohr's hydrogen atom, the time it takes for the electron in the ground state orbit to circle around the proton is $\sim$150 attoseconds. To have a more intuitive perspective, one can compare it to the age of the universe - estimated to be approximately 13.8 billion years, which is equivalent to approximately 4.35×10^{17} seconds. Just as the age of the universe is incomprehensibly vast compared to a second, the timescales involved in the evolution of an electron wave packet within an atom are incredibly short compared to a second.

To probe and resolve the dynamics of atoms or molecules, one needs tools that occur on a similar or even shorter timescale. A famous example is Muybridge's Horse [1], where series of experiments were conducted in the late 19th century to settle a debate about whether all four hooves of a galloping horse are simultaneously off the ground during a certain phase of the gallop. With the help of a camera, it was proven that for a brief moment during the gallop, all four of the horse's hooves are indeed off the ground. In the case of observing microscopic dynamical processes, the "camera" here is produced with ultrashort laser pulses. In recent years, significant advancements have occurred in the development of sources capable of generating such ultrashort pulses. These pulses can exhibit a wide range of properties, which may vary considerably based on factors like their duration, energy, and the method of generation. Nowadays, with the help of mode-locked lasers [2, 3], such pulses can reach

duration down to a few femtoseconds and intensities more than 10^{14} W/cm^2 [4–6]. With the nonlinear process of high harmonic generation [7], pulse duration can even reduce to tens of attoseconds, and it becomes possible to generate isolated attosecond pulses [8] or pulse trains [9]. These pulses can be used to perform time-resolved measurements on the natural timescale of electronic excitation in atomic [10–12], molecular [13–15] and solid-state systems [16].

The time evolution of the dynamics of microscopic systems interacting with electromagnetic fields under non-relativistic quantum theory can be described by the time-dependent Schrödinger equation

$$i\hbar\frac{\partial}{\partial t}\left|\Psi(t)\right\rangle = \hat{H}\left|\Psi(t)\right\rangle . \tag{1.1}$$

This is the general equation of motion represented by the quantum wave function $|\Psi(t)\rangle$, and the Hamilton operator $\hat{H}$ describes the energy of the system. The temporal evolution of the system is encoded in the complex phases "$\exp[-i\hat{H}t] = \exp[-i(E/\hbar)t]$", from which one sees its relation to the energy of the quantum state. The time and phase relation of an oscillation with frequency ω is

$$T = \frac{2\pi}{\omega} = \frac{2\pi\hbar}{E}. \tag{1.2}$$

In the context of quantum mechanics, where only relative changes of time are meaningful, a straightforward approach to defining temporal changes is to evaluate the derivative of the phase φ. This derivative can be represented as

$$\Delta T = \frac{d\varphi}{dE}. \tag{1.3}$$

Phases characterize the complex amplitudes within a quantum system's superposition of discrete states, known as eigenstates, each identified by its associated energy level. When only a single state is occupied, as exemplified by the lowest Bohr orbit of an atom mentioned earlier, no observable temporal evolution occurs. The measurable quantity here is $|\Psi|^2$, one can see the imaginary phase part drops out. To overcome this intrinsic property, more than one quantum state is needed, meaning that the electron wave function occupies more than one Bohr orbital. In such cases, properties like the mean position of the electron relative to the nucleus undergo time-dependent changes and become measurable.

By measuring the phase evolution of the system at a certain energy, one can correspondingly gain insight into its time evolution. However, limited by detector resolution and sensitivity, direct measurements of time-dependent phases on the electronic attosecond timescale are not yet possible. The solution is provided by the concept of interferometry. A prominent example is the detection of gravitational waves [17], the perturbations in spacetime induced by gravitational waves are observed by employing laser interferometry to measure distances with extreme sensitivity. In the realm of quantum systems, an easily accessible experimental observable closely associated with their phase evolution is the energy of particles or photons that interact with or are emitted by the system. The high degree of coherence of the laser is able to fully conserve the phase of the quantum states. To capture ultrafast dynamics on the atomic timescale, it is essential to have a broad and coherent spectrum that spans a wide range of frequencies, which covers a broad energetic range of quantum states that supports their ultrafast

dynamics. The reason for a broad spectral range follows the concept of Fourier analysis [18], the temporal bandwidth and frequency components are directly connected. Fourier analysis reveals the frequencies present in a signal and their respective amplitudes and phases. The frequency domain representation allows you to identify dominant frequencies and their contributions to the overall signal. The spread of frequencies in the spectrum provides information about the signal's temporal characteristics. The correspondence between time and energy in quantum mechanics implies that temporal information about a quantum system is inherently encoded in the energy spectrum of observations, which is exactly what's being measured. This principle is a fundamental aspect of quantum mechanics and is known as the energy-time uncertainty principle, which relates the uncertainty in energy measurements to the uncertainty in time measurements. Essentially, any measurement or observation of a quantum system's energy spectrum provides indirect information about the system's temporal behavior. The energy levels and transitions within the system reveal how it evolves over time, as transitions between different energy states occur with specific frequencies or over specific time intervals.

In summary, measuring time-dependent processes in quantum mechanics by retrieving time information from a phase changing with time involves Fourier analysis, interferometry, and advanced spectroscopic techniques. The spectroscopic techniques used in this thesis are attosecond transient absorption spectroscopy (ATAS) and attosecond streaking spectroscopy.

In ATAS, one uses these attosecond pulses to probe the absorption of light of particles. This involves creating a time-delay between the attosecond pump pulse and a probe pulse, which induces changes in the absorption lineshape as a function of this delay. In streaking, one uses the attosecond pulses to ionize atoms, the emitted photoelectrons have energies that depend on the time they were released. By measuring the momentum distribution and timing of these photoelectrons, one can retrieve the full temporal profile of the electric fields and the time-delay axis. These two techniques offer complementary information, and their combination can provide valuable insights into attosecond timescale dynamics. The challenge to combining ATAS and AS is to perform both measurements on the same target simultaneously. To achieve this, precise timing and synchronization of the attosecond pulse generation and the measurement apparatus are needed, as well as different requirements for the target gas densities have to be met. Combining ATAS and AS is a complex experimental setup that requires advanced laser systems and precise synchronization, making it a valuable tool in attosecond science research.

In this work, a novel beamline is presented for the simultaneous measurement of ATAS and attosecond streaking spectroscopy. By simultaneously measuring the resonant photoabsorption spectra of laser-coupled doubly excited states in helium, together with the streaked photoelectron spectra, From the absolute time-delay zero calibrated spectra, one can extract delay-related physical quantities. For instance, a state-resolved phase of the time-delay dependent modulation of absorption is used to determine the relative signs of transition dipole matrix elements between the bound states. We also extract delay-dependent phase information of the dipole response of the couplings from absorption lineshapes. In the second chapter of this thesis, the theoretical framework of the physics fundamentals in this type of experiments are given. In the following chapters, the experimental apparatus of our simultaneous

ATAS and streaking are shown, as well as the data processing and calibrations procedures. The transient absorption spectrum of the helium doubly excited states and streaking spectrum will be presented in the fifth chapter. The delay-dependent lineout oscillation of the laser-driven two-electron wave packet of the delay-calibrated absorption spectrum will be compared with a quantum mechanical model simulation. The phase and amplitude information of the dipole response is also extracted from the resonance absorption lineshape. At last, the results of this thesis are summarized and concluded.

Chapter 2

Theoretical background

2.1 Ultrashort laser pulses

The ultrashort laser pulse is a fundamental tool in ultrafast science in the time-resolved measurements of ultrafast dynamics on their natural timescales, moreover, it can be used to generate even shorter pulses in the attosecond regime. Its properties have been introduced in various textbooks such as [19], which this chapter will be referring to.

The mathematical description of an ultrashort pulse starts with a time-dependent electric field $E(t)$ with a slow varying envelope $\mathcal{E}(t)$ and a rapid oscillating term describing the carrier wave:

$$E(t) = \mathcal{E}(t)\, cos[\phi(t)]. \tag{2.1}$$

For mathematical convenience, the field can also be written in the complex form, and the real part still represents the measurable physical quantity:

$$E(t) = \mathcal{E}(t)e^{i\phi(t)}. \tag{2.2}$$

$\mathcal{E}(t)$ gives the overall temporal structure and duration of the pulse, which is the full width at half maximum (FWHM) of the intensity profile $I(t) \propto \mathcal{E}(t)^2$. The envelope can be described by analytical functions, here the Gaussian case is taken as an example with its envelope and duration given by

$$\mathcal{E}_G(t) = \mathcal{E}_0(t)e^{-\left(\frac{t}{t_G}\right)^2} \tag{2.3}$$

and

$$t_G = \frac{t_{\text{FWHM}}}{\sqrt{2\ln 2}} \approx 0.849 \cdot t_{\text{FWHM}}. \tag{2.4}$$

The temporal phase $\phi(t)$ can be Taylor expanded into

$$\begin{aligned} \phi(t) &= \sum_{k=0}^{\infty} \frac{\phi(t-t_0)^{(k)}}{k!}(t-t_0)^k|_{t_0=0} \\ &= \phi_{\text{CEP}} + \omega_c t + \varphi(t), \end{aligned} \tag{2.5}$$

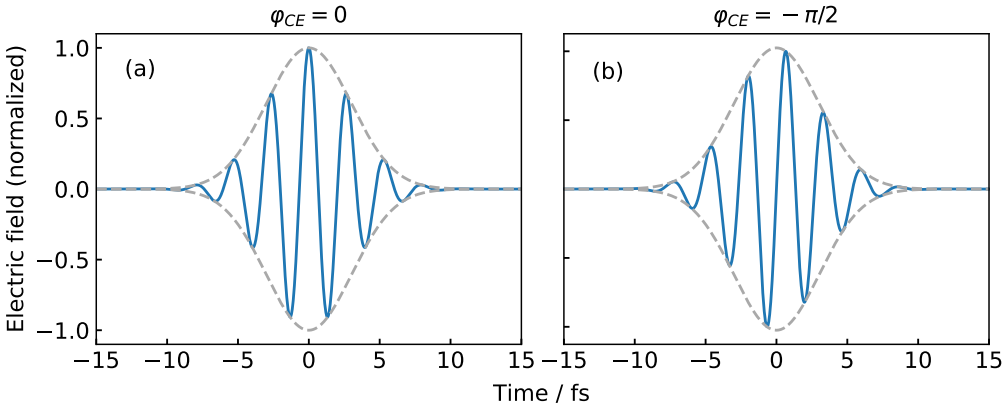

Figure 2.1: Definition of CE phase of a laser pulse with pulse duration 5 fs, and 1.5 eV central energy in temporal domain. The carrier wave is shown in blue solid line and the pulse envelope is shown in grey dashed line.

where ϕ_{CEP} is the phase shift between the carrier wave and pulse envelope, often referred to as the carrier envelope phase (CEP), ω_c is the central frequency of the carrier wave, and $\varphi(t)$ includes the higher order phase terms in the expansion. When the pulse duration is on the order of one cycle of the carrier wave, the phase ϕ_{CEP} will affect the intensity distribution as shown in Fig. 2.1. Another term related to the pulse is the instantaneous frequency:

$$\omega(t) = \frac{d\phi(t)}{dt} = \omega_c + \frac{d\varphi(t)}{dt}, \tag{2.6}$$

which describes the modulation of the frequency across the pulse. If the term $\varphi(t) \neq 0$, then the frequency will increase (up-chirped) or decrease (down-chirped) over its duration. The chirp is linear for order $k = 2$, and non-linear for $k > 2$. The pulse can also be described in the frequency domain (spectral domain), it is obtained by performing a Fourier transform to the time domain field:

$$\tilde{E}(\omega) = \mathscr{F}[E(t)] = \frac{1}{2\pi} \int_{-\infty}^{+\infty} E(t) e^{-i\omega t} dt, \tag{2.7}$$

The inverse Fourier transform is

$$E(t) = \mathscr{F}^{-1}[\tilde{E}(\omega)] = \frac{1}{2\pi} \int_{-\infty}^{+\infty} \tilde{E}(\omega) e^{i\omega t} d\omega. \tag{2.8}$$

Due to this Fourier relation, the shorter the pulse is in time, the broader it will be in the spectral domain and vice versa. Thus, to generate a ultrashort pulse, one would need a broad spectrum. The pulse duration Δt and spectral bandwidth $\Delta\omega$ fulfills the uncertainty principle [19]

$$\Delta t \Delta\omega \geq 2\pi c_B. \tag{2.9}$$

Where the constant c_B depends on the exact temporal shape of the intensity.

2.2 Strong laser fields

In the preceding section, properties of the laser pulse in the temporal domain such as the duration and dispersion of ultrashort laser pulses were introduced. In this section, another important characteristic: the strength of the laser electric field will be discussed. The peak intensity of the femtosecond laser pulse used in the experiment here is on the order of 10^{14} W/cm^2, corresponding to an electric field strength of 10^9 V/cm. This value is approaching the atomic unit of field strength (5.14×10^9 V/cm), which is the strength of the Coulomb field experienced by an electron in the first Bohr orbit of atomic hydrogen. In general, peak intensities beyond 10^{12} will already be regarded as strong. The typical definition of the strong-field regime is via the ponderomotive potential(which depends on the frequency, described in Eq. 2.14), which needs to be larger than the ionization potential.

Light matter interactions with strong laser field can no longer be treated perturbatively. Thus, to define strong fields, one approach is to use characteristic energies of the atom and the field. Following Newton's law, the motion of an free electron in a electric field can be described classically

$$a(t) = \frac{d^2}{dt^2}x(t) = -\frac{e}{m_e}E(t), \tag{2.10}$$

$$v(t) = \frac{d}{dt}x(t) = v_0 - \frac{e}{m_e}\int_{-\infty}^{t} E(t')dt' = v_0 + A(t), \tag{2.11}$$

$$x(t) = x_0 + v_0 \cdot + \int_{-\infty}^{t} A(t')dt' \tag{2.12}$$

where e and m_e are the electron charge and mass. And $A(t)$ of the electric field is the vector potential:

$$A(t) = -\frac{e}{m_e}\int_{-\infty}^{t} E(t')dt'. \tag{2.13}$$

Assuming a plane wave $E(t) = E_0\cos(\omega t + \phi)$ to solve the equations of motion analytically. The cycle-averaged kinetic energy of an electron in a laser field, initially at rest, is referred to as the ponderomotive energy

$$U_p = \frac{1}{2}m_e\overline{v(t)^2} = \frac{e^2\mathcal{E}_0^2}{2m_e\omega^2}. \tag{2.14}$$

Another characteristic energy for atoms interacting with an electric field is the ionization potential I_p, it is the energy needed to remove one bound electron from the atom. Table 2.1 below gives the I_p of some commonly used noble gases.

	He	Ne	Ar	Kr	Xe
I_p (eV)	24.59	21.56	15.76	14.00	12.13
I_p (a.u.)	0.9036	0.7925	0.5792	0.5145	0.4458

Table 2.1: Ionization potential for noble gases calculated from [20].

2.2.1 Strong field ionization

The starting point for many processes in strong laser fields is the ionization of electrons, the mechanism of ionization depends on the laser intensity and the ionization potential I_p of the atomic system. The work of Keldysh [21, 22] unified the multiphoton and tunneling ionization processes into one parameter: the Keldysh parameter γ, to describe the ionization under weak- and strong- electric field regimes:

$$\gamma = \omega \frac{\sqrt{2I_p}}{I} = \sqrt{\frac{I_p}{2U_p}}, \tag{2.15}$$

where I is the field intensity, and U_p is the ponderomotive potential. It is the ratio of the estimated tunneling time of an electron through a potential well, with respect to the laser period. For $\gamma \gg 1$, it is in the multiphoton ionization regime, where several photons are non-linearly absorbed to overcome the ionization potential, the photoionization rate strongly depends on the laser frequency. For $\gamma \ll 1$, it is the tunneling ionization regime, the electric field bends the Coulomb potential so that the bound electron can tunnel through the potential barrier, and photonionization rate then becomes frequency independent.

2.2.2 Attosecond pulse through high-harmonic generation

The electronic motion is on the attosecond timescale, to observe these dynamics one would need laser pulses that are short enough to excite as well as resolve the dynamics. The typical photon energy for this purpose is usually 10 eV or higher, falling within the XUV and soft X-ray spectral range. High-harmonic generation (HHG) is able to produce attosecond XUV pulses that meet these conditions. The generated XUV pulse can reach photon energies in the keV regime [23] and pulse duration below 100 as [24–26]. Detailed descriptions can be found in [27–29], in this section, a short overview of the most important aspects will be given.

The HHG generation happens when a linearly polarized, short-pulse laser beam with an intensity around 10^{14} W/cm^2 interacts with noble gases, it gives rise to odd harmonics of the fundamental frequency. These harmonics can extend up to tens or even hundreds in order in the resulting output beam. Nobel gases were used because of their large binding energies. The intensity of the first few harmonic order decreases quickly with increasing order, then after some orders the intensity will remain almost unchanged over a range of orders, forming a plateau region. Then, the signal cuts off rapidly at the highest order.

A classical three-step model [30] proposed in 1993 is a straightforward description of the mechanism, illustrated in Fig. 2.2. First, consider an atom in an oscillating electric field of

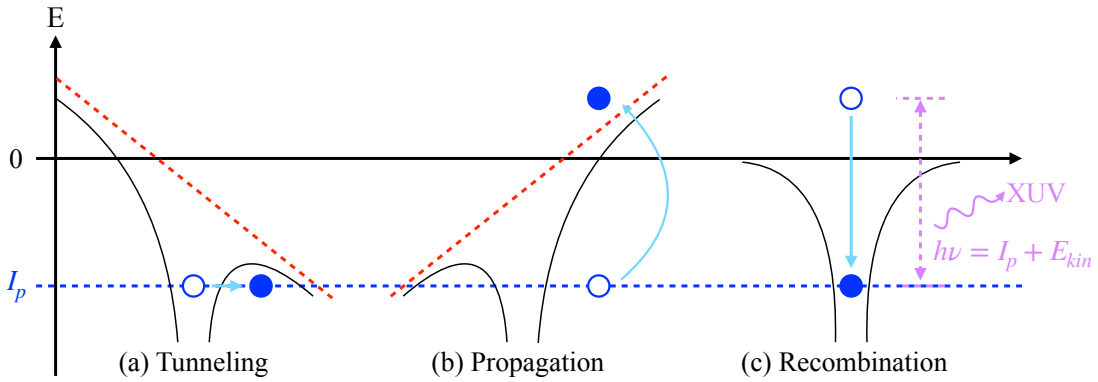

Figure 2.2: Schematic illustration of the three-step model for HHG. The Coulomb atomic potential is shown in black while the laser electric field is shown in red. (a) Tunneling, the intense laser field potential bends the Coulomb potential of the atom, causing an electron to tunnel out. (b) Propagation, the freed electron propagates in the laser field, and when the electric field potential reverses, the electron is driven towards its parent ion. (c) Recombination, the electron could recombine with its parent ion and emits an XUV photon.

a strong laser pulse, its Coulomb potential will be deformed by the external electric field. The superposition of the laser field and the Coulomb field transforms the potential well that binds the electron into a potential barrier, then the electron could tunnel through. Then, the freed electron will follow the field potential and move away from the parent ion, then it will be accelerated and gains kinetic energy E_{kin}. Finally, in the next half-cycle of the oscillatory field, the electron is driven back by the field towards the ion, which can lead to the recombination of the electron. When it recombines, the excess kinetic energy will be transferred into a single high energy photon, with its photon energy given by

$$\hbar\omega_{HHG} = E_{kin}^{(r)} + I_p. \tag{2.16}$$

The kinetic energy $E_{kin}^{(r)}$ at the moment of recombination can come from two classical trajectories within one laser cycle, which are the short and long trajectories. This generation process can occur every half-cycle of the laser pulse and interferes with events from other cycles. This interference gives rise to harmonic photon energies spaced by $2\hbar\omega_c$, and ω_c is the fundamental frequency of the laser field. The energy gained by the electron depends on the time of the ionization from the driver pulse. The maximum recombination energy is found to be $3.17U_p$ by calculating the classical trajectories depending on the time of ionization within the pulse, which happens close to the maximum of the electric field. This gives us the maximum achievable photon energy

$$\hbar\omega_{\text{HHG,cut-off}} = 3.17\, U_p + I_p, \tag{2.17}$$

which means the emitted photon energy is limited to a certain cut-off energy. The time window of the tunneling ionization for each trajectory is less than a quarter of the electric field

cycle, which produces a broad range of recombination energy. This range of equally probable recombination energies is also known as the plateau region.

Another approach to understanding the HHG process is to fully treat the electron motion quantum-mechanically, while the strong field is described classically. The generated harmonic radiation can be interpreted as the quantum-mechanical interference of the different parts of the wave function. The ground state wave function is ionized and propagates in the continuum and then interferes with the still-bound wave function around the parent ion. This interference gives rise to a rapidly oscillating dipole moment which is the source of the emission of the high-energy harmonic radiation.

2.3 Quantum dynamics

In general, the dynamics of a quantum mechanical system can be fully characterized by the wave function Ψ and its time evolution. The time evolution of the system is described by the unitary time translation operator $\hat{U}(t, t_0)$ which is characterized by the generation function $\hat{H}$. $\hat{H}$ is also known as the Hamilton operator, describing the energy of the system. In the non-relativistic case, the equation of motion is given by the time-dependent Schrödinger equation

$$i\hbar\frac{\partial}{\partial t}\left|\Psi\right\rangle = \hat{H}\left|\Psi\right\rangle, \tag{2.18}$$

where $\hbar$ is the Planck constant. The state $|\Psi\rangle$ can be expanded in the eigenstates of the system

$$\left|\Psi(t)\right\rangle = \sum_n c_n(t)\left|\phi_n\right\rangle + \int dE\, c(E,t)\left|\chi_E\right\rangle. \tag{2.19}$$

Here, $|\phi_n\rangle$ represents the bound states and $|\chi_E\rangle$ the continuum states. $c_n(t)$ and $c(E,t)$ are the complex expansion coefficients. Without external perturbation, $\hat{H}_0$ will be independent of time, its eigenvalue defines the energy of each discrete and continuous state. Using 2.18, the time-dependent expansion coefficients are expressed as

$$c_n(t) = c_{n,0}\, e^{-i\frac{E_n}{\hbar}t} \tag{2.20}$$

and

$$c(E,t) = c(E,0)\, e^{-i\frac{E}{\hbar}t}, \tag{2.21}$$

where the evaluations begins at $t = 0$ with the initial values $c_{n,0}$ and $c(E, 0)$.

For the study of dynamics induced by time-dependent fields such as the XUV and NIR fields, it is more convenient to split the total Hamiltonian into two parts $\hat{H} = \hat{H}_0 + \hat{V}$: the unperturbed and time-independent system $\hat{H}_0$ and the interaction operator $\hat{V}$. The wave function can be expended into a set of the energy eigenstates of the unperturbed system

$$\left|\psi\right\rangle = \sum_{i=1}^{n} c_i\left|i\right\rangle, \tag{2.22}$$

where c_i is the complex-valued, time-dependent state coefficients. The evolution of the system will be found by determining the evolution of the n state coefficients. Then, the Hamiltonian is represented by a $n \times n$ matrix, with the energies $E_i = \langle i| \hat{H}_0 |i\rangle$ on the diagonal and couplings $V_i j = \langle i| \hat{V} |i\rangle$ on the off-diagonal elements.

$$\hat{H} = \begin{bmatrix} E_1 & V_{12} & & V_{1n} \\ V_{21} & E_2 & & V_{2n} \\ & & \ddots & \\ V_{n1} & V_{n2} & & E_n \end{bmatrix}, |\psi\rangle = \begin{bmatrix} c_1(t) \\ c_2(t) \\ \vdots \\ c_n(t) \end{bmatrix}. \tag{2.23}$$

In the dipole approximation in length gauge $\hat{V} = \hat{d}F(t)$, the matrix elements V_{ij} equals to

$$V_{ij} = \langle i| \hat{V}(t) |j\rangle = \langle i| \hat{d} |j\rangle F(t) = \mu_{ij} F(t), \tag{2.24}$$

where $\hat{d}$ is the dipole operator, μ_{ij} is the dipole matrix elements.

2.3.1 Time-dependent perturbation theory

For arbitrary time-dependent interactions it can be impossible to find analytical solutions for the time-evolution of the system, therefore, perturbation theory is applied to get approximate eigenstates and eigenvalues.

The Hamilton operator can be divided into the Hamiltonian of the unperturbed system $\hat{H}_0$ and a perturbation $\hat{H}_{int}$ as follows

$$\hat{H} = \hat{H}_0 + \hat{H}_{int}, \tag{2.25}$$

this can express all interactions with external fields. In general, the expressions produced by perturbation theory are not exact, but they can lead to accurate results as long as the expansion parameter is very small. Then, the results are expressed in terms of finite power series which could converge to the exact values when summed to higher order. In our case, the purpose of perturbation theory is to approximately solve the Schrödinger equation 2.18 and obtain the eigenstates and eigenvalues for the case of $\hat{H}_{int} \neq 0$. If the perturbation is weak, meaning the characteristic energies are small compared to energies and energy separations of the system, the Hamiltonian can be written as

$$\hat{H} = \hat{H}_0 + \lambda \hat{V}(t), \tag{2.26}$$

where λ is a small scaling parameter of the perturbation.

In the case of $d\hat{H}/dt = 0$, an expansion of E_n and $|n\rangle$ in powers of λ will express correction terms to the eigenstates and energies brought by the perturbation [31]. For $d\hat{H}/dt \neq 0$, a time-dependent version of the perturbation theory is used. Where only the dynamical changes of the wave function due to the time-dependent perturbation $H_{int} = \hat{V}(t)$ are considered. This is called the interaction picture, a "mixture" of both the Schrödinger and Heisenberg picture.

In this picture, the wave function $|\Psi\rangle(t)_I$ and perturbation $V(t)$ follow the equations

$$i\hbar\frac{\partial}{\partial t}\,|\Psi(t)\rangle_I = \hat{V}_I(t)\,|\Psi(t)\rangle_I, \tag{2.27}$$

with

$$\hat{V}_I(t) = e^{i\hat{H}_0 t}\,V(t)\,e^{-i\hat{H}_0 t}. \tag{2.28}$$

The wave function can be expanded into a complete set of basis states $|\Psi(t)\rangle = \sum_n c_n(t)|n\rangle$. Inserting this into equation 2.27 and 2.28, and contracting over a general basis state $|m\rangle$, we have the relation coupled time dependent state coefficient $c_n(t)$

$$i\hbar\frac{\partial}{\partial t}c_m(t) = \sum_n \langle m|V(t)|n\rangle\; e^{i(E_m-E_n)}\; c_n(t). \tag{2.29}$$

This relation of the coefficients can also be written into a perturbation expansion in powers of the interaction

$$c_n(t) = c_n^{(0)} + c_n^{(1)} + c_n^{(2)} + ..., \tag{2.30}$$

where $c_n^{(0)}$ represents the initial state without the perturbation. The time evolution of the wave function can be described by a time-evolution operator

$$|\Psi(t)\rangle = \hat{U}(t,t_0)|\Psi(t_0)\rangle. \tag{2.31}$$

The expression for $\hat{U}(t,t_0)$ is

$$\hat{U}(t,t_0) = \mathbf{I_n} + \sum_{n=1}^{\infty}(-i)^n \int_{t_0}^{t} dt_1 \int_{t_0}^{t_1} dt_2 ... \int_{t_0}^{t_n-1} dt_n \hat{V}(t_n)...\hat{V}(t_1). \tag{2.32}$$

Consider a system in a general initial state $|i\rangle$ and inserting the identity matrix $\mathbf{I_n} = \sum_n |n\rangle\langle n|$ into equation2.31, we will have

$$\hat{U}(t,t_0)|i\rangle = \sum_n |n\rangle\langle n|\hat{U}(t,t_0)|i\rangle,\; c_n(t) = \langle n|\hat{U}(t,t_0)|i\rangle. \tag{2.33}$$

Then we combine equations 2.32 and 2.33, we can derive the first and second order expansion coefficients

$$c_n^{(1)}(t) = -i\int_{t_0}^{t} dt'\;\langle n|V(t')|i\rangle\; e^{i(E_m-E_n)t'} \tag{2.34}$$

$$c_n^{(2)}(t) = -\sum_m \int_{t_0}^{t} dt' \int_{t_0}^{t'} dt''\;\langle n|V(t')|m\rangle\langle m|V(t'')|i\rangle\; e^{i(E_n-E_m)t'+i(E_m-E_i)t''}. \tag{2.35}$$

2.4 Few-level system

2.4.1 The helium atom

In this work, the doubly excited states (DES) in helium is investigated, it is the most simple system with two correlated electrons. However, due to this electron correlation, the Coulomb repulsion cannot be neglected during interaction, causing the helium of two electrons and one nuclei to become a three-body system, and there is no known analytical solution. Thus, the solution of the Schrödinger equation cannot be written as the product of two single-electron wave functions

$$\Psi^{(2)}(\vec{r}_1, \vec{r}_2) \neq \Psi^{(1)}(\vec{r}_1)\Psi^{(1)}(\vec{r}_2). \tag{2.36}$$

Instead, the wave function is written as

$$\Psi^{(2)}(\vec{r}_1, \vec{r}_2) \cdot \chi(S_1, S_2), \tag{2.37}$$

where the first and second term describes the spatial degrees of freedom and the spin of both electrons, respectively [32].

The usual atomic term symbols follow LS coupling (Russell-Saunders coupling), in spectroscopic notation presented as

$$^{2S+1}L^{\pi}, \tag{2.38}$$

where L is the total angular momentum quantum number, S is the total spin quantum number, and π the parity of the state, which will be either "o" (odd, bright states) or "e" (even, dark states). The term $2S + 1$ is the spin multiplicity, the number of possible values of the spin magnetic quantum number for a given spin S. The L quantum number is usually given in letter notation with $L = \mathrm{S}, \mathrm{P}, \mathrm{D}, \mathrm{F}, ...$ denoting the sum angular momentum of the single electron orbits. The DES of helium in this work are spin singlet states $S = 0$ with an antisymmetric spin wave function $\chi(1, 2)$. Under dipole approximation, only transitions between different parity states are allowed. In our helium case, the ground state $^1S^e$ can only interact with $^1P^o$ states with single photon transitions.

The generated attosecond XUV pulse covers a wide energy range, therefore, multiple configurations of electronic states in helium can be excited. Fig. 2.3 plots the energy states above the N=1 continuum, below this threshold at 24.59 eV sits the singly excited states with only one electron excited from the ground state. For energies above N=1 threshold, the system can ionize directly or both electrons can be excited simultaneously. The DES with N=2, there are three possible configuration series, the $2snp$, $2pns$, and $2pnd$ series [34] which converges to the N=2 ionization threshold at 65.04 eV. The superposition of states is described with a linear combination of the orbital configurations [35], because the states of the first two series are not distinguishable

$$\frac{1}{\sqrt{2}}(2snp \pm 2pns), \text{ denoted } sp_{2,n\pm}, \tag{2.39}$$

where the "+" and "-" are the strong and weak series, meaning they appear more or less prominent in absorption spectra.

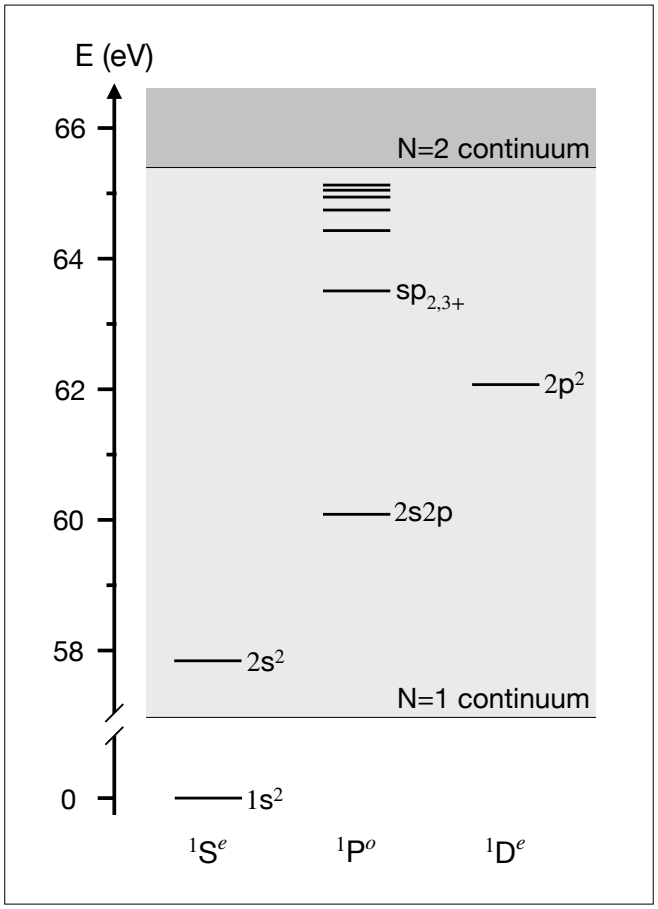

Figure 2.3: Level Scheme of the helium atom for the levels below the N=2 continuum relevant for this work. The energy positions are taken from [33]. The mixing of these states with the energetically degenerate N = 1 continuum is the essence of Fano-type autoionization and quantum interference apparent in absorption spectra.

Photon energy 60.15 eV is larger than the ionization potential of the ground state 24.59 eV, thus a single electron can be emitted and the other electron stays in the ground state of He^+, which is referred to as direct ionization. Another possible situation is both electrons can be excited to the $2s2p\ ^1P^o$ state, this state then autoionizes with one electron returning to the ground state of He^+ and the other electron leaving the atom. Autoionization will happen by the interaction of the excited electrons with other electrons.

2.4.2 Autoionization and Fano theory

Fano's description of configuration interaction dated back to the early 1960s, provides a straightforward framework for comprehending the theory of autoionization [36]. It typically occurs when an atom or molecule is in an excited state, often after absorbing energy from an external source, such as photons from laser light or collisions with other particles. These processes often results in interference effects, where multiple pathways or quantum states are involved in the energy transfer and ionization process. The process of autoionization of the doubly excited states gives rise to asymmetries in the cross-sections of the transition resonances. Fano showed the asymmetric lineshape is from interference between two different pathways to the same final state. In the case of helium, the two pathways involve discrete and continuum states, one is the transition from the ground state directly into the continuum, and the other is coupling through the autoionizing states.

Due to this coupling of the excited state b with the continuum c_E, the eigenstate of the Hamiltonian $\hat{H}_0$ becomes a superposition of them. The energy of the excited state $E_b = \langle b| \hat{H}_0 |b\rangle$ lies above the ionization threshold, their coupling happens via the configuration interaction operator $\hat{V}$, which leads off-diagonal elements $V_E = \langle c_E| \hat{V} |b\rangle$ of the full Hamiltonian. By diagonalizing the coupled Hamiltonian we can represent the eigenstates as a linear combination of the basis states, then the goal becomes determining the energy-dependent expansion coefficients, which solution is included in Fano's work [36].

As a result, the bound state is mixed with a set of continuum states due to configuration interaction and causes a rapid change in the expansion of the state around the resonance energy within an energy range defined as Γ. In other words, the modified bound state becomes autoionizing due to the loss channel to the continuum with a finite lifetime $\tau \propto 1/\Gamma$. Fano related the transition amplitude from the ground state $|g\rangle$ to the energy eigenstate $|a\rangle$ and to the continuum states $|c_E\rangle$, and introduced the q parameter.

$$q = \frac{\langle a| \hat{d} |g\rangle}{\pi V_E^* \langle c_E| \hat{d} |g\rangle} = \frac{d_{ag}}{\pi V_E^* d_{cg}}. \tag{2.40}$$

The absorption cross-section of the Fano profile can be written as

$$\sigma \propto \frac{|q+\epsilon|^2}{1+\epsilon^2} = 1 + \frac{q^2 - 1 + 2q\epsilon}{1+\epsilon^2}, \tag{2.41}$$

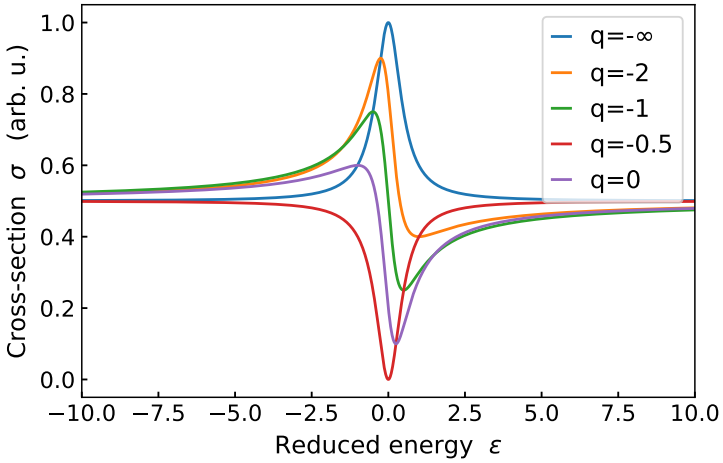

Figure 2.4: Asymmetric Fano resonance lines for different values of the Fano q parameter. The cross section of a resonance embedded in a continuum is plotted in arbitrary units depending on the normalized energy ε. The cross section changes to a Lorentz line shape for $q = \pm\infty$.

with the reduced energy

$$\epsilon = \frac{E - E_a}{\Gamma/2}. \tag{2.42}$$

In spectroscopic aspect, the two pathways are identical, they can be seen as two arms of a quantum interferometer. And depending on the relative transition strength, the corresponding asymmetric lineshape is plotted in Fig. 2.4.

2.5 Attosecond transient absorption spectroscopy

2.5.1 Linear absorption

In absorption, the laser interacts with a system of many particles, one can start with the dipole response to the incoming field of a single particle. Its interaction with electromagnetic fields will cause population to transfer from the ground state into one or more excited states, depending on the provided photon energy range. The excitation through the field generally leaves the quantum system in a superposition of states which form a wave packet that is non-stationary in time, generating a time-dependent dipole

$$d(t) = e \langle\psi| \hat{x} |\psi\rangle . \tag{2.43}$$

The dipole in turn generates an external electric field via polarization

$$P(t) = \varrho\, d(t), \tag{2.44}$$

where ϱ is the density of the medium.

In the experiment, usually the transmitted intensity spectrum $I(\omega)$ is measured, one can also measure a reference spectrum $I_0(\omega)$ without the target medium. The absorbance of the medium is often described in units of optical density (OD)

$$OD = -\log_{10}\left(\frac{I(\omega)}{I_0(\omega)}\right). \tag{2.45}$$

The derivation starts from an integration of the electric field F, with the precondition that the medium is homogeneous, meaning $\varrho(z) = \varrho$ and $d(\omega, z) = d(z)$

$$\begin{aligned} F(\omega, L) &= F(\omega, 0) + i\frac{\omega}{2\epsilon_0 c}\int_0^L dz\ \varrho(z)\ d(\omega, z) \\ &= F(\omega, 0) + i\frac{\omega\varrho L}{2\epsilon_0 c} d(\omega) \\ &= F_{in} + iF_{gen}. \end{aligned} \tag{2.46}$$

It is valid if the generated field F_{gen} is small, which means the change of the incoming field F_{in} along the propagation path is negligible. With the coefficient i in front of the F_{gen}, it is shifted by $\pi/2$ in phase from F_{in} and will interfere destructively with the incoming field. And when we take the square to calculate intensity, the F_{gen} term can be dropped:

$$I(\omega) = |F(\omega)|^2 = |F_{in}|^2 - iF_{in}F_{gen}^* + iF_{in}^*F_{gen}. \tag{2.47}$$

Then we take the ratio

$$\begin{aligned} \frac{I(\omega)}{I_0(\omega)} &= \frac{|F_{in}|^2 - iF_{in}F_{gen}^* + iF_{in}^*F_{gen}}{|F_{in}|^2} \\ &= 1 - i\left(\frac{F_{gen}^*}{F_{in}^*} - \frac{F_{gen}}{F_{in}}\right) \\ &= 1 - 2\,\mathrm{Im}\left(\frac{F_{gen}}{F_{in}}\right). \end{aligned} \tag{2.48}$$

Because $F_{gen} \ll F_{in}$, it is valid to the approximation $\ln(1-x) \approx -x$ and take the logarithm of the above formula to obtain

$$\begin{aligned} OD(\omega) &= -\log_{10}\left(\frac{I(\omega)}{I_0(\omega)}\right) \\ &= \frac{\varrho L\omega}{\ln(10)\varepsilon_0 c}\mathrm{Im}\left(\frac{d(\omega)}{F_{in}(\omega)}\right) \\ &= (\varrho L)_{a.u.}\frac{4\pi\alpha\omega}{\ln(10)}\mathrm{Im}\left(\frac{d(\omega)}{F_{in}(\omega)}\right). \end{aligned} \tag{2.49}$$

By measuring optical densities, The above optical density describes an arbitrary non-linear relationship between the incoming field and the generated dipoles, it can be further simplified in the weak-field limit, where the macroscopic polarization has a linear relationship with the electric field

$$P(\omega, z) = \varrho\, d(\omega, z) = \varepsilon_0\, \chi(\omega) F(\omega, z). \tag{2.50}$$

2.5.2 The time-dependent dipole response

The optical density is a measured quantity, to obtain intuitive insight into the real-time dynamics of the system one is interested in the time-dependent dipole. Following 2.43, the time evolution of the wave packet forms an electron distribution that constitutes a dipole moment.

After a certain time duration, the excited system will spontaneously emit exactly one photon. Because the wave packet is a distribution, the exact time of emission cannot be predicted, only the probability distribution of a large number of events of the emission process can be measured. This distribution defines the lifetime τ and the spectral width Γ of the emitted photons, they have the relation $\Gamma = 1/\tau$.

For a simple system of only the ground state $|g\rangle$ and one excited state $|e\rangle$, the coupling between them results in an exponentially decaying dipole oscillation. Under the framework of perturbation theory, its amplitude evolution after the excitation is given by the state

$$|\Psi(t)\rangle = |g\rangle - i\, e^{-i\omega_e t - \frac{\Gamma}{2}} c_e(t_0)\ |e\rangle\,, \tag{2.51}$$

here, $c_g(t_0) \approx 1$ and $E_g = 0$. The dipole will become

$$d(t) = \langle\Psi|\,\hat{x}\,|\Psi\rangle \propto |\,\langle e|\,\hat{x}\,|g\rangle\,|\, e^{-\frac{\Gamma}{2}}\, \sin(\omega_e t)\, c_e(t_0)\, \theta(t). \tag{2.52}$$

The term ω_e is the energy spacing between the two states, Γ is the decay width of $|e\rangle$. And $c_e(t_0)$ is the population at t_0, which is given by $c_e(t_0) = c_g(t_0)\mu_{ge}\mathcal{E}$, where μ_{ge} is the dipole matrix element and $\mathcal{E}$ is the excitation field strength. $\theta(t)$ is the Heaviside theta function, because of the assumption of an instantaneous excitation. The Fourier transform of $d(t)$ into the frequency domain gives the spectrum of the radiation emitted by this dipole.

For atomic systems with more excited states involved, the states and dynamics need to be treated according to Fano's theory. The dipole response will gain an additional phase term $\varphi(q)$ related to the Fano q parameter [37],

$$d(t) \propto c_q\, \delta(t) + c_i\, e^{-\frac{\Gamma}{2}t + i[-\omega_i t + \varphi(q)]}. \tag{2.53}$$

The Dirac delta function $\delta(t)$ represents the continuum oscillating at all possible frequencies of the system scaled with the ionization probability c_q. The phase offset term $\varphi(q)$ corresponds to the shift in dipole decay compared to the moment of excitation. It was demonstrated in [37] there is a direct relation between the phase offset $\varphi(q)$ and Fano q parameter

$$\varphi(q) = 2\arg(q - i) \ \leftrightarrow\ q = \cot\left(\frac{\varphi(q)}{2}\right). \tag{2.54}$$

2.6 Attosecond streaking spectroscopy

In the characterization of single isolated attosecond XUV pulses, the photon pulse is converted to an electron pulse through the photoelectric effect. This electron pulse subsequently interacts

with a NIR dressing pulse to extract the XUV phase information. Through ionization, the phase and amplitude of the XUV field are mapped onto a time-momentum distribution of the electrons.

2.6.1 Momentum streaking

The attosecond streaking measures the time and momentum information of the released photoelectrons of the atom interaction with strong laser fields. When the attosecond XUV beam is focused on an atomic gas target, the bound electrons of the atom can be excited into vacuum. A technique named the streak camera [38, 39], is able to measure spatial information of the electrons ejected from the atomic system, which is linked to the temporal domain. The attosecond streak camera can measure the momentum of electrons with the help of the well-developed time-of-flight (ToF) spectrometer. Another strong laser field, usually the NIR pulse, will be used to sweep the photoelectrons in momentum space.

The streaking principle can be explained in a classical picture [40, 41]. Consider an electron released from the atom at time t with initial momentum $\vec{p}_0$ in the presence of an electric field $\mathcal{E}(t)$, its equation of motion is

$$\frac{d\vec{p}}{dt} = -e\mathcal{E}(t), \tag{2.55}$$

here e denotes the electron charge. To simplify this expression, one uses the magnetic vector potential $\vec{\mathcal{A}}$, which is defined as

$$\vec{\mathcal{B}} = \nabla \times \vec{\mathcal{A}}, \tag{2.56}$$

where $\vec{\mathcal{B}}$ is the magnetic induction. And from Faraday's induction law

$$\nabla \times \mathcal{E} = -\frac{\partial \vec{\mathcal{B}}}{\partial t} = -\frac{\partial(\nabla \times \vec{\mathcal{A}})}{\partial t} = -\nabla \times \frac{\partial \vec{\mathcal{A}}}{\partial t}. \tag{2.57}$$

Then electric field can be replaced in Eq. 2.55 with

$$\mathcal{E}(t) = -\frac{\partial \vec{\mathcal{A}}}{\partial t}. \tag{2.58}$$

Then the equation of motion becomes

$$\frac{d\vec{p}}{dt} = -e\frac{\partial \vec{\mathcal{A}}}{\partial t}. \tag{2.59}$$

After integration

$$\vec{p}(t) - \vec{p}_0 = e\left[\vec{\mathcal{A}}(t) - \vec{\mathcal{A}}(t_0)\right]. \tag{2.60}$$

The electron momentum is measured after the laser pulse passes through the gas target, thus $\vec{\mathcal{A}}(t = \infty) = 0$. Then, the final observed momentum is

$$\vec{p}(t) = -e\vec{\mathcal{A}}(t_0) + \vec{p}_0. \tag{2.61}$$

This $\vec{p}$ is the canonical momentum of the electron, it is conserved during free propagation in the laser field. In a more general case, electrons are usually released with an initial momentum distribution $n_{cl}(\vec{p}_i, t)$ other than a well-defined initial momentum. The spectral width and chirp of the XUV pulse are reflected in a broad and time-dependent distribution of the initial electron energies, the observed electron spectra can be written as

$$\sigma(\vec{p}) = \int_{-\infty}^{\infty} n_{cl}(\vec{p} - \vec{\mathcal{A}}(t), t)\, dt, \tag{2.62}$$

where the initial release momentum is related to the conserved canonical momentum through $\vec{p}_i = \vec{p} - \vec{\mathcal{A}}(t)$. If one measures electron spectra with different laser pulse $\vec{\mathcal{A}}(t)$, the field free release distribution can be fully recovered.

In this work, one measures the time-delay-dependent streaked photoelectron from the target atom by the interaction with an XUV pulse in the presence of a few-cycle near-infrared (NIR) laser pulse. From a measured streaking spectrogram, one could apply retrieval algorithms to reconstruct the time-delay axis, as well as the XUV and NIR electric fields [42–44].

2.6.2 Time to momentum conversion

The recorded flying time of the released electron will be converted to the momentum. First, one assumes a monochromatic laser pulse that propagates in the x direction and is linearly polarized in the z direction. The field is expressed as

$$\mathcal{E}(t) = E_0 \cos(\omega_0 t)\vec{z} = E_0 \cos(\frac{2\pi}{T_0}t)\vec{z}. \tag{2.63}$$

Substitute it into 2.61

$$\vec{p}(t) - \vec{p}_0 = \frac{e}{\omega_0} E_0 \sin(2\pi\frac{t_0}{T_0})\vec{z}. \tag{2.64}$$

The range of t_0 variation is the attosecond pulse duration τ. For the case of τ much shorter than the laser period T_0, one gets

$$\vec{p}(t) - \vec{p}_0 \approx e\, E_0\, t_0\, \vec{z}. \tag{2.65}$$

This equation provides the principle of the mapping of electron release time t_0 to the measured momentum $\vec{p}(t)$. Figures in [45] visualized the initial time-momentum distribution of electrons and the final measured one. The peak of the attosecond pulse is located at the zero-crossing point of the vector potential of the electric field for maximum momentum shifting. The duration of the attosecond pulse should be shorter than half of the optical cycle to avoid the momentum degeneracy between two different releasing times.

In the experiment, only the electrons released in the laser polarization z direction are measured. For a transform-limited pulse, the width of the momentum distribution is

$$\Delta p = \sqrt{\Delta p_0^2 + \left(\frac{dp(t)}{dt_0}\tau\right)}, \tag{2.66}$$

where p_0 is the unstreaked distribution. The streaking speed is then

$$\frac{dp(t)}{dt_0} = e\, E_0. \tag{2.67}$$

Once the values of Δp and Δp_0 are known at a given streaking speed, the attosecond pulse duration can be determined.

Chapter 3

Experimental setup

3.1 The laser system

Since the laser was developed in 1960, it has become the dominant high-power light source. A femtosecond laser system usually has four main components, which are a gain medium, the pump laser, feedback mirrors to form the optical resonant cavity, and dispersion compensation optics.

The laser used in this work is generated by the commercial laser system FEMTOPOWER^{TM} HE/HR CEP4. The system consists of a carrier-envelope-phase (CEP) stabilized oscillator and a multi-pass amplifier, they both use titanium-doped sapphire (Ti:Sa) crystals as the gain medium. Ti:Sapphire is a commonly used gain medium for femtosecond lasers, primarily because of its broad gain bandwidth and large gain cross sections. Its center wavelength is 800 nm, which corresponds to 2.6 fs optical period.

The oscillator is pumped by a Spectra Physics Millenia solid-state pump laser with 3.5 W continuous power at 532 nm. The output of the oscillator cavity produces a continuous octave-spanning spectrum centered at 800 nm central wavelength with 3.5 nJ pulse energy and <10 fs pulse duration. The pulse then leaks through an output mirror at 75 MHz repetition rate and enters a CEP-stabilization module (CEP4). In this module, the carrier-envelope offset frequency f_{CEO} is detected based on difference frequency generation, the difference frequency signal is produced by focusing the pulse on a periodically poled lithium niobate (PPLIN) crystal for SHG. To stabilize the CEP, the pulse passes an acousto-optic frequency shifter (AOFS), which shifts the short-term drifts of the frequency offset, leading to a stable output [46]. This feed-forward scheme can provide a CEP stabilization with a standard deviation of a few mrad.

The pulses after the CEP4 module are used to seed the amplifier, which is pumped by an external Q-switched DPSS pump laser (DM-50 Photonics Industries) that delivers nanosecond pulses at 50 W average power, the process is based on the chirped-pulse amplification (CPA) technology [47]. Femtosecond oscillators with Ti:Sa as the gain medium can generate pulse energies on the nJ level, but direct amplification of the pulse to mJ level might cause damage to the crystal. Therefore, the seed pulse are first stretched into hundreds of picoseconds in order to lower its peak power and prevent damage in the crystal, then it passes the gain medium 10

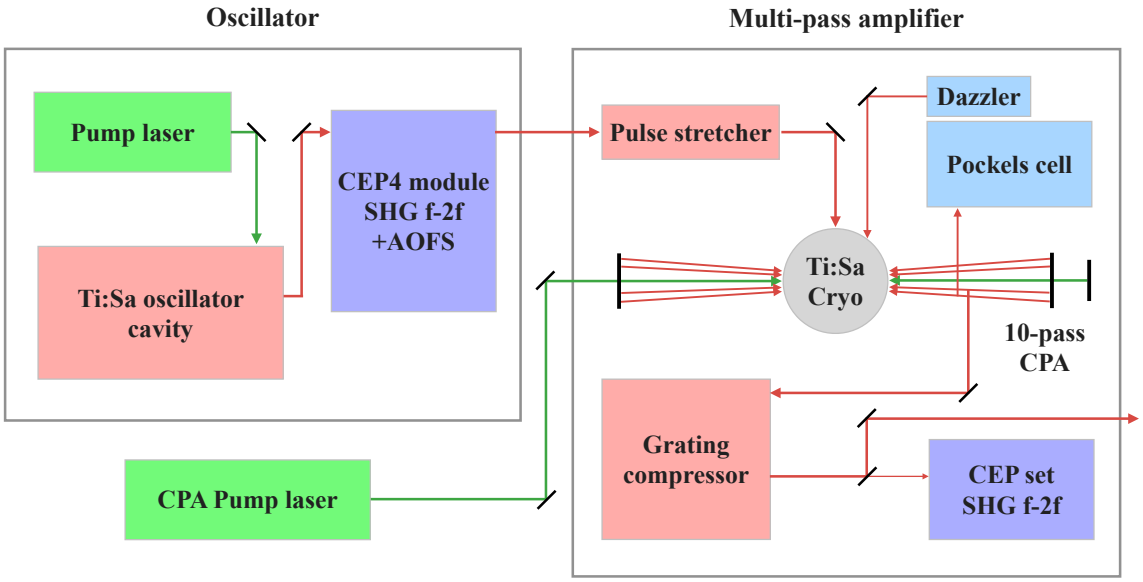

Figure 3.1: Sketch of the laser system for the generation of NIR pulses, which includes an oscillator and multi-pass amplifier. The arrows indicate the propagation of the laser pulse steered by optical mirrors (black bar) through several pulse manipulation states (colored box).

times in total. The amplifier crystal is cryogenically cooled in a vacuum chamber operating at a maximum 10^{-5} mbar, to reduce thermal lensing and damage during operation. After 4 passes through the crystal, the beam is directed through a Pockel's cell, which selects one pulse out of the pulse train synchronized with the pump laser, this lowers the repetition rate of the laser to 3 KHz. The multipass design does not require the use of additional dispersive materials, which is an advantage for generating short pulses. But it is limited by the total number of passes because of the spatial separation of beams, therefore, it is challenging to achieve high conversion efficiency from the pump energy to laser energy.

Then, the pulse amplitude and phase are shaped by the Dazzler (Fastlite), which produces acoustic waves that imprint a programmable phase onto the time phase of the pulse and modify its spectral amplitude. Shaping the spectral amplitude can reduce gain-narrowing in the amplification process. With the Dazzler, one can control the temporal shape of the pulse at the output of the laser system, and even tune the pulse duration at the entrance of the experimental beamline. The last stage of the amplifier is the recompression of the amplified pulses with a grating compressor and chirped mirrors. Then the beam is focused into a hollow-core fiber (HCF). Beam stabilization is achieved by two sets of beam alignment systems with position-sensitive diodes and motorized mirrors to stabilize the pointing of the beam, one is implemented in front of the amplifier and another in front of the fiber.

3.2 Pulse compression and characterization

The 20 fs pulse from the laser requires spectral broadening to reach shorter pulse durations. In our system, it is achieved by guiding the pulse into a gas-filled double differentially pumped hollow-core fiber (HCF) followed by a chirped mirror compressor.

The fiber capillary is 1.5 m long with an inner hole diameter of 310 µm. It is broken in the middle in order to let gas enter the central channel, and both sides are sealed with glue to allow the pumping of the exits. With our pump, we achieve < 10 mbar at both ends. With this configuration, plasma generation at the fiber incoupling will be less, therefore producing a more stable beam mode as well as reducing damage of the entrance window and extending the lifetime of the fiber. Propagation within the fiber can be thought of as the beam being reflected through grazing incidence reflections. And because the losses caused by multiple reflections are higher for higher-order beam modes, the fundamental mode will travel longer distances in the fiber. Our fiber throughput is usually around 4-5 W (50-60% transmission) with a stable beam mode.

The pulses propagating through the HCF is spectrally broadened but also chirped due to dispersion in the conversion medium and the self-phase modulation process. When a plane Gaussian wave propagates through a medium, a nonlinear phase shift is added to the temporal phase of the pulse, in the frequency domain it means new frequency components are added to both sides of the pulse, which broadens its bandwidth. To compress the pulse in time, we employ seven pairs of double-angle chirped mirrors (PC70, Ultrafast Innovations), which introduces a negative GDD of -40 fs^2 per pair. To fine-tune the dispersion, a pair of fused silica glass wedges are mounted on motorized translation stages, which control the amount of glass inserted into the beam path. After compression, we can achieve <5 fs pulse duration.

To characterize a short pulse with its duration on the order of a few femtoseconds, one would need to use a shorter pulse to sample it in the time domain. Therefore, techniques such as autocorrelation are developed, and a laser pulse is split into two, one of which is delayed in time, they are combined and focused into a second harmonic generation crystal. The autocorrelated trace records the delay-dependent second harmonic signal, from which the pulse duration can be estimated. The two most commonly employed methods for measuring the spectral phase are frequency-resolved optical gating (FROG) [48] and spectral phase interferometry for direct electric-field reconstruction (SPIDER) [49]. In this work, the method called dispersion-scan (D-scan) is used, the beam is spatially split into two even parts, and they are both focused into a birefringent crystal for second harmonic generation, and one of the pulses is delayed and scanned over the other pulse. The dispersion of the pulse is controlled by moving the glass wedges mentioned before.

The measured D-Scan trace $S(\omega, z)$ can be expressed by an analytical formula that includes the intensity spectrum and the spectral phase of the fundamental NIR pulse.

$$S(\omega, z) \propto \left| \int_{-\infty}^{+\infty} \left(\int_{-\infty}^{+\infty} E(\omega') e^{ik(\omega')z} e^{i\omega' t} d\omega' \right)^2 e^{-i\omega t} \right|^2 \tag{3.1}$$

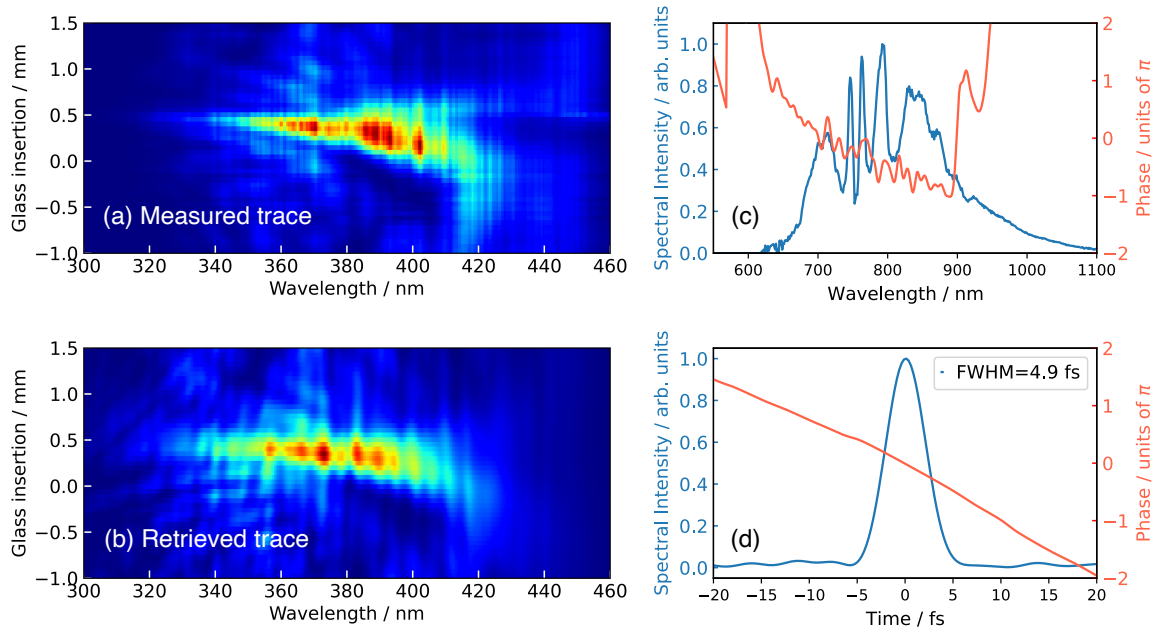

Figure 3.2: Measurement of the pulse duration of the few-cycle NIR pulse by the dispersion scan (D-Scan) setup. (a) The measured D-Scan trace, which is the intensity spectrum of the second harmonic of the laser produced in a nonlinear BBO crystal, it is plotted with different glass insertion of the wedge. (b) The retrieved D-Scan trace from an iterative algorithm. The trace is obtained after 15000 iterations. (c) The measured intensity spectrum of the laser pulse and the retrieved spectral phase for the best wedge position. (d) The retrieved pulse shape for the short-pulse optimized wedge position, its full width at half maximum is ∼5 fs.

We measure spectra with time delay, and the spectral phase can be reconstructed via iterative algorithms [50, 51]. By scanning the wedge position, one finds the spectrum will be broadest when the shortest pulse is generated at the BBO crystal with the optimum amount of GDD introduced by glass wedges. During the experiment, the wedge will be further fine-tuned by monitoring live harmonic signals.

Fig. 3.2 shows an example of a spectral trace of the SH signal. In the figure one can see for a certain wedge position, the spectrum is broadest because the GDD introduced will generate the shortest pulse at the BBO crystal.

3.3 Experimental setup for absorption and streaking

With the laser and pulse compression system described above, it is able to generate attosecond pulses for experiments in the vacuum beamline. The vacuum experimental setup for HHG and time-resolved measurements is shown in Fig. 3.3. More details of the beamline are given in

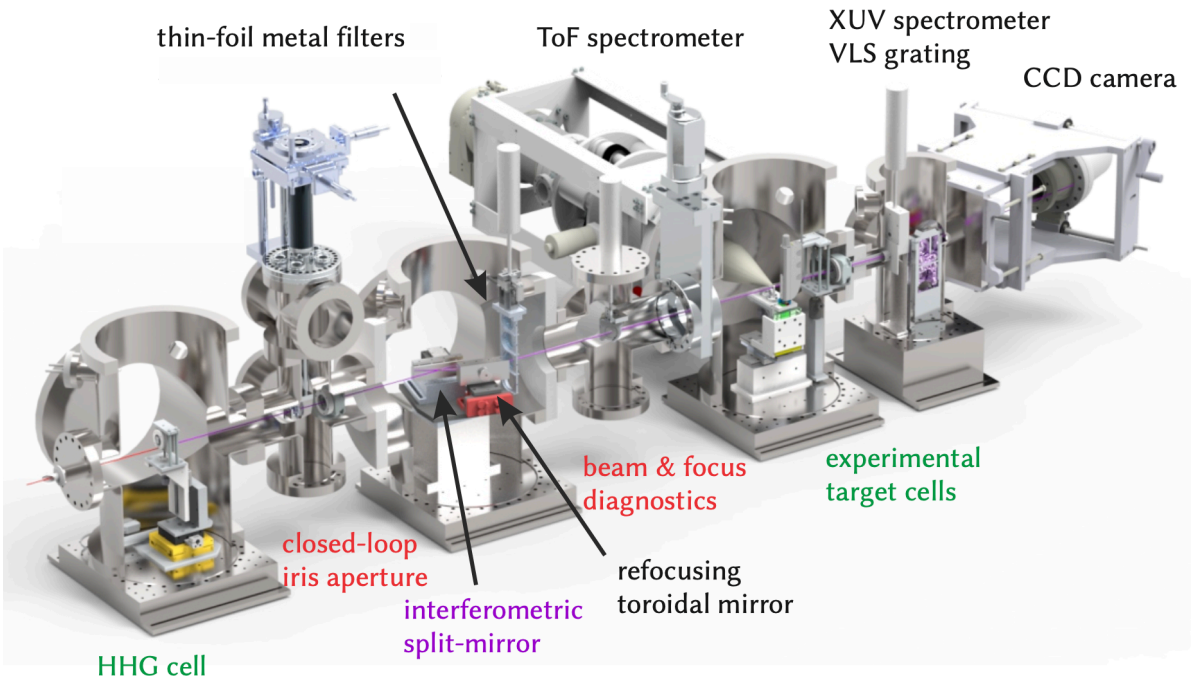

Figure 3.3: CAD drawing of a cut through the vacuum beamline. The HHG and target are in separate chambers to enable differential pumping between the chambers. Details about the purpose of each component can be found in this section. The figure is adapted from reference [52].

Stooß et al [52]. Modifications added to the beamline in order to perform streaking measurements will be presented in the following sections.

There are several general requirements for NIR laser pulse to generate an attosecond pulse, which are all being met with our apparatus. The intensity in the focus on the gas target should be on the order of 10^{14} W/cm^2. And, the corresponding pulse energy usually needs to be higher than 100 µJ to avoid tight focusing. Also, pulse duration needs to be sufficiently short, ideally in the few-cycle regime to generate single, isolated attosecond pulses. Additionally, the CEP should be stabilized, or else there will be a shot-to-shot variation of the attosecond pulses because they are generated every half laser cycle and more than one pulse might be generated if the CEP is shifted. For detection purposes, the repetition rate of the laser is preferred to be on the kHz level. The attosecond streaking experiment measures photoelectrons, and there exists an upper limit on the electrons per shot to avoid the space-charge effect.

3.3.1 Carrier-envelope phase stabilization

The carrier-envelope phase (CEP) of the laser pulse is the phase offset between the carrier and envelope of the electric field of the pulse. For a linearly polarized field, when $\varphi_{CE} = 0$,

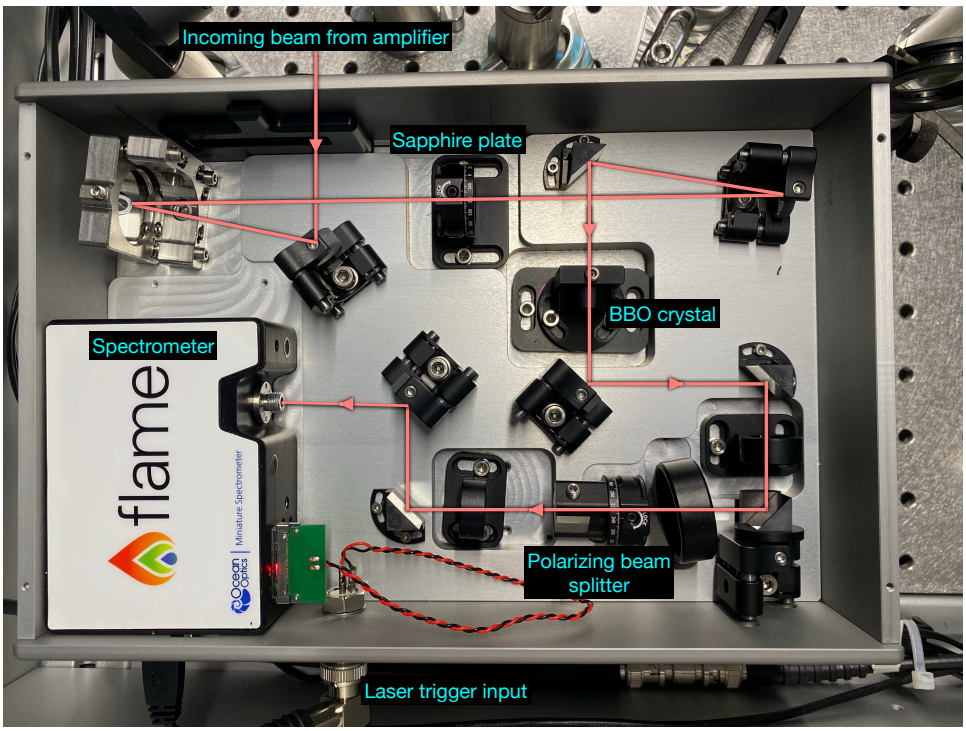

Figure 3.4: Schematic setup of the f-2f interferometer. The most important components are labeled, other unlabeled optics are steering and focusing mirrors.

the maximum of the electric field is at the maximum of the pulse envelope (see Fig. 2.1 (a)). Processes that are sensitive to the electric field strongly depend on it. The CE phases of the amplified laser pulse were first stabilized by [53].

Fast fluctuations of the CEP are stabilized by the CEP4 module after the oscillator as mentioned in 3.1, however, the long-term drifts require the use of a second CEP stabilization module placed inside the amplifier. CEP4 module can select pulses with identical CE phase with a pulse picker and send to the amplifier, however, pulse-to-pulse CE phase variations can still be introduced by components in the subsequent spectral broadening and compression stages. We have additional control of this CE phase by adjusting the dispersion of the amplifier through active feedback to the fused silica slabs in the stretcher, the CEP signal of our system can be measured inside the amplifier as shown in Fig. 3.1 or in front of the beamline.

The module consists of a f-2f interferometer as shown in Fig. 3.4 and a piezo-controlled glass wedge inside the amplifier to change the CEP. A small portion of the amplifier beam (about 25 mW) is sent into the f-2f-interferometer to produce an interference pattern, which will be measured with a USB spectrometer to calculate the CE-phase of the laser pulses. The sapphire plate is for filamentation and white-light generation to broaden the spectrum so that it covers an octave [54]. Then beam is focused into the BBO crystal, which can be rotated to tune the phase matching angle to generate second harmonic of the input light. Rotating the BBO crystal with respect to the beam equals shifting the second harmonic in the frequency

axis. The polarizer is used to project the second harmonic and fundamental light into the same polarization axis to form interference, in the end, fringes will be detected by the spectrometer.

For our setup, the interference pattern appears around 550 nm, and then the spectral phase of the fringes will be obtained with Fourier transformation to calculate the relative CEP value from the desired value. A histogram of the measured CEP value is also recorded and fitted by a Gaussian fit function to give the standard deviation, during streaking experiments the RMS is around 200 mrad.

Another option for our setup is another f-2f interferometer in front of the beamline. The small portion of the beam that is not transmitted from the 45° fused silica glass entrance window will be steered into the interferometer, the control of the CEP is still realized by the components inside the amplifier. However, the beam after the amplifier undergoes a long propagation distance, and it will be influenced by nonlinear processes in the fiber causing the CEP to fluctuate, therefore it would be ideal to be able to control the CEP after the fiber. For future improvements, one could use the glass wedges after the fiber to fine-tune the dispersion.

One possible method to stabilize the slow-drifting CEP, which has yet to be implemented, is to add a phase shifter to the laser system, which can provide a controllable phase to the RF signal. This device can be added in between the electronic signals of the CEP4 module.

3.3.2 High-harmonic generation

The first step inside the vacuum chamber is to generate attosecond pulses via high-harmonic generation, its process is explained with the semiclassical three-step model in section 2.2.2. The 1 mJ, sub 5 fs NIR pulses after the chirped mirrors are focused on a rare-gas medium. Rare gases have high ionization potential, which suppresses depletion in the leading edge of the NIR pulse and allows HHG in the high intensity parts of the pulse. The focusing mirror (f=500 mm) sits in front of the HHG vacuum chamber, it is hit under near incidence angle to reduce astigmatism of the beam in the focus. The focal size is around 50 µm with peak intensity in the range of $10^{14} - 10^{16}$ W/cm^2. The gas cell is made of ceramic Macor with a hole that is 200 µm wide and 3 mm long for the beam to focus through. The gas conversion medium used in this experiment is neon, with a backing pressure of 100 mbar, and the corresponding chamber pressure is on the level of 10^{-3} mbar. The cell is on a home-built precision stage that can be moved in all XYZ directions to adjust for optimal phase-matching conditions during the HHG process, the stages are controlled outside the vacuum.

There are several methods for the generation of a single attosecond pulse because it is an important step in time-resolved spectroscopy. One is to use a linearly polarized driver pulse in the single-cycle regime so that the harmonics emitted at the peak of the pulse are naturally confined to half the laser cycle. Another is the gating method [55, 56] with pulses whose polarization changes with time, because the attosecond generation efficiency strongly depends on the ellipticity of the driving pulse [57], attosecond pulses can only be produced by the center portion of the NIR pulse, usually the duration of the temporal gate is shorter than the input pulse

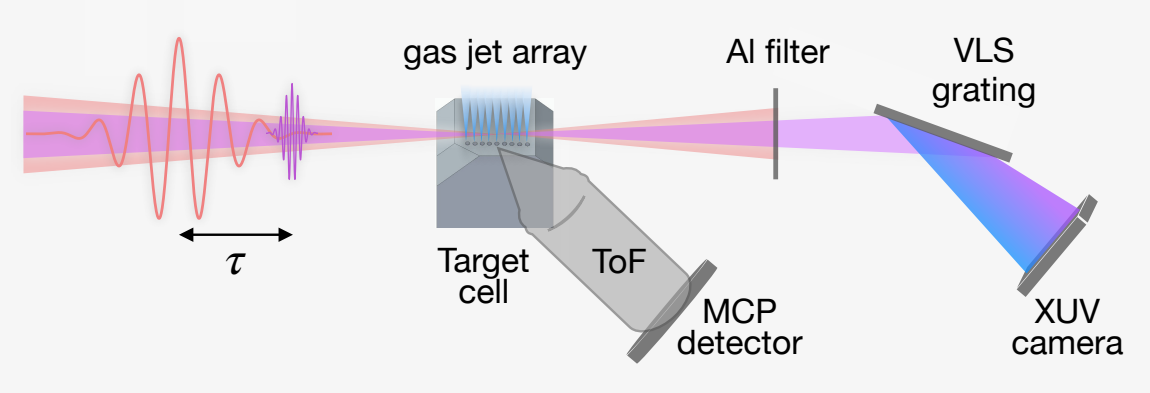

Figure 3.5: Schematic of the experimental setup after intensity and time-delay control. The XUV and NIR co-propagates and are spatially and temporally separated by the split mirror and filters. Then the pulses interact with the target gas and pass through Al filter to block the NIR beam. At the end, the XUV spectrum is measured using a flat-field spectrometer consisting of a VLS-grating and a CCD camera, the photo-electrons are measured by a time-of-flight and MCP detector.

[58]. In our experimental setup, we employ ionization gating [59], which suppresses harmonics in the tail of the driver NIR pulse as a result of ionization and depletion of the ground state in the leading edge of the pulse. However, note this scheme does not restrict the emission of weak attosecond pre-pulses, therefore, we are not strictly speaking in the single attosecond pulse regime.

3.3.3 Pulse control and interferometry

The newly generated XUV beam will co-propagate with the NIR and pass through an iris, metallic filters, an interferometric mirror unit, and then a toroidal mirror, with this configuration, XUV, and NIR will be separated both spatially and temporally and refocused into the target chamber 1.4 m downstream.

The XUV has a shorter wavelength than the NIR beam, therefore smaller divergence along the beam path. Due to this property, one can control the NIR intensity by concentrically cutting off the beam with an iris without influencing the XUV beam, and also insert a temporal delay between the two pulses by varying their relative optical paths. This is realized by an iris aperture, two grazing incidence mirror assemblies (one for temporal pulse separation and one for refocusing the beam into the gas target), and a variable filter array for spatial pulse separation.

The iris is a motorized and closed-loop zero aperture iris, one can estimate the intensity of the target by coupling out the beam and measuring its power and focal spot size. The two grazing-incidence mirrors are hit under an angle of 15°, where the angle is chosen as considering both reflectivity and alignment. The first split mirror assembly consists of a silver-coated outer mir-

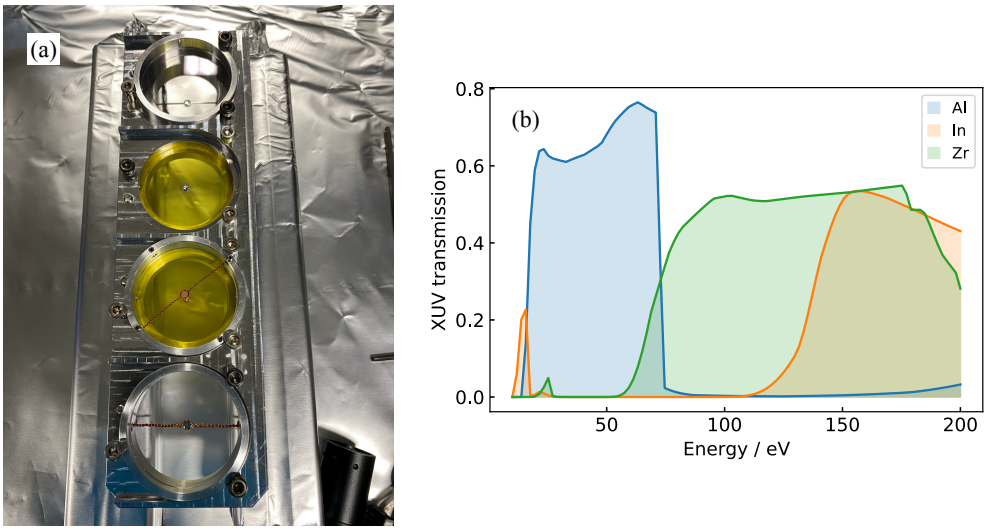

Figure 3.6: The concentric filter for the spatial separation of the NIR and XUV pulses and the XUV transmission curves of the metallic filters in our filter assembly. (a) The filter assembly in the vacuum chamber, it is on a mount that can be shifted in all dimensions inside vacuum during alignment. (b) Different metallic materials for the 200-nm-thin transmission filter can be used for different spectral regions of the XUV from 12 eV using indium (In) to aluminum (Al) around 50 eV up to 200 eV using zirconium (Zr). The XUV transmission data are taken from reference [60].

ror which reflects the NIR beam and a movable high-quality boron carbide (B_4C) coated inner mirror for introducing time-delay. The 2 mm $\times$ 100 mm small inner mirror is connected to a piezo stage, its stability determines the temporal resolution of absorption measurements. From measuring interference fringes formed between the inner and outer mirror of a reference laser (continuous wave helium-neon-alignment-laser), one quantifies the interferometric stability to be 26 as. Next is the gold-coated toroidal mirror, the coating supports the XUV reflectivity for a broad spectral range.

Last, we have a two-component band-pass filter in annular geometry for spatial separation of the XUV and NIR beams. One filter assembly consists of a small rounded metal filter in the center to block all NIR in that beam region, and a thin membrane surrounding the metal piece which transmission is high for NIR light and low for XUV radiation. In the beamline, there are four filter assemblies with different materials (depending on the interested XUV spectra region) in a column on a mount that allows it to move in and out of the beam path as well as switch between different filters without breaking the vacuum. The metallic foil with a diameter of 2 mm is glued onto a home-built twisted Kapton wire or is directly glued onto a Kapton foil with a central hole. The foil or the wire is mounted on a 4 cm outer diameter aluminum ring, which is held in place by a variable and in a vacuum movable support array, see Fig. 3.6(a).

The selection of the metallic filter depends on the photon energies of the XUV pulse and the investigated photon energies of the target. In Fig. 3.6, the transmission curves of 200 nm thick

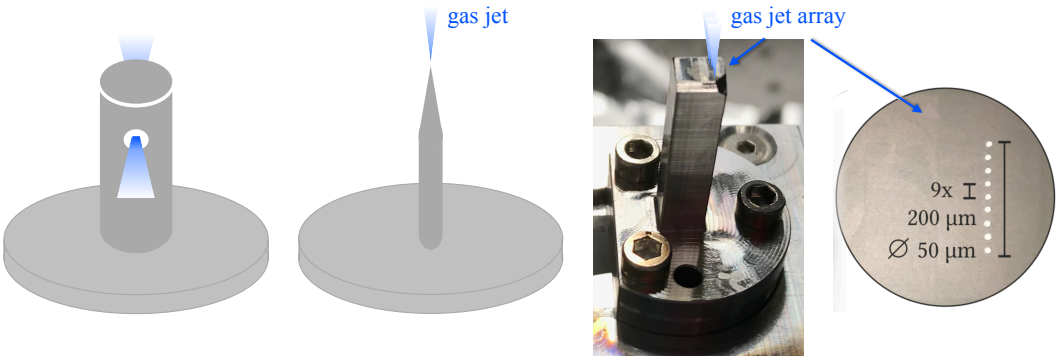

(a) Standard absorption cell (b) Standard streaking nozzle (c) Target cell for simultaneous absorption and streaking measurement

Figure 3.7: Different target cell geometries. (a) A standard absorption cell made of ceramic, gas exits from both holes in the laser propagation direction. (b) A glass nozzle for streaking measurements, gas jet is formed at the tip of the nozzle. (c) The full steel target cell used in this experiment, nine holes of 50 μm in diameter are drilled into the top of the cell. A gas jet array is formed in the laser propagation direction to increase the path-length-density-product.

aluminum, indium, and zirconium are shown. Here, we study the doubly excited helium states around 60 eV, thus aluminum (Al) is used. Indium (In) can be used for low harmonic energies between 12 and 16.5 eV, and zirconium (Zr) for energies between 72.5 and above 200 eV.

In our current setup, the same NIR is used for HHG generation and the interferometric step. Due to the geometry of the split mirror and target cell, the total delay range between NIR and XUV is limited. The polarization of the NIR light cannot be easily changed, which is related to current isolated attosecond generation techniques. An external incoupling of the NIR pulses was designed and implemented to enable more variability in our interferometric measurements [61].

3.3.4 Target cell

The target gas regimes required for absorption and streaking are different, thus a new target cell design is implemented to meet both pressure conditions. For absorption spectroscopy, usually, tens of millibars of backing pressure is used, leading to the target chamber pressure of about 10^{-3} mbar. While the MCP detector used for streaking has to be operated in the pressure better than 8×10^{-6} mbar. Although the small entrance of the ToF spectrometer serves as differential pumping between the chamber and the detector, it is still not sufficient to satisfy the conditions for both measurements. The different target cells are shown in Fig. 3.7.

The most commonly used streaking cell is a nozzle, which is a glass-needle-like capillary with a small hole on the tip, with the target gas exiting from the tip forming a gas jet. The

beam will be focused into this region ionizing the atoms or molecules, then the electrons will mostly fly in the direction perpendicular to the beam direction. The absorption target cell is similar to the HHG cell, with no hole in the perpendicular direction of the laser which means the freed electrons will be blocked by the cell itself. However, if one uses the streaking gas jet and performs absorption measurements, the target density will be too small to see a signal.

Thus to meet the requirements of our measurement, one needs to increase the target density while maintaining a low chamber pressure. It can be achieved with pulsed atomic or molecular beam [62, 63], which uses fast-acting valves with skimmers and synchronized with the laser's repetition rate to produce short pulses of gas. However, these cell designs are either expensive or requires a considerable level of expertise and increases the complexity of the measurement.

The new cell implements a gas-jet array, which increases the absorption path length while maintaining the pressure requirement for the MCP detector. Tests of the target cell backing pressure, target chamber pressure, pressure at MCP, and absorption signal are performed to select the optimum parameters for the experiment. The initial version was implemented by drilling holes into standard aluminum foils that were glued on top of a prototype cell, the foil was able to withstand backing pressures up to 1 bar. The resulting increase in the path-length-density-product compared to a single gas jet allowed for the observation of the first five resonances of the $2s2p$ series of autoionizing states in helium [64]. However, the aluminum foil is too easily burnt in the laser focus, so a full steel cell was constructed for further measurements. On the side of the cell facing the laser's incoming direction, the corner is cut off forming a 45deg surface facing outwards, this is for calibrating the time-of-flight zero which will be discussed in section 4.2.1.

3.3.5 Detection gas

As mentioned in section 3.2, methods have been developed for the complete characterization of the temporal structure of the NIR pulse. However, for attosecond light pulses in the XUV range with moderate intensities, using nonlinear-optical effects for characterization is challenging, thus other attosecond measurement techniques have been developed that fulfill this purpose. It is done by ionizing atoms via single-photon absorption, which process generates an attosecond electron pulse which is a replica of the attosecond XUV pulse, and the phase and amplitude information of the XUV field are transferred to the photoelectron wave packet.

The electron replica of attosecond XUV pulses is generated within the detection gas via photoionization. Usually, the XUV flux is low, thus the target gas should have a large absorption cross-section to produce as many photoelectrons as possible [65]. The ionization potential of the atom should be high enough so that the photoelectrons produced by the XUV are much larger than the number of electrons generated by the NIR laser via above-threshold ionization. Because of this, noble gases are commonly chosen as gas targets, in this work helium is used.

3.3.6 XUV spectrometer

The spatially and temporally separated XUV and NIR pulses interact with a gas target, and the NIR beam will be blocked by another 200 nm thick aluminum filter before the gratings. There exist two interchangeable concave variable line spacing (VLS) gratings for the spectral range 10-56 eV and 20-112 eV, they can focus the spectra on a flat-field which does not blur with a flat-chip camera. The camera is a thermo-electrically cooled, back-illuminated CCD with 1340×400 pixels with a size of 20 µm×20 µm. Arbitrary region-of-interest (ROIs) on the chip can be selected for binning to speed up data recording and transmission. The camera sits on a custom-built mount that moves along the imaging plane to cover different spectral regions. The overall resolving power of the spectrometer is $E/\Delta E > 1500$. The adjustment of the distance between the grating and camera and the orientation of the camera with respect to the spectral plane is used to improve the spectral resolution.

3.3.7 Electron time-of-flight spectrometer

To measure photoelectron spectra produced by the XUV attosecond pulses, a time-of-flight (ToF) spectrometer is the most commonly used electron spectrometer. Its working principle is to measure the flying time of the electrons with different momentum from their point of generation, this allows time-resolved detection of the arriving electrons with decent resolution. There are some main specifications of ToF:

- The range of the measured electron energy: it is related to the spectrum of the attosecond XUV pulse generated via HHG and the metallic filters used in the beamline.
- The energy resolution: the relative energy resolution for electron energy E and drift tube length L_{drift} is given by [66]

$$\frac{\Delta E}{E} = \frac{\sqrt{8}}{\sqrt{m_e}} \frac{\Delta t}{L_{drift}} \sqrt{E}. \tag{3.2}$$

- The acceptance angle: it is dependent on the distance from the interaction point to the MCP plate and the size of the MCP plate.

The spectrometer in our setup is the field-free ToF spectrometer for electron and ion spectroscopy from Stefan Kaesdorf [67], only the electron detection parts are used in our case. The main parts, shown in Fig. 3.8 (a) from left to right, consist of an entrance piece, Einzel lens, drift tube, microchannel plate (MCP), and an anode plate, the two tubes perpendicular to the main tube are for vacuum pump and pressure sensor installments.

The original entrance piece is the entrance aperture of the entrance piece (Fig. 3.8 (b)) is home-built with titanium, size of the 1 mm circle opening in the front is selected while considering differential pumping and acceptance angle. The need for differential pumping has been mentioned in the previous section, however, the hole cannot be as small as a skimmer, or else the photoelectron count rate will be lost from the beginning. The size of the first MCP

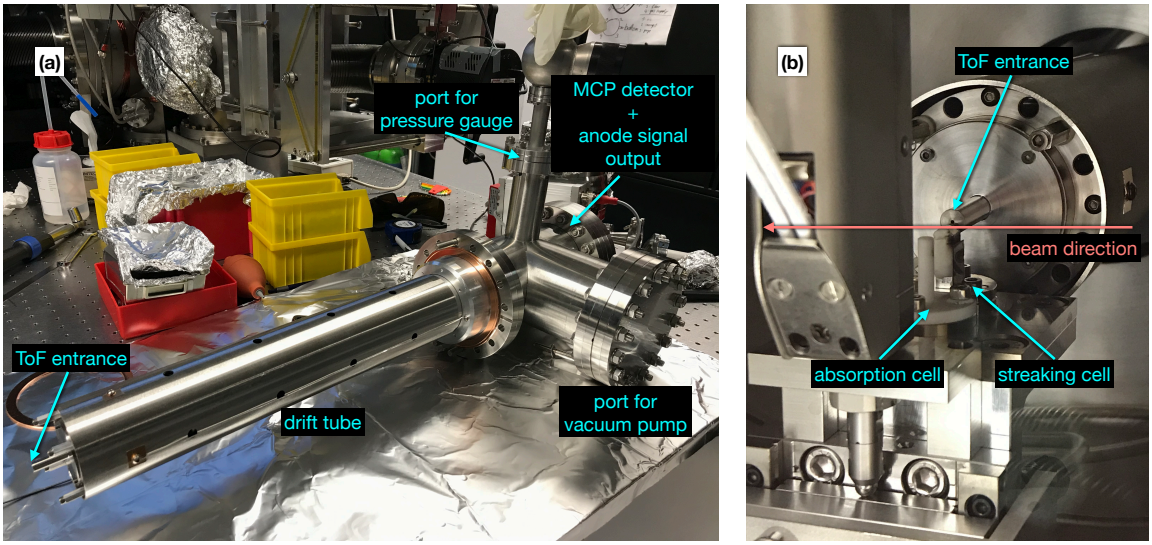

Figure 3.8: The electron time-of-flight (ToF) detector from Stefan Kaesdorf and the layout of the cell inside the chamber. (a) The detector before mounted to the vacuum beamline. (b) Shows the position of the target cell and the ToF entrance during experiment, the laser propagation direction and ToF entrance are perpendicular to each other.

plate and distance from the interaction region gives the acceptance angle, thus the entrance hole should be big enough to not affect the angle. The Einzel lens is a charged particle electrostatic lens that focuses charged particles without changing their kinetic energy, in our setup it is on positive potential (max. output 1000 V) and allows an increase to the acceptance angle of the spectrometer by more than one order of magnitude. The drift tube is 50 cm long, and has the possibility to apply positive or negative voltages up to $\pm$ 180 V, in positive mode it is equivalent to making the time-of-flights longer which may be an advantage for electrons energies >200 eV, and negative mode increases the sensitivity for slow electrons. The drift tube is encapsulated in a μ-metal (material with large magnetic permeability) shield to prevent penetration of external magnetic fields into the drift region, for instance, it can avoid the earth's magnetic field dragging the electrons downwards.

The principle of an MCP detector is similar to an electron multiplier, which intensifies single particles by the multiplication of electrons via secondary emission. While MCP has many tiny tubes (microchannels) stacked parallel together, the microchannels are typically a few micrometers in diameter and have a small angle to the surface so that the entered electron is guaranteed to hit the walls of the channel. By applying a strong electric field across the plates, each individual microchannel cascades one electron into a cloud of electrons. Afterward, the microchannel takes some time, usually on the order of nanoseconds, to recover before it can detect another signal. The electrons exit the channels on the other side of the plate and are collected by an anode, then the feedthrough signal will enter a series of electronics that amplify and convert the electronic signal into an analog signal and feed to LabView programs which

will be introduced in the next section.

In our setup, there is a two-stack channelplate with a 40 mm diameter and a pore size of 5 μm for faster response. It should be operated in a vacuum better than 8×10^{-6} mbar and the system be pumped for longer than 3 hours. To measure the vacuum pressure at the MCP region, hot cathode ionization gauges should be used, and it is important to switch off the pressure gauge before activating the MCP because it will produce a large background causing the MCP to saturate and get destroyed. The detector should be kept under vacuum because it will be destroyed if staying in atmosphere for more than a few days. The ToF tube and MCP detector are attached to a manipulator that allows movements in all XYZ directions for alignment.

It is important to collect as many electrons as possible and maintain high energy resolution over a wide energy range. However, energy resolution decreases rapidly with increasing acceptance angle. A technique namely the magnetic bottle would help [68], it can collect electrons from all emitted angles from the interaction region by implementing an inhomogeneous magnetic field which is equivalent to a collimating magnetic lens. However, there is another cell next to the ToF cell making it not possible to implement one in our setup. One could also add Helmholtz coils to the outside of the target chamber to overcome the Earth's magnetic field or to act similar to a magnetic bottle to collect and direct more electrons into the ToF detector.

3.3.8 Signal processing of the MCP detector

Signal from the anode is coupled out by feedthroughs, and amplified by a fast amplifier (FTA 820, Ortec), then converted to standardized NIM pulses by a constant fraction discriminator (CFD). The CFD is able to count narrow pulses at very high count rates, and marking the arrival time of the detected events with precision and consistency is its primary function. It gives a timestamp based on the time of the rising edge of the signal pulse shape reaching a certain percentage of its pulse amplitude, which will be used as the stop signal for the ToF measurement signal. More importantly, the time resolution of the signal is mainly limited by jitter, walk, and drift, which can be minimized by adjusting the discriminator threshold on the leading- or falling-edge of the analog pulse. Then it launches a normal pulse, where the timing information is transferred to a more robust type of signal, and enters a level adapter (LeCroy) to convert the input NIM pulse to a low voltage TTL output pulse with the same width, where the input time-jitter performance is fully maintained without the typical drawbacks of the passive pulse inverters at high pulse rates. The nuclear instrument modules (NIM) is a standard modular instrumentation system, transistor-transistor logic (TTL) is a logic family that relies on circuits built from bipolar transistors, from NIM to TTL the signal will be reversed in amplitude.

At last, the signal will be the analog input for the time tagger together with a laser trigger for the acquisition of the time-of-flight information. The time tagger 20 module from Swabian Instruments is a versatile multi-channel time-to-digital converter with timing resolution down to 3 ps. The time events are recorded within a programmable time window which should be determined experimentally, in this setup the laser trigger serves as the start time and timestamp

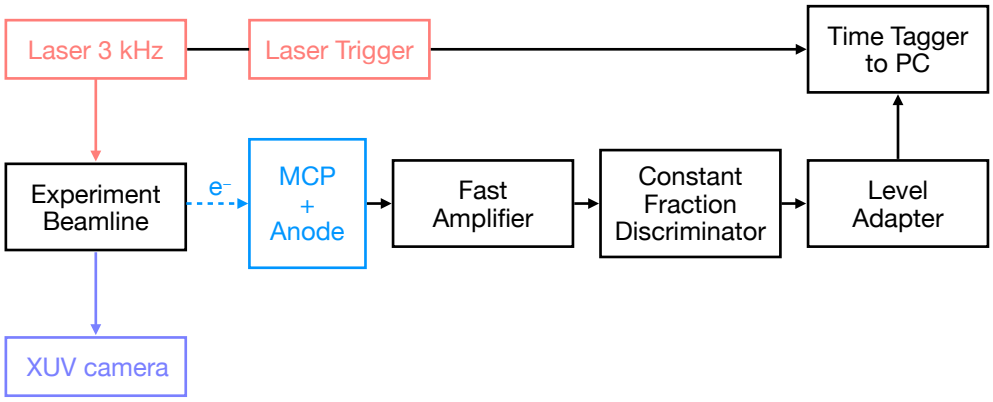

Figure 3.9: Illustration of electronics in the signal processing of streaking measurement. The read-out electronics are housed in a standardized NIM rack, which serves as their power supply.

from CFD as the stop time, and the work cycle starts again on the next laser trigger. For each time-delay, the events are binned in a histogram by the software provided with the module producing time-of-flight spectra. A LabView VI for our beamline synchronizes both the time-delay piezo and data acquisition from the time tagger module.

The time-of-flight spectra will be converted to kinetic energy by the relation

$$E_{kin} = \frac{m_e}{2}\left(\frac{l}{t - t_0}\right)^2 \tag{3.3}$$

where l is the distance from the interaction region of the target, t_0 is the constant offset of the trigger. However the ToF detector has the option to apply voltage to the drift tube and Einzel lens, which is equivalent to increasing the distance l.

Chapter 4

Data processing and calibration

4.1 Novel simultaneous measurement of attosecond transient absorption and attosecond streaking in helium

We simultaneously measured the resonant photoabsorption spectra of the laser-coupled doubly excited states in helium, together with the streaked photoelectron spectra. In section 3.3.3, the pulse propagation and interferometric layout are explained, and the pump-probe pulse for absorption and streaking spectra share the same mirror that introduces time-delay. Thus, this novel experiment method can be used to calibrate the absolute time-delay zero of absorption spectra. Experiments that combine these two spectroscopic methods either use two different target gas cells and separately record spectra one after another [69], or the target investigated is solid material [70–73], or use a two foci geometry for solid targets [74]. It is to the best of my knowledge the first time that our measurement has been performed in the same gas target for both transient absorption and streaking. Since the two experiments can be performed simultaneously, precise pump-probe delay calibration can be achieved, thus opening the possibility for a new class of attosecond experiments in gas targets.

4.2 Data processing for streaking

Fig. 4.1 shows the raw measured electron spectra with respect to time delay, each delay step is integrated for 1 s. The CEP rms is stabilized to around 200 mrad. The spectra are integrated over all delay steps to illustrate the distribution of electrons in the spectra. The peak with the highest counts comes from the electrons released from the atom, it is the signal. The wide distribution that follows comes from NIR light scattered by the target cell itself, it was recognized by varying the iris aperture in our beamline. There exists another small peak before the arrival of the main signal, however in the trace is not visible with the current color scale without saturating the oscillating streaking trace. This tiny peak and the rising edge of the highest main peak are used for momentum calibration discussed in the next section.

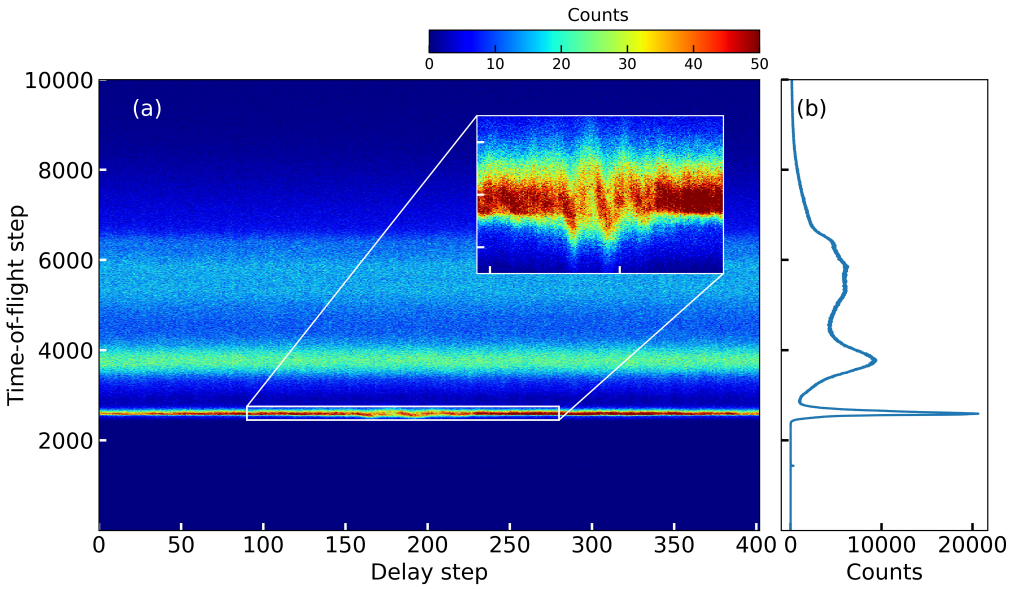

Figure 4.1: Measured streaking trace (a) with 1 s integration time and the spectrum (b) integrated over all delay steps, the inset plot is zoomed in on the trace. The axes indicates step size, it will be converted into time delay and energy in the following analysis.

4.2.1 Pre-algorithm processing

The spectrometer records the flight time of the electrons, which needs to be mapped to the energy domain. The streaking cell with a needle tip allows direct electrons to reflect from the curved surface when it is in the light path of the laser and enter the detector, this gives the timestamp of delay 0. The cell used in this experiment, shown in Fig. 3.7, has a flat 45° cut surface for reflecting the direct electrons that leave the interaction area when some small portion of the NIR laser hits the target cell. The difference in flying time between direct electrons and arrival of the main signal is inserted into Eq. 3.3 to obtain a calibration curve between flying time and kinetic energy of the electrons, the energy-calibrated spectra is plotted in Fig. 4.3.

Another step before inserting the trace into the retrieval algorithm is to isolate the main peak from the unwanted signal, i.e. the long tail of the electron distribution. It is done by first integrating the spectra over a range where XUV and NIR do not overlap, then smoothing the spectra, as shown in Fig. 4.4 (a), and taking the gradient to find the local minimum in the region where the two signals intersect. Then use the index of this minimum as the center for a Sigmoid function to be multiplied to the spectrum, this will produce a smooth edge rather than a sharp cut-off which then would be an artificial edge and challenging for retrieval algorithms. The retrieval algorithms usually use the central momentum approximation, which means the center of the streaked trace in energy should be larger than its width. If the measured trace includes the lower energy electrons, it might lead to the algorithm not converging. Also, if there are other

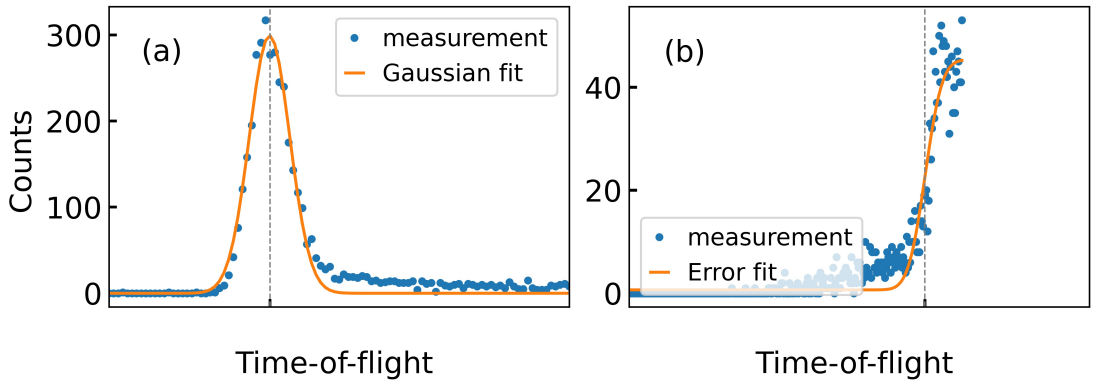

Figure 4.2: Fitting of the measured data for time calibration. (a) The measured spectrum is integrated over all delay steps and then fitted with a Gaussian function, the maxima of the fit (grey dashed line) gives flying time 0. (b) The measured spectrum is integrated over the unstreaked spectra and then fits the rising edge with a Gaussian error function, the middle of the fit (grey dashed line) gives the energy of aluminum edge at 72 eV minus the ionization potential of helium 24.6 eV.

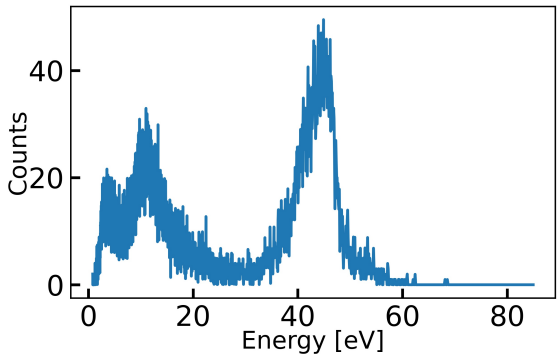

Figure 4.3: An example of the energy-calibrated electron spectrum of one delay step. Due to the fact that shorter flying times corresponds to higher momentum, the rising edge in Fig. 4.2(b) becomes the falling edge at around 50 eV.

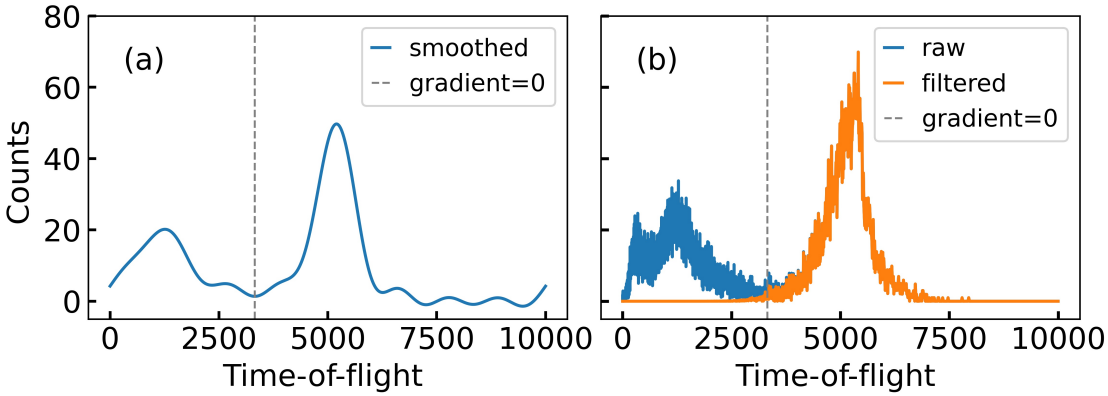

Figure 4.4: Illustration of the intermediate steps to remove low-energy electron distributions for a single time-delay step. (a) The smoothed spectrum, index of the local minimum in the spectrum is indicated by the grey dashed line, this index will be the center position for the Sigmoid filter multiplied to the spectrum. (b) The original spectrum is plotted in blue, orange denotes the filtered spectrum.

band-like structures adjacent to the main signal, then the algorithm might retrieve a double pulse or a pulse with a long tail. Thus it is necessary to apply the above-explained method to each delay step to obtain a clean streaking trace as plotted in Fig. 4.5 (b). The trace is then ready to be inserted into retrieval algorithms, the one chosen is introduced in the following section.

4.2.2 The retrieval algorithm ePIE

The TDSE can be solved analytically within the strong-field approximation (SFA) in order to describe strong-field laser–atom interactions [75]. Under SFA, it is assumed that the intense laser field ionizes the ground-state electron directly into the continuum while neglecting the effects of excited states. The influence of the Coulomb potential of the parent ion on the electron motion after it has been ionized is ignored. As a result, the photoelectron spectrum $S(p,\tau)$ as a function of electron momentum p and time delay τ between the XUV and NIR electric fields can be written as

$$S(p,\tau) = |\int dt\, E(t)\, d(p + A_{NIR}(t-\tau))\, P(t-\tau)\, e^{i(\frac{p^2}{2}+I_p)t}|^2, \tag{4.1}$$

where the XUV electric field $E(t)$, the XUV dipole transition matrix element $d(p)$, the NIR gate function $P(t)$ and the ionization potential I_p are all in atomic units. The negative delay corresponds to the NIR pulse arriving first. $P(t)$ is the pure phase-gate function $P(t)$ given by

$$P(t) = exp\left[-i\int_t^\infty dt' \left(p_c\, A_{NIR}(t') - \frac{A_{NIR}^2(t')}{2}\right)\right], \tag{4.2}$$

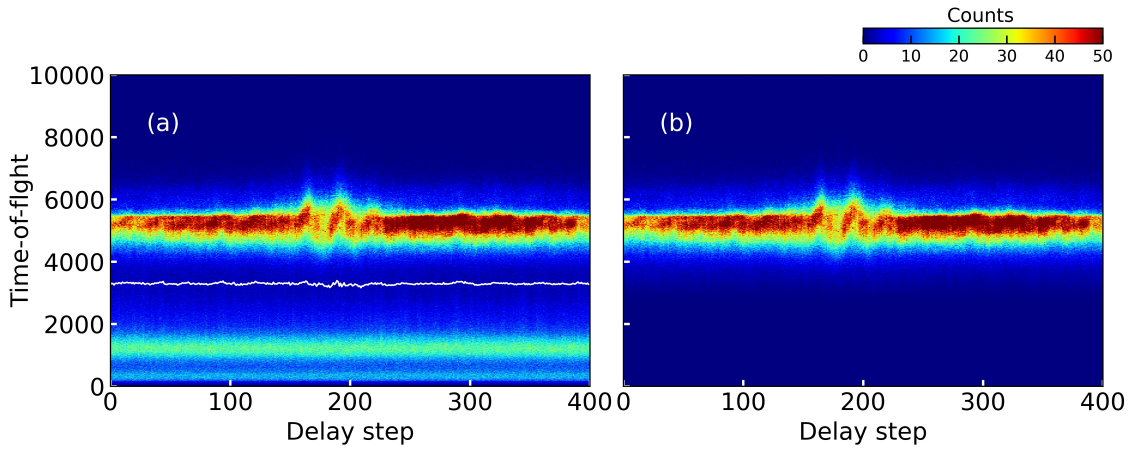

Figure 4.5: Comparison of the trace before and after spectrally filtering out the low energy electrons. The white line drawn in (a) is obtained from the intermediate filtering step explained in Fig. 4.4(a).

where p_c is the unstreaked central momentum and $A_{NIR}(t)$ is the vector potential of the streaking field defined by

$$A_{NIR}(t) = -\int_{-\infty}^{t} dt'\, E_{NIR}(t'). \tag{4.3}$$

The temporal information of the electric fields are embedded in the spectrogram $S(p,\tau)$, with iterative reconstruction algorithms, the XUV pulse shape and duration, and the delay axis can be fully retrieved. Most conventional reconstruction algorithms are based on the FROG-CRAB method, for instance, principle component generalized projections algorithm (PCGPA) [76, 77] and least-squares generalized projections algorithm (LSGPA) [78],

The algorithm is called extended ptychographic iterative engine (ePIE) is adapted from ptychography, which reconstructs phase and amplitude iteratively from far-field diffraction measurements of a real space object [79, 80]. The initial inputs are XUV field $E(t)$ with random white noise and a reasonable NIR gate function $P(t)$, then the streaking time domain response $\xi_{j,n}(t,\tau_n)$ at a certain delay τ_n will be calculated through

$$\xi_{j,n}(t,\tau_n) = E_{j,n}(t)P_{j,n}(t-\tau_n). \tag{4.4}$$

Hereby, n is the index of time delay and j is the global iteration step of the algorithm. Then, one replaces the modulus of the calculated frequency-dependent trace with the square root of the measured spectrogram $\sqrt{\tilde{S}_n(\omega,\tau_n)}$, then inverse Fourier transforms it back to the time domain to obtain a new $\xi'_{j,n}(t,\tau_n)$. In the next step, the XUV pulse will be updated with

$$\begin{aligned} E_{j,n+1}(t) = E_{j,n}(t) + \beta_E \frac{P^*_{j,n}(t-\tau_n)}{\max\left(|P_{j,n}(t-\tau_n)|^2\right)} \\ \times[\xi'_{j,n}(t,\tau_n) - \xi_{j,n}(t,\tau_n)], \end{aligned} \tag{4.5}$$

where the iteration parameter β_E only takes values between 0 and 1. Similarly, the gate function is updated starting from

$$\xi_{j,n}(t,\tau_n) = E_{j,n}(t+\tau_n)P_{j,n}(t). \tag{4.6}$$

Similar to previous step, $\xi_{j,n}(t,\tau_n)$ is Fourier transformed, then the modulus is replaced by the square root the the corresponding spectrum and the new function $\xi'_{j,n}(t,\tau_n)$ is used to update the new estimate of the gate function

$$\begin{aligned} P_{j,n+1}(t) = P_{j,n}(t) + \beta_P \frac{E^*_{j,n}(t+\tau_n)}{\max\left(|E_{j,n}(t+\tau_n)|^2\right)} \\ \times[\xi'_{j,n}(t,\tau_n) - \xi_{j,n}(t,\tau_n)], \end{aligned} \tag{4.7}$$

where the iteration parameter β_P also assumes values between 0 and 1. To preserve the pure phase-gate property of $P(t)$, an additional constraint is applied by

$$P_{j,n+1}(t) = \exp\{i \arg[P_{j,n+1}(t)]\}. \tag{4.8}$$

The updated XUV and gate function are then inserted in

$$\xi_{j,n+1}(t,\tau_n) = E_{j,n+1}(t)\ P_{j,n+1}(t-\tau_{n+1}) \tag{4.9}$$

to repeat the above procedures at the next delay step τ_{n+1}. When all delay points τ_n have been processed, the global iteration loop will go forward into $j+1$.

The convergence criterion is calculated via the root mean square (RMS) between the original and the reconstructed spectrogram after every global iteration step j as

$$\text{rms} = \sqrt{\frac{1}{MN}\sum_{\omega,\tau}|S_j(\omega,\tau) - S(\omega,\tau)|^2}. \tag{4.10}$$

Here, M is the temporal sampling grid for XUV pulse and streaking field, its interval δt is solely determined by the resolution and total spectral range, and N is the time delay sampling grid with interval $\delta\tau$. $S_j(\omega,\tau)$ is generated in every iteration step. For a good convergence, one needs to optimize the iteration parameters β_P and β_E according to different delay step size and the total number of steps. Another relevant parameter is the time-delay ratio R=FWHM[arg$(P(t))]/\delta\tau$, given by the ratio of the FWHM of the streaking field divided by the time-delay interval $\delta\tau$. It has been shown in [79] that ePIE will give accurate reconstruction for $R > 5$.

4.2.3 The robustness of ePIE

The ePIE scheme differs and has some advantages over other reconstruction schemes such as the above-mentioned PCGPA and LSGPA. The time delay increment does not depend on the desired temporal resolution or the wavelength sampling of the spectrometer, but only on the duration of the gate field $P(t)$. Ptychography requires N spectra recorded at different time

delays τ_n (n=1...N) between the XUV pulse and the streaking field, all spectra combined together form the spectrogram $S(\omega, \tau)$ sampled on an M×N grid. The only constraint on the two integers is $N \leq M$ but generally N is orders of magnitudes smaller than M. Even with a few spectra recorded the algorithm can converge, this has been illustrated in [79, 81]. Due to the small number of spectra needed, i.e. N and M do not have to span the same time window, this decreases the time needed for convergence. The PCGPA algorithm requires a sampling grid of M×M, and typically the spectral axis has a higher sampling rate than the temporal axis, which means the temporal axis needs interpolation and this might lose information that changes faster than the delay increment.

The performance of the algorithm against different noise effects is being studied in [82] for simulated streaking traces of single and double pulses, such as delay jitters between the attosecond and NIR pulse, energy resolution of the photoelectron detector, and Poisson noise in streaking spectrograms with different count levels. The central momentum approximation (CMA) is used both in the generation of the streaking spectrogram and the retrieval algorithm for bandwidth-limited attosecond pulses with 200 as pulse duration. In Fig. 4.6 and 4.7, the three sources of noise are shown individually, as well as their combination, and their impact on the retrieval of isolated and double XUV pulses in the transform-limited regime.

In [82], it was shown that among the three forms of noise studied, Poisson noise (counting statistics) has the most pronounced effect on the pulse duration, resulting in an overestimation on the order of 5%-10% when the count level is below 10×10^3 in the photoelectron spectrum. In the case of a double pulse, the detector resolution is the main limitation in retrieving the side pulse amplitude. Both delay jitter and detector resolution lead to an underestimation of the retrieved parameters, while these parameters are overestimated under the influence of Poissonian counting statistics. Both delay jitter and detector resolution result in an underestimation of the retrieved parameters, while they are overestimated under the influence of Poisson noise. Applying spectro-temporal smoothing to the background-free noisy signals can reduce the impact of noise due to counting statistics, which improves the accuracy of retrieved pulse duration. The retrieval accuracy of experimental signals with nonzero background level was not investigated, because we did not have measured data at that time.

In measurement, it is preferred to obtain a clean trace, meaning a trace with one oscillation like Fig. 4.6. For instance, if there exists a second trace overlapping in energy with π phase shift to the main trace, which might come from the CEP setup mentioned in 3.3.1 not set to an optimal value causing the streak fields carrying different CEP, or a double pulse produced in the HHG process, then the retrieval algorithm cannot distinguish these two.

4.2.4 Retrieval of the time delay zero and electric fields

Studies related to laser-driven quantum dynamical processes, such as NIR-induced couplings between bound states, often lead to one-cycle or sub-cycle oscillations in resonant absorption lines. For an experiment, the typical central wavelength of 750 nm, one laser cycle is 2.5 fs. In the beamline, the resolution provided by the split-and-delay interferometric unit, where the

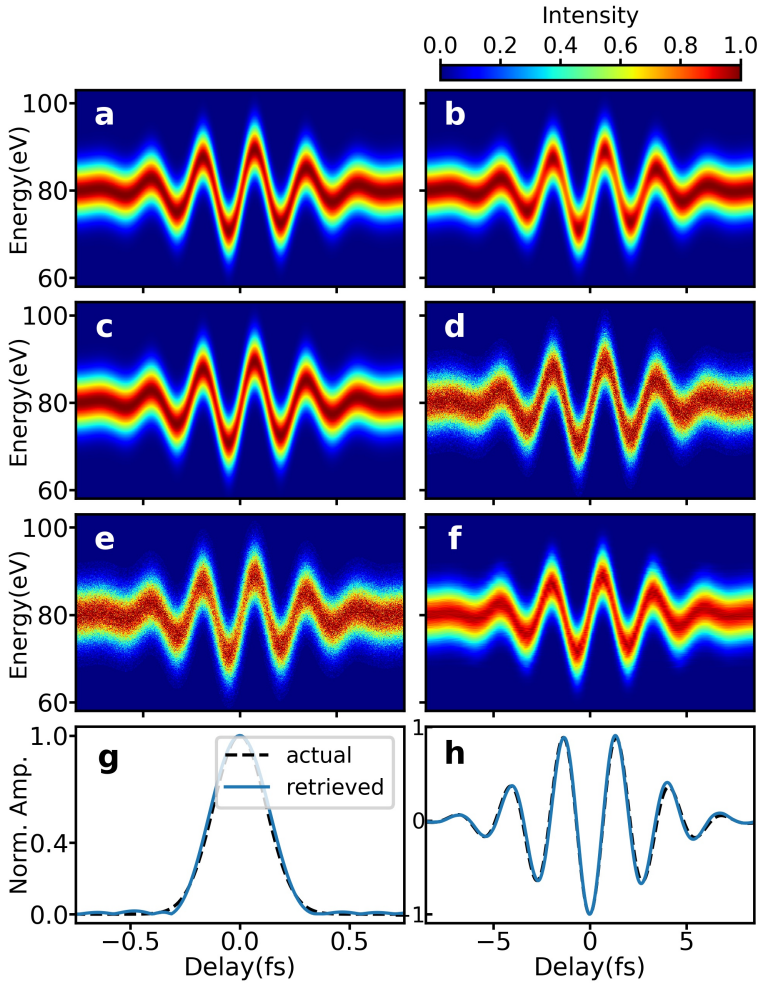

Figure 4.6: (a)–(e) Visualization of noise effects on the streaking trace, (f)–(h) retrieval of an XUV single pulse (FWHM 200 as) from the trace in (e). Large noise parameters are chosen to better visualize the effects. (a) Noise-free SFA input trace (normalized to unity), (b) trace with 0.3 fs delay jitter, (c) trace with 1.5 eV detector resolution, (d) trace with 4.8×10^3 photoelectron counts per delay step and including Poisson noise, (e) trace of all of the above noise operations applied in sequence, (f) retrieved trace, (g) retrieved XUV pulse, (h) streaking gate. The black dashed lines represent the simulated XUV pulse and gate used to calculate the noise-free trace (a). (a)–(f) and (h) share the same horizontal axis. [82]

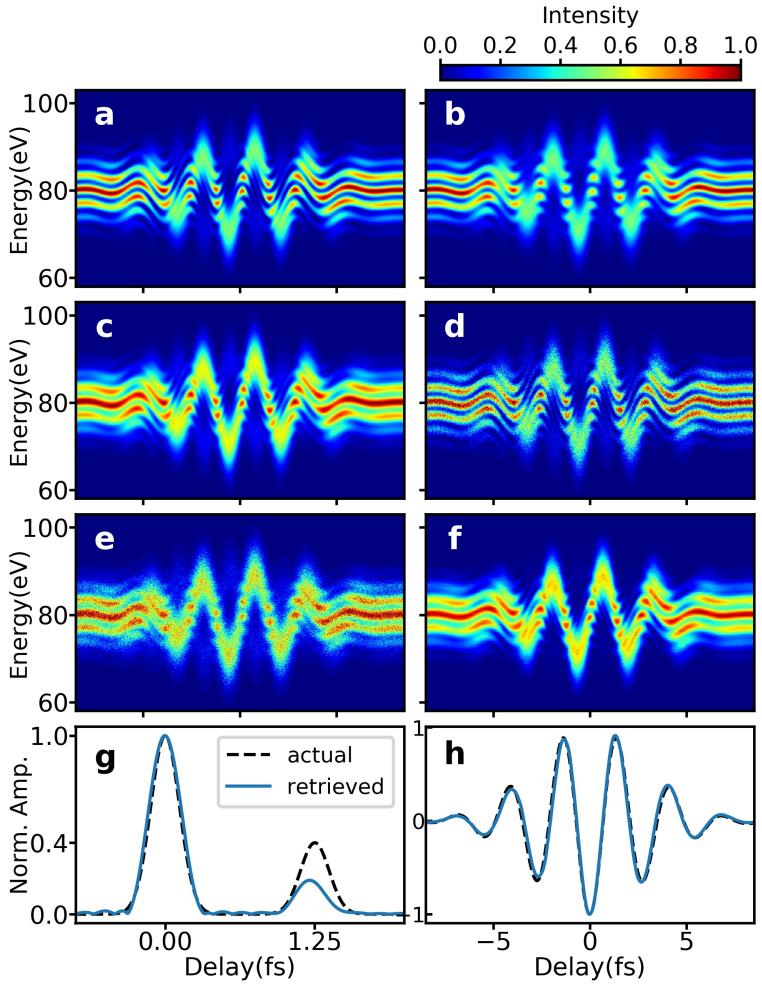

Figure 4.7: (a)–(e) Visualization of noise effects on the streaking trace, (f)–(h) retrieval of an XUV double pulse (FWHM 200 as) from the trace in (e). Large noise parameters are chosen to better visualize the effects. (a) Noise-free SFA input trace (normalized to unity), (b) trace with 0.3 fs delay jitter, (c) trace with 1.5 eV detector resolution, (d) trace with 2.8×10^3 photoelectron counts per delay step and including Poisson noise, (e) trace of all of the above noise operations applied in sequence, (f) retrieved trace, (g) retrieved XUV pulse, (h) streaking gate. The black dashed lines represent the simulated XUV pulse and gate used to calculate the noise-free trace (a). (a)–(f) and (h) share the same horizontal axis. [82]

XUV and NIR co-propagates and are split in time, is calibrated with the translation movement of the piezo stage of the inner mirror, which is 1.705 fs per μm with the relative error below 1% [83].

In our setup, one could roughly find the time overlap between the NIR and XUV pulse by imaging the beam profile around its focus position with a camera, and the split-mirror setup can be used to scan the inner-mirror stage to observe interference patterns. Where the interference fringes show the highest visibility can be interpreted as the position where the maxima of the pulse envelope are in overlap. However, this procedure provides mostly an estimation that is helpful for alignment purposes, and it depends on experimental settings. For instance, metallic filters in the beamline will introduce additional delays because of the dispersion of the material. Or the relative angle between the split-mirror setup, small changes during alignment of the XUV and NIR spatial overlap in the target region will cause changes in the time overlap. Therefore, for precise calibration of the time delay zero or time overlap one would turn to more reliable methods.

Such methods make use of timing-sensitive strong-field-induced effects that modify the absorption lineshape. For instance, the window resonances of the autoionizing states in Argon [84, 85], the atom is strong-field ionized after XUV excitation, and the XUV-induced dipole momentum is cut when there is NIR, then the strength of the absorption lines will be delay-dependent, and it is minimal in time overlap. Also, could be use separate reference measurements to analyze the build-up effects of ion absorption lines [86] or Autler-Townes splitting [83, 87]. Moreover, the strong field-induced ponderomotive shift of the resonance state which modifies the lineshape [37, 88], with further analysis by the dipole control model [83, 89, 90], one can iteratively fit several parameters related to the spectral lineshape with time-delay until reaches convergence.

With the simultaneous experiment presented here, one calibrates the time overlap with the measured streaking trace. In streaking, the absolute value of the time-delay zero can not be directly measured during the experiment, and for ePIE algorithm the time-delay axis is not arbitrarily defined, it will be given by the retrieval itself. Even if the time-delay zero input into ePIE is shifted, as long as the whole streaking trace still lies within the total time window, the algorithm will converge and reconstruct the electric fields $E(t)$ and $P(t)$, only with a shift in the time axis corresponding to a relative shift of the time-delay zero.

The delay axis in fs converted from the x-axis plotted in Fig. 4.5 (b) can be arbitrary, the algorithm will retrieve the electric fields with a corresponding shift on the time axis. Because of our simultaneous measurement, streaking and absorption share the same delay axis, which means the absolute time delay zero obtained from streaking retrieval can be used for absorption. The retrieved XUV pulse duration is 195 ± 11 as, the rms error is obtained from 5 separate runs, when converted to the energy domain it centers around 58 eV. The NIR pulse duration is $\sim$5 fs.

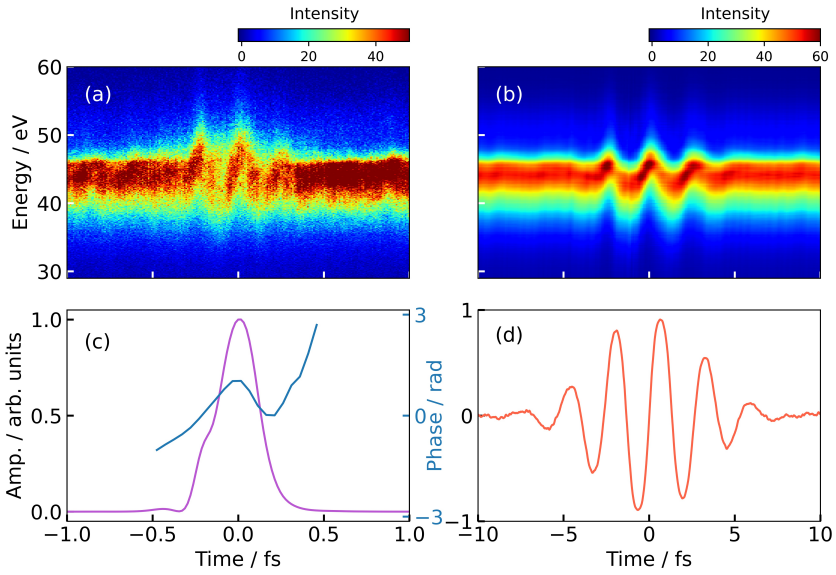

Figure 4.8: Retrieval of the measured streaking trace. (a) Measured. (b) Retrieved trace. After 500 iterations, rms error is 0.082. (c) Retrieved XUV field intensity (purple) and phase (blue). (d) Retrieved NIR gate, which is the vector potential of its electric field.

4.3 Data processing for absorption

4.3.1 Photon energy calibration

The spectra measured by the camera are in pixels, one needs to convert pixels to photon energies by fitting the Fano lineshape of the excited states in helium. In the setup, a flat-field spectrometer grating is used to separate different energies of the harmonic spectrum. One can use the grating equation to map the spectral plane and different wavelengths of the reflected XUV pulse

$$m\lambda = g\left(\sin(\alpha) - \sin(\beta)\right), \tag{4.11}$$

where m is the spectral order of dispersion, α and β are the angle of incidence and reflection, respectively, and g is the effective grating constant. The grating used in this experiment is $g = 1/600$ mm. Considering the geometry of the setup, the relation between wavelength and pixel is

$$\lambda = \frac{g}{m}\left(\sin(\alpha) - \frac{1}{\sqrt{(\frac{x}{L})^2 + 1}}\right), \tag{4.12}$$

where L is the distance between grating and camera, and x is the camera position with respect to the grating surface. This equation is used to fit absorption line positions in measured spectra and generate the pixel to photon energy calibration curve, it is shown in Fig. 4.10.

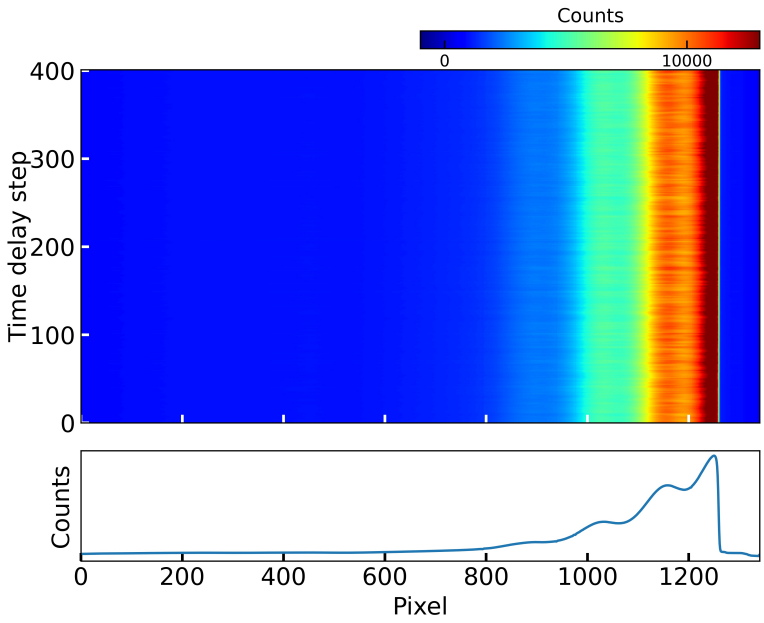

Figure 4.9: The measured absorption spectra and its histogram over the whole delay range. In the lower histogram plot, one can see the oscillation of the harmonic peaks, their peak-to-peak distance is around 3 eV.

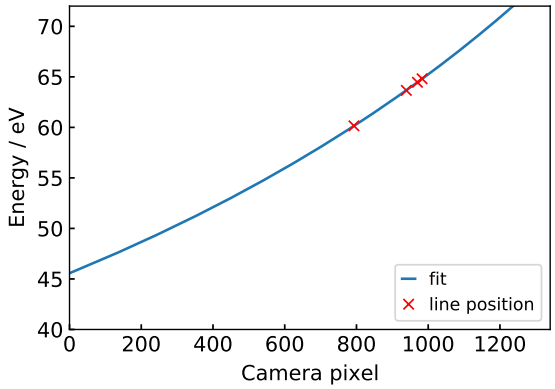

Figure 4.10: Energy calibration curve (blue) obtained by fitting the inverted grating equation to the resonance positions of helium resonances (red).

4.3.2 Reference spectrum

After obtaining an energy-calibrated spectrum, one then calculates the absorbance of the spectra. The recorded spectrum consists of the slow varying high-harmonic spectrum and the sharp absorption lineshapes of helium states. The standard procedure of data analysis in transient absorption is the calculation of the optical density from the measured signal $I_{\mathrm{sig}}(\omega)$ with target gas and a reference signal I_{ref}.

There are two general methods of acquiring I_{ref}:

- Measured reference $I_{\mathrm{ref}}^{\mathrm{m}}$: directly measure the high harmonic spectrum without the target gas
- Fourier filtered reference $I_{\mathrm{ref}}^{\mathrm{f}}$: apply a low-pass Fourier filter to $I_{\mathrm{sig}}(\omega)$ to extract the low frequency spectrum, and then scale it

The first method with $I_{\mathrm{ref}}^{\mathrm{m}}$ is the most straightforward one. The HHG generation is a non-linear process, it is sensitive to small fluctuations in the driving laser, and moving the target cell in and out of the beam path to measure absorption and reference one after another might not be the best solution. Therefore, the *in situ* reference method has been introduced in [52], to measure part of the XUV beam diffracted by a TEM grid that propagates above the target cell interaction region as a reference spectrum. However, the cell is very similar to a usual absorption cell, making it impossible to perform our simultaneous measurement.

Under this condition, it is only possible to obtain the reference from the Fourier filter method. The asymmetric absorption lines are sharp in structure compared to the slow-modulating harmonic background, thus one can reconstruct a *in situ* reference spectrum from each obtained spectrum. By applying a low-pass Fourier filter, the harmonic modulation can be directly retrieved from each measured signal without the shape features (see Fig. 4.11(a)). The low-pass filter is valid because all resonance line shapes exhibit finer spectral structures than the $\sim$3 eV harmonic background.

Following Beer-Lambert's law and Eq. 2.45, the OD it is given by

$$OD(\omega) = -\log_{10}\frac{I_{\mathrm{sig}}(\omega)}{I_{\mathrm{ref}}(\omega)} = \frac{\rho\, l}{\ln 10}\sigma(\omega). \tag{4.13}$$

Here, $\sigma(\omega)$ is the non-resonant photo-absorption cross section, the value can be extracted from the precision measurements of [91]. In the regime of the doubly-excited states of helium, $\sigma(\omega)$ comes from the absorption into the N = 1 continuum, and it only changes slowly as a function of energy. The path-length-density product $\rho\, l$ is the quantity for the optical thickness of the gas target. The helium backing pressure during experiment was tested to avoid significant dispersion effects in too dense materials [92]. Value of the non-resonant photoabsorption cross-section of helium is $\sigma = 0.55$ Mb obtained from [91]. From the spectra, we have $OD \approx 0.024$, thus one can estimate

$$\rho\, l = \frac{0.22\ln(10)}{50\ \mathrm{Mb}} = 1\cdot 10^{17}\ \mathrm{cm}^{-2} = 2.8\ a.u.. \tag{4.14}$$

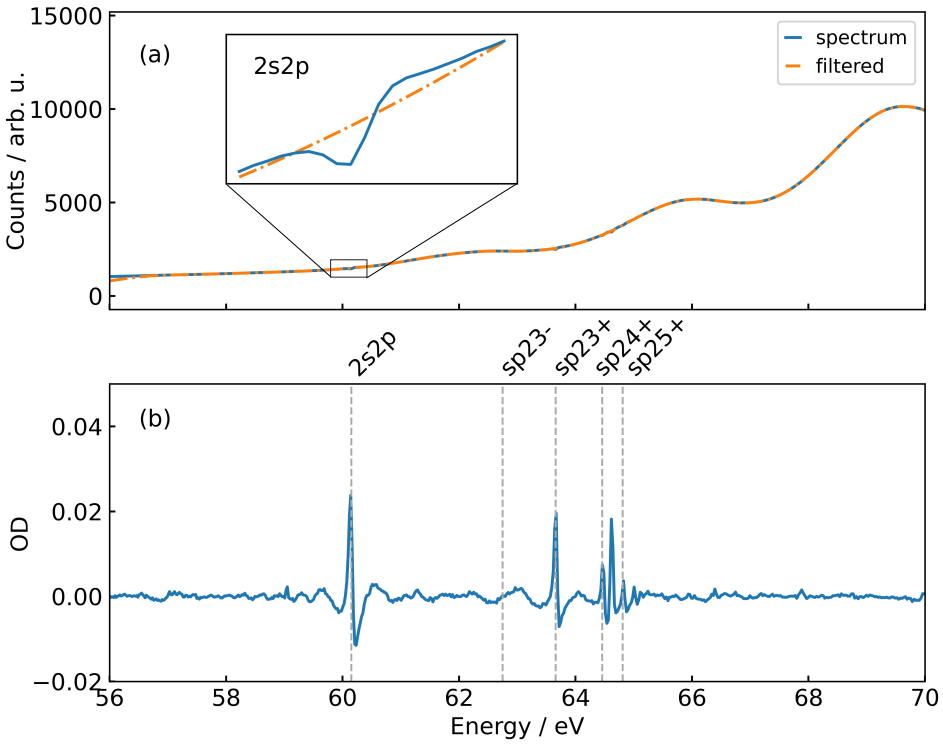

Figure 4.11: Absorption spectrum. (a)Comparison of the harmonic modulation spectrum before and after employing a low-pass Fourier filter (orange dashed line) to the measured absorption spectrum (blue). (b) The OD spectrum. Note the peak between $sp_{2,4+}$ and $sp_{2,5+}$ is from dead pixels on the camera, and it does not show any delay-dependent features.

Then the *in situ* filtered spectrum is scaled to obtain a reconstructed reference spectrum

$$I_{\mathrm{ref}}(\omega) = I^{\mathrm{f}}_{\mathrm{ref}}\, e^{\sigma(\omega)\,\rho\,l}. \tag{4.15}$$

Thus, the filtered spectrum after the low-pass filter is used to calculate OD, plotted in Fig. 4.11.

4.3.3 Inner mirror walk-off calibration

The inner-mirror in the split-mirror setup, which delays the XUV beam, will create a walk-off of the beam, and slightly change the angle of incidence on the spectrometer grating. The incidence angle on the grating is around 85deg, and the inner mirror movement is small, thus the shift of wavelength is approximately linear with the inner-mirror position. This shift will be reflected in the absorption lines and it will be used to calibrate this walk-off effect.

For the correction of the walk-off, one can trace the position of the absorption line where there are no field-induced changes. The $2s2p$ absorption has a more complicated lineshape,

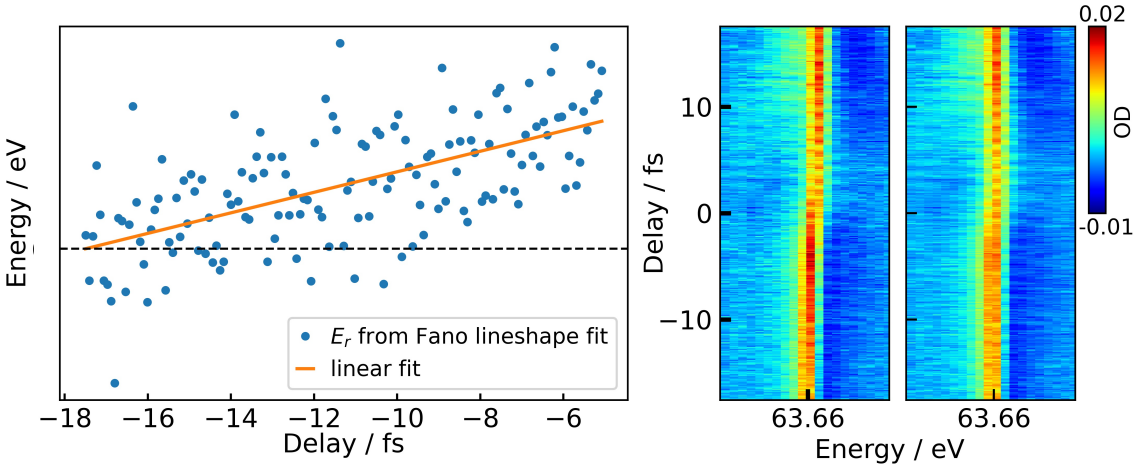

Figure 4.12: Calibration of the walk off of the inner mirror. (a) Position (blue) of the the $sp_{2,3+}$ resonance line where there is no NIR present. Orange line is the linear fit, it is used to shift the spectrum in pixel direction for different time delay. (b) Comparison of the resonance before (left) and after (right) the calibration.

thus the $sp_{2,3+}$ line is used. Because the shift is linear, this linear relationship between pixel and delay obtained from negative delays could be applied to all delay ranges including spectra where the NIR is present. Fig. 4.12 shows the $sp_{2,3+}$ absorption line without and with compensation of the walk-off, one can see the line is no longer tilted over more pixels. The correction of this walk-off effect is important for the Fano lineshape fit in the next chapter.

Chapter 5

Attosecond dynamics of dipole-coupled doubly excited states in helium

5.1 Few-level TDSE simulation

From the absorption measurement, we observe the two strongest absorption lines which correspond to the $2s2p$ and $sp_{2,3+}$ states are strongly modulated as a function of time delay. In order to understand the coherent coupling between these two states, a numerical simulation is performed. All the interaction and coupling information of multi-particle systems are carried by the wave functions. For a system like hydrogen with one bound electron, analytical solutions can be found for the wave functions [93]. However, in the case of a helium atom with two electrons, one needs to numerically approximate the solutions of the time-dependent Schrödinger equation.

Our simulation employs a time-dependent few-level model based on the coupling of a few discrete states where the Schrödinger equation is solved. In the model, the energy levels of interest are represented by the ground state $|g\rangle$, four excited states $|e\rangle = |2s^2\rangle$, $|a\rangle = |2s2p\rangle$, $|b\rangle = |2p^2\rangle$, and $|c\rangle = |sp_{2,3+}\rangle$, and two continua $|1s, \epsilon p\rangle$ and $|1s, \epsilon s\rangle$, into which the $^1P^o$ and $^1S^e$ bound states autoionize, respectively. The states $|2s^2\rangle$ (^{1}S^e) and $|2p^2\rangle$ (^{1}S^e) are included because they are close to the resonant state $2s2p$, and their energy difference is around the central photon energy 1.54 eV of the NIR laser. Other states from the N=2 doubly excited Rydberg series are far off-resonance with respect to the coupling NIR laser or are significantly lower in coupling strength to the states included in this model, and are thus not accounted for. Coupling between states in continua with different symmetry is also neglected for the intensities of our experiment [94]. The parameters used in the simulation of the resonant energy and lifetime of the bound states are listed in Tab. 5.1 below.

Fig. 5.1 plots the energy level diagram of the relevant states and transitions in helium. The system is first excited by an XUV pulse, then they are strongly coupled by a time-delayed NIR pulse. The excited states are excited from the ground state through bound-bound and bound-continuum transitions with dipole matrix elements μ_{nm}, while the excited states are coupled via configuration interactions with matrix elements $V_{\epsilon,n}$.

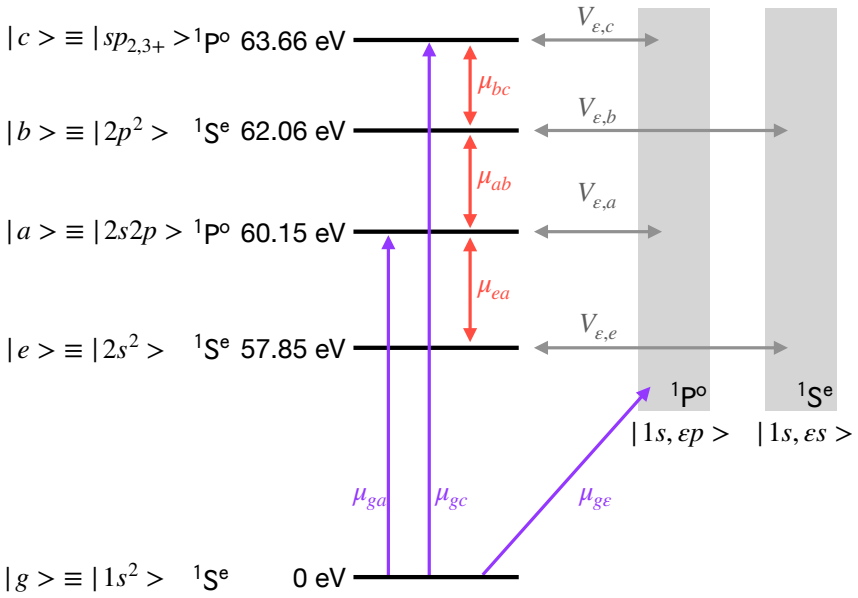

Figure 5.1: Energy level diagram of the simulated system, which shows the coupling of the involved states during the interaction with the laser fields. The XUV- and NIR-induced couplings are marked with purple and red arrows, respectively. The single-photon transition in 1.54 eV (800 nm) is depicted in red.

State	E_0 (eV)	Γ (meV)	q
$2s^2$	57.85	125	
$2s2p$	60.15	37	-2.75
$2p^2$	62.06	6	
$sp_{2,3+}$	63.66	10	-2.53

Table 5.1: Parameters of the bounds states used in simulation, the values are obtained from [33] for $^1P^o$ states and [95, 96] for $^1S^e$ states.

Using the states listed above, and considering that autoionization is the main process involved in the lineshape formation in measured spectra, the state vector of the system is expanded into

$$|\psi(t)\rangle = c_g\,|g\rangle + c_e\,|e\rangle + c_a\,|a\rangle + c_b\,|b\rangle + c_c\,|c\rangle + c_{\varepsilon p}\,|\varepsilon, p\rangle + c_{\varepsilon s}\,|\varepsilon, s\rangle\,. \tag{5.1}$$

Next we numerically solve the Schrödinger equation for the simulation with a spilt step algorithm [97], described in the following. The time evolution is given by the solution of the Schrödinger equation in matrix representation

$$i\partial_t \vec{c}(t) = \hat{H}\vec{c}(t), \tag{5.2}$$

with the complex expansion coefficient $\vec{c}(t) = (c_g, c_e, c_a, c_b, c_c, c_{\varepsilon p}, c_{\varepsilon s})^T$. Given the initial wave function $|\psi(t=0)\rangle = |\psi_0\rangle$, the formal solution of the Schrödinger equation is

$$|\psi(t)\rangle = e^{-i\frac{\hat{H}}{\hbar}t}\,|\psi_0\rangle\,. \tag{5.3}$$

In linear algebra, we know that for a diagonal operator the matrix exponential reduces to a diagonal matrix of the exponential of the matrix elements. Therefore, in the field-free case, the Hamiltonian reduces to a trivial phase evolution of each eigenstate depending to its energy. We can apply the same method to the full Hamiltonian, by transforming the state vector into the eigenstate of the Hamiltonian.

As a start, we perform the propagation in discrete time steps Δt to determine the complete evolution of the coefficients, with the total propagation time $t_k = k\delta t$, the following sequence is performed in every k step:

1. The field-free evolution
$$c_i(t+\Delta t) = e^{-i\frac{E_i}{\hbar}\Delta t}c_i(t)$$

2. Transformation into the eigenstates of the interaction. The transformation matrix $\hat{T}$ consist of the basis eigenvectors of $\tilde{V}$ as columns.
$$\tilde{V} = \mathrm{diag}(\tilde{V}_1 ... \tilde{V}_n) = T^\dagger \hat{V} T, \quad |\tilde{\psi}\rangle = T^\dagger\,|\psi\rangle$$

3. Propagation in the interaction basis.
$$\tilde{c}_i(t+\Delta t) = e^{-i\frac{\tilde{V}_i}{\hbar}\Delta t}\tilde{c}_i(t)$$

4. Back transformation into the energy basis.

$$|\psi\rangle = T|\tilde{\psi}\rangle$$

The XUV pulse used in our experiments is weak so it can be treated as a small perturbation to the field-free Hamiltonian, thus the $\hat{V}$ only includes the dressing of the NIR pulses. Atomic units are used throughout the calculations in the simulation.

For each step, the time-dependent dipole moment between the ground state, the dipole-allowed states $|a/c\rangle$, and the $|1s, \varepsilon p\rangle$ is evaluated:

$$d(t) = \langle\psi|\,\hat{d}\,|\psi\rangle = \mu_{ga}\; c_a(t) + \mu_{gc}\; c_c(t) + \mu_g \sum_{\varepsilon} c_{\varepsilon p}(t), \tag{5.4}$$

where the ground-continuum dipole matrix element $\mu_g = \mu_{g\varepsilon}$ is assumed to be energy independent. The sum runs over all excited states.

The full time-dependent Hamiltonian of the system in dipole approximation is $\hat{H}(t) = H_0 + H_{NIR} + H_{XUV} + H_{ci}$, written out in details as

$$\hat{H}(t) = \begin{bmatrix} E_g & 0 & \mu_{ga}^*\cdot F_{XUV} & 0 & \mu_{gc}\cdot F_{XUV} & \mu_{g\epsilon}\cdot F_{XUV} & 0 \\ 0 & E_e & \mu_{ea}\cdot F_{NIR} & 0 & 0 & 0 & 0 \\ \mu_{ga}^*\cdot F_{XUV} & \mu_{ea}^*\cdot F_{NIR} & E_a & \mu_{ab}\cdot F_{NIR} & 0 & V_{\epsilon,a} & 0 \\ 0 & 0 & \mu_{ab}^*\cdot F_{NIR} & E_b & \mu_{bc}\cdot F_{NIR} & 0 & V_{\epsilon,b} \\ \mu_{gc}^*\cdot F_{XUV} & 0 & 0 & \mu_{bc}^*\cdot F_{NIR} & E_c & V_{\epsilon,c} & 0 \\ \mu_{g\epsilon}^*\cdot F_{XUV} & 0 & V_{\epsilon,a}^* & 0 & V_{\epsilon,c}^* & E_\epsilon - i\kappa & 0 \\ 0 & 0 & 0 & V_{\epsilon,b}^* & 0 & 0 & E_\epsilon - i\kappa \end{bmatrix} \tag{5.5}$$

The electric fields F_{XUV} and F_{NIR} are both time-dependent. The diagonal elements of the Hamiltonian are the energies of the respective states, where the energy of the continuum states gives a complex contribution in the form of the linewidth Γ_c. Through this linewidth, the continuum state is adjusted to decay rapidly such that it effectively acts as a loss channel. The configuration interaction matrix elements $V_{\epsilon,n} = \langle 1s, \epsilon p/s|\,\hat{H}\,|n\rangle = V_n$, which describe autoionization are taken to be constant in the vicinity of each configuration state.

The free parameters of the simulation are:

- total time axis T and time step size Δt
- continuum distribution and its delay constant κ
- configuration interaction matrix elements V_n
- dipole matrix elements coupling the ground state to the excited states d_{gn} and continuum states $d_{g\varepsilon} = d_g$

- dipole matrix elements d_{ea}, d_{ab} and d_{bc} for the allowed optical transitions between the excited states coupled by the NIR pulse.

Before performing the simulation, some values can be determined directly from the measured absorption lineshape with the help of Fano lineshape fits.

5.2 Fano fit formula

The laser-induced phase change of the states after excitation can be extracted by performing a Fano lineshape fit on the measured absorption spectrum. The Fano phase formula used is from [98], which maps the Fano asymmetry parameter q to a phase φ_{Fano} of the time-dependent dipole response function

$$\varphi_{Fano} = 2\arg(q - i). \tag{5.6}$$

The equation representation of the asymmetric Fano line profile is

$$S_{Fano} = \frac{A_{Fano}}{q^2+1}\left[\frac{(q+\varepsilon)^2}{1+\varepsilon^2} - 1\right] + b, \tag{5.7}$$

where $\varepsilon = 2(E - E_{res})/\Gamma$ is the reduced energy. The formula is valid for a δ-like excitation, that is to say the duration of the excitation is much smaller than the lifetime of the states, which is valid for our case. In fitting experimentally recorded line shapes, the finite spectrometer resolution σ_{res} is taken into account

$$S_{Fano,exp} = -\log_{10}\left[(10^{-S_{Fano}}) \otimes \frac{1}{\sqrt{2\pi}\sigma_{res}}\exp\left[-\frac{E^2}{2\sigma_{res}^2}\right]\right], \tag{5.8}$$

where $\otimes$ denotes convolution.

Here, the free parameters are Fano phase φ_{Fano}, energy of the resonance state E_{res}, decay width Γ, amplitude A_{Fano}, offset b, and sigma energy resolution σ_{res}. Both E_0 and Γ were kept around the literature values for all NIR laser intensities, by setting the boundary of the fit to ± 0.005 eV and ± 0.01 eV respectively. Also, the σ_{res} is set to experimentally determined detector resolution value 0.02 eV. By fitting the absorption line with XUV excitation only (see Fig. 5.2), one finds the energy resolution of the detector which is an input parameter for simulation, it is in agreement with previous measurements preformed with the same setup [52, 99].

5.3 Simulated results

The few-level simulation algorithm is applied on a time grid to scan the time delay between the XUV and NIR pulse. The electric fields (Fig. 5.3 (a)) and time-delay axis are taken from streaking retrieval, also the fields and time axis are interpolated with the B-spline function

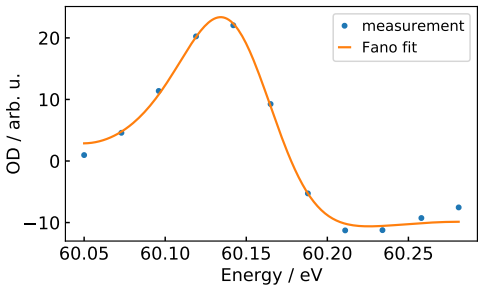

Figure 5.2: Fano fit of the lineshape for resonance $2s2p$, integrated over negative delay range from -17 to -7 fs in order to find the energy resolution of the measurement. From the fit result σ_{res}=20 meV.

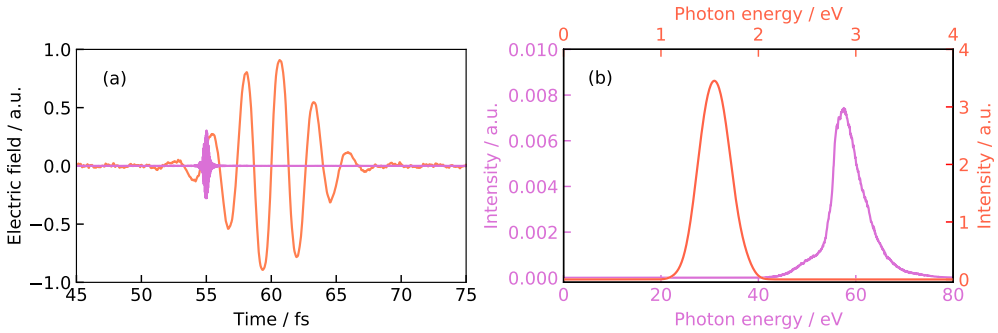

Figure 5.3: The XUV (purple) and NIR (red) fields retrieved from streaking that are used in simulation. They have different scale on y-axis for better visibility. (a) Electric fields in the time domain, their position on the time axis is set to time delay 5 fs. (b) The intensity spectra of both pulses from the Fourier transform of fields in the time domain. The XUV pulse is centered around 60 eV and the central photon energy of the NIR is 1.54 eV.

to have a finer step size. According to the Fourier transform relation, the total length of the time grid determines the energy resolution of the simulated spectra, and the time step size determines the grid of the energy axis.

In the simulation, the total time grid length is $T = 32000$ a.u. (774 fs) with time step size $\Delta t = 0.25$ a.u. (0.006 fs). They are chosen to have a small enough sample size compared to the 2.5 fs laser cycle and to cover the full natural autoionizing decay time of the states, for instance, the $\Gamma_{2p^2} = 6$ meV corresponding to an exponential decay time of 220 fs. The photon energy resolution is ΔE =0.005 eV, and the total energy axis length is 680 eV.

The continua are modeled by two broadband continuous spectra, which are centered at the resonant energy of $2s2p$ and $sp_{2,3+}$, to couple with $^1P^o$ and $^1S^e$ states, with the decay rate κ =0.8 a.u. corresponding to lifetime 21 eV. Compared to simulations that define hundreds of discrete quasi-continuum states [99, 100] and broaden them to a mutual overlap to approximate

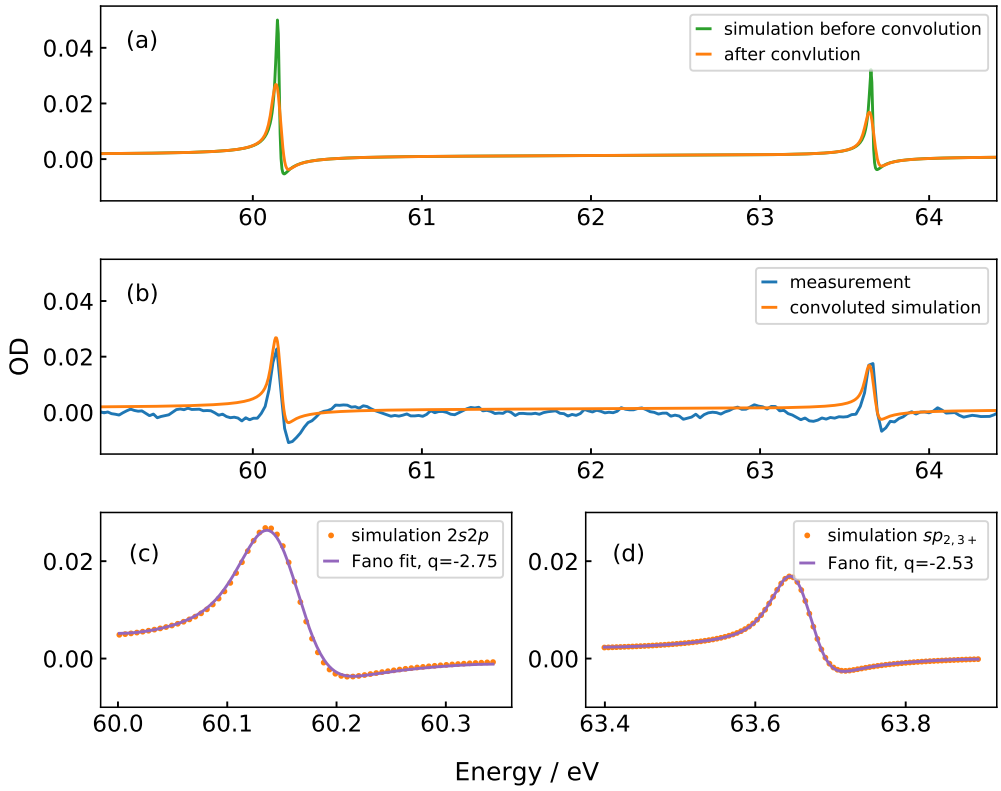

Figure 5.4: Spectrum with XUV excitation only. (a) The spectra before and after convolution with the spectrometer resolution. (b) Comparison between the measurement and simulation, the simulated spectrum is rescaled in amplitude to roughly match the maxima of the $2s2p$ and $sp_{2,3+}$ Fano lineshape. (c) and (d) show Fano lineshape fits, where the value of the Fano q parameter is extracted.

a continuous spectrum, the present method significantly relaxed the computational cost.

The dipole matrix elements μ_{gn} and μ_d configuration interaction matrix elements V_n are chosen for the simulated absorption lines to match known experimental and theoretical parameters (see Table. 5.1). As shown in Figs. 5.4(c) and 5.4(d), the extracted q parameters are -2.75 and -2.53. The absolute values of dipole matrix elements between excited states are $\mu_{ea} = 2.17$ a.u. from [101], $\mu_{ab} = 2.17$ a.u. and $\mu_{bc} = 0.81$ a.u from [102, 103].

With parameters set, one performs the simulation over the delay range -5 to 15 fs, shown in 5.5, then the simulated spectra are convolved with the spectrometer resolution 20 meV extracted from the Fano lineshape fit, from Fig. 5.4 (a) one can see the sharp resonant absorption peaks become less prominent. Near the time overlap and at positive delays, the absorption spectrum is strongly modified. At slightly positive delays, the effect of Autler–Townes splitting of the $2s2p$ resonance with the energetically repelling $2p^2$ dressed state can be seen, it is

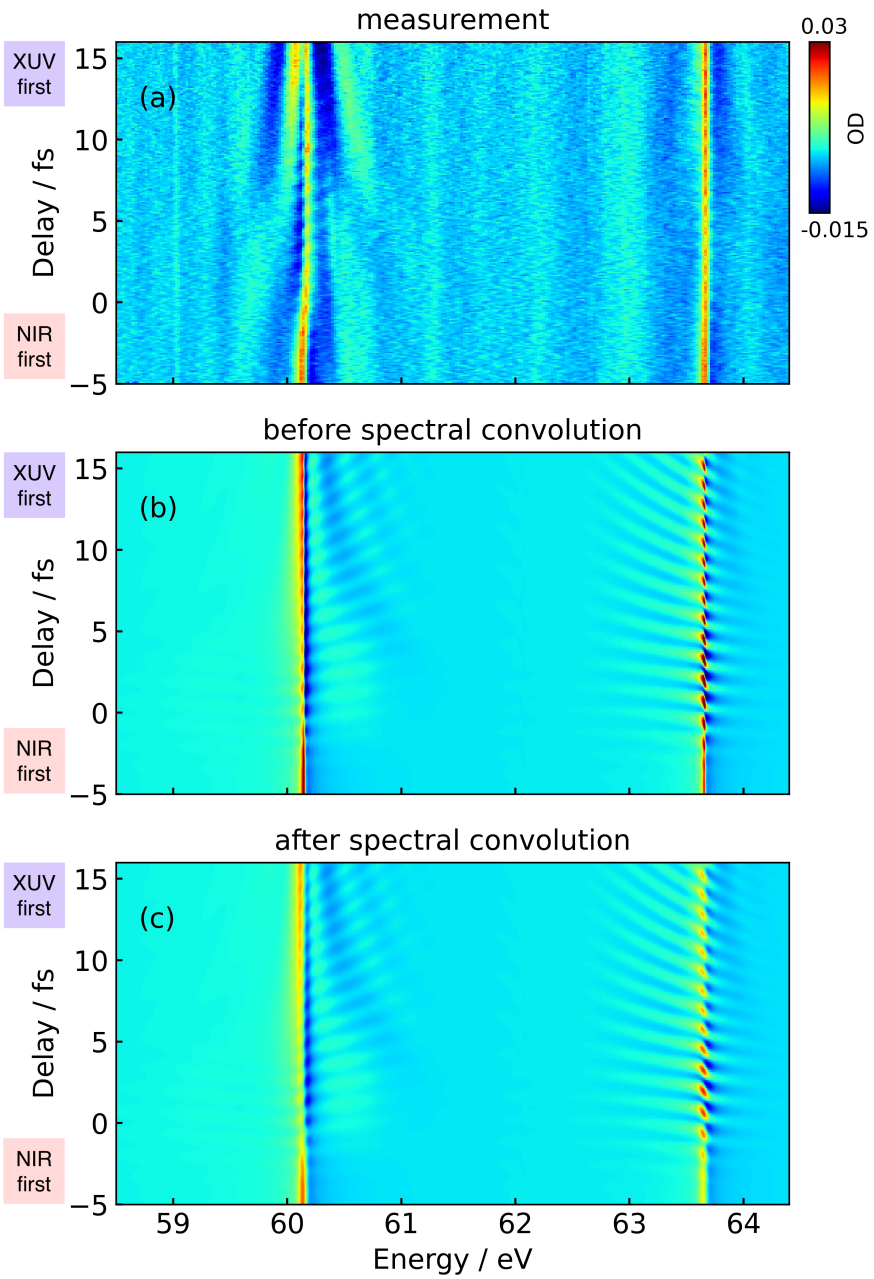

Figure 5.5: Measured and simulated spectrum of the helium doubly excited states as a function of time delay. The numerically calculated absorption spectra (b) is rescaled in order to share the same colorbar with measured spectrum (a), and it is spectrally convolved with a Gaussian of width 0.02 eV that represents the detector resolution.

Transition	Ott[103]	Stooß[106]	Ho[109]	Chu[101]	Loh[102]	Tarana[107]
$2s^2$ - $2s2p$	-	-1.56	1.58	2.17	-	-
$2s2p$ - $2p^2$	-	2.11	1.99	-	2.17	2.11
$2p^2$ - $sp_{2,3+}$	-0.81	-0.81	0.68	-	-	-

Table 5.2: The dipole matrix elements (a.u.) between three different transitions from theoretical calculations.

evidence of the strong coupling between the autoionizing states and Rabi oscillations.

5.4 Sign convention of the dipole matrix elements

From the time delay calibrated simulated absorption spectrum, one can extract delay-dependent physical quantities such as the transition dipole matrix elements, which play an important role in extracting attosecond state-specific dynamics from transient absorption spectra [104, 105]. Precise determination of the dipole matrix elements between doubly excited states in helium is of interest in many related experiments [103, 106, 107]. In these publications, dipole matrix elements for various S-P and P-D transitions were reported, and in [108] there is a nice summary. To calculate the dipole matrix elements for the helium atom, one needs to solve the Schrödinger equation, the first step is the precise determination of the energies and eigenfunctions of the initial and final states. The dipole matrix elements can be calculated with the expression from [109, 110]

$$F_{DME} = \sqrt{\frac{8\pi}{2l+1}} \langle \Psi_0 | \sum_{i=1}^{2} r_i^l Y_{lm}(r_i) | \Psi_n \rangle . \tag{5.9}$$

In the references, sometimes they have comparable absolute values but with opposite signs, selected transition are listed in Tab. 5.4. The values listed here are found from theoretical calculations with different methods, for instance Stooß [106] and Tarana [107] uses *ab-initio*, Loh [102] uses eigenchannel R-matrix [110, 111], Ho [109] uses stabilization method.

The relative signs of dipole matrix elements have thus far not been tested experimentally, whereas it becomes possible with our experiment scheme. The signs of the dipole matrix elements seemed to appear differently depending on different calculation methods, which can be easily changed in our few-level simulation to compare their influence on absorption spectra. To study the effect of the sign convention of the dipole matrix elements, simulations with the combination of positive and negative signs for μ_{ab} and μ_{bc} are performed, and it was observed that only different relative signs result in different absorption spectrum. The most intuitive comparison is to take delay-dependent lineouts and observe the oscillations. One directly sees different relative signs between μ_{ab} and μ_{bc} will lead to a π phase shift in the oscillations (cf. the orange and gray lines in Fig. 5.7). Thus, it is sufficient to classify the sign conventions into $\mu_{ab}\mu_{bc} > 0$ and $\mu_{ab}\mu_{bc} < 0$ and further compare with the experiment.

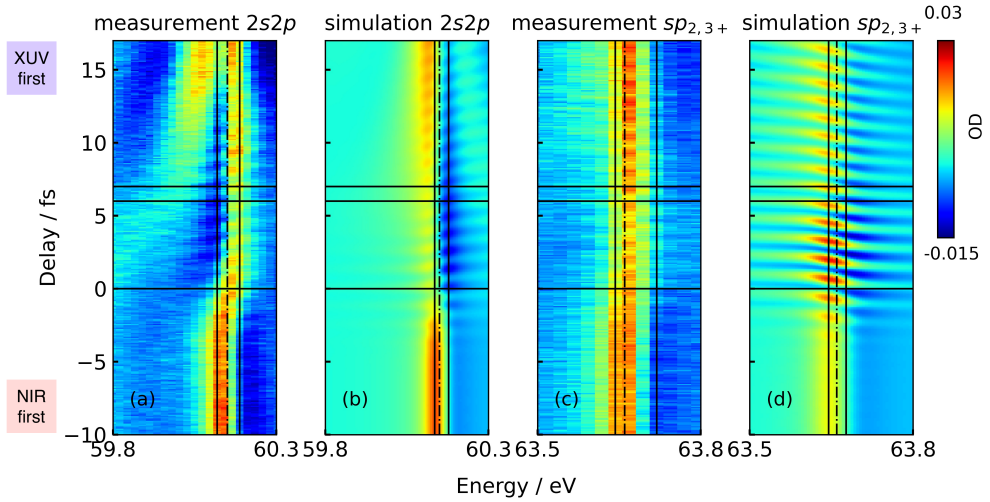

Figure 5.6: Absorption spectrum from simulation and measurement zoomed in on the two resonant states. Horizontal lines plot the delay 0, 6, and 7 fs. Vertical dashed lines mark the resonance energy of $2s2p$ 60.15 eV and $sp_{2,3+}$ 63.66 eV, solid lines indicate the region where the delay-dependent lineouts are extracted from. The energy between the two vertical solid lines are: (a) 0.045 eV, (b) 0.043 eV, (c) 0.045 eV, and (d) 0.032 eV.

In previous absorption analysis, one could define the delay zero precisely in simulation by shifting the oscillation lineout obtained from the experiment along the time delay axis. With our simultaneous measurements, we are able to obtain a time-delay zero calibrated absorption measurement and simulation. With the Fano phase introduced in 5.2, one knows the modified asymmetric lineshape introduces a phase change, therefore when taking the lineout, one needs to select a very small region so that the oscillation will not be smeared out too much by the delay-dependent phase change.

The here observed oscillation is from the beating of a wave packet, which is a direct consequence of the coherent superposition of quantum states, between at least two energetic states, the time evolution oscillates with a cycling period of $T_c = 2\pi\hbar/\Delta E$, determined by the energy spacing of the involved states [99]. The time between two oscillation maxima observed in Fig. 5.7 is 1.2 fs, corresponding to the energy level difference $\Delta E = 63.66 - 60.15 \approx 3.51$ eV between the two mostly dominantly populated states $2s2p$ and $sp_{2,3+}$.

The comparison of the delay-dependent lineout of measurement and simulation shown in Fig. 5.7, one directly sees different relative signs between μ_{ab} and μ_{bc} lead a π phase shift in the oscillations, and only $\mu_{ab}\mu_{bc} < 0$ agrees with experimentally measured data.

From state $2s^2$ to $2s2p$ is a one-photon transition, while $2s2p$ and $sp_{2,3+}$ are coupled through the dark state $2p^2$. However, from references in Tab. 5.4, one sees μ_{ab} and μ_{bc} sometimes are calculated separately and are not consistent in sign. Although for transition $2s2p$ to $2p^2$ all

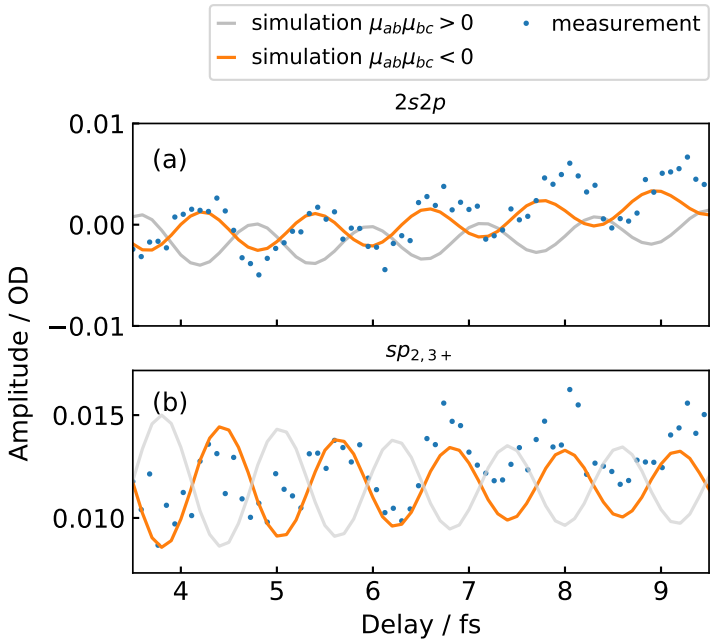

Figure 5.7: Delay-dependent lineouts of the (a) $2s2p$ and (b) $sp_{2,3+}$ resonant states from simulated and measured absorption spectrum. The grey and orange lines are with different relative signs between dipole matrix elements μ_{ab} and μ_{bc}.

calculated values are positive, with our observations, we find μ_{ab} can be both signs as long as $\mu_{ab}\mu_{bc} < 0$. We also simulated with positive and negative dipole matrix elements for $2s^2$ to $2s2p$, and found that it does not change the lineout oscillation phase. As $2s^2$ is the lowest doubly excited state in helium above the N=1 continuum threshold, there is no other state below this energy level to form a coupling scheme similar to $2s2p$ and $sp_{2,3+}$.

The lineouts are compared in the region of 3 to 10 fs, because in the time overlap, absorption spectra are modulated by NIR-induced ponderomotive shift of the state's energy, it is prominent in 5.6 (a) that the $2s2p$ line is shifted to larger energies, and after 10 fs, the spectral structures are more complex with an additional branch to the left of the main resonance. The few-level model simulation used here does not include ponderomotive shift or other couplings to states that are not included, and this leads to different structures in the OD plots. Nevertheless, it simulates the most important two-electron wavepacket oscillation which is the main goal of this analysis.

As mentioned in the previous context, due to symmetry properties of the Fano lineshape there is a π phase shift over the resonance, the delay-dependent lineouts are sensitive to the region which is being selected manually, thus may lead to artificial shifts in the phase of the lineout. Therefore, to further analyze the precision of our time-delay calibration and extract more information on delay-dependent phases from absorption lineshapes directly, one can apply the Fano phase method from [112], described in the next sections.

5.5 Fano lineshape fit

This Fano phase method requires the delay-dependent Fano phase and amplitude values of the near-resonantly coupled doubly-excited states, which can be extracted by fitting the lineshapes with Eq. 5.7. After the discussion of dipole matrix elements in the last section, we used $\mu_{ea} = -2.17$, $\mu_{ab} = 2.17$ and $\mu_{bc} = -0.81$ to produce simulated absorption spectra.

For high NIR intensities, it has been found that additional effects, such as AC Stark shift, will change the lineshape and resonant energy positions [113] or broadening of the linewidth due to ponderomotive potential [114]. One sees in Fig. 5.8, on the resonance $2s2p$ starting at temporal overlap, the whole lineshape is shifted to higher energy in measured data, while this is not captured with our simulation. There is no such energy shift in the other excited state. The fit is applied to a small energy region of the two resonant states for delay from -5 to 15 fs, plotted in Fig. 5.8. One can see in subplot Fig. 5.8 (b) and (d), the Fano fit is only applied to the energy range of 60.1-60.25 eV because if more data points are included on the lower energy side, the fit does not give optimal results.

Fig. 5.9 visualizes the quality of Fano fit, it shows the data points between delay 6 to 7 fs from simulation and their Fano fitted lineshape, the fitted Fano phase and amplitude information in this delay region will be used to extract the delay-dependent relative phases.

5.6 Dipole phase and amplitude

From the Fano fit, one can further use the phase φ_{Fano} and amplitude A_{Fano} information obtained from the previous step and insert into the Fano phase method described in [112], which maps the Fano asymmetry parameter q to a phase φ of the time-dependent dipole response function.

Kaldun's paper assumed the general case of three states $|1\rangle$, $|2\rangle$, and $|3\rangle$, with energy spacing $\Delta\omega_L \approx \Delta\omega_{12} \approx \Delta\omega_{23}$, he then derived the contributions to the quantum state coefficient of $|3\rangle$

$$a_{\text{mod}} = a_1 + a_{\text{self}} + a_{\text{inter}}(\tau), \tag{5.10}$$

where a_{mod} is connected to the lineshape of state $|3\rangle$ which is modulated by the couplings with other states, a_{self} is the two-photon laser coupling of state $|1\rangle$ to $|2\rangle$ and back to $|1\rangle$, and $a_{\text{inter}}(\tau)$ is the coupling pathway of state $|1\rangle$ to $|2\rangle$ and to $|3\rangle$. This assumption for the couplings between the excited states can be applied to our system, therefore in the following, the names of the terms in the Fano phase method will be adapted and explained in detail.

Here, the system of interest consists of one ground state $|g\rangle$, three excited states $|a\rangle = |2s2p\rangle$, $|b\rangle = |2p^2\rangle$, and $|c\rangle = |sp_{2,3+}\rangle$. The energy spacing between states $|a\rangle$ and $|c\rangle$ is 3.51 eV, approximately equal to $2\omega_L$ of the laser. According to dipole selection rules, the transition from the ground state directly to state $|2p^2\rangle$ is not allowed. Thus, $|2p^2\rangle$ is coupled by the NIR pulse through states $|2s2p\rangle$ and $|sp_{2,3+}\rangle$.

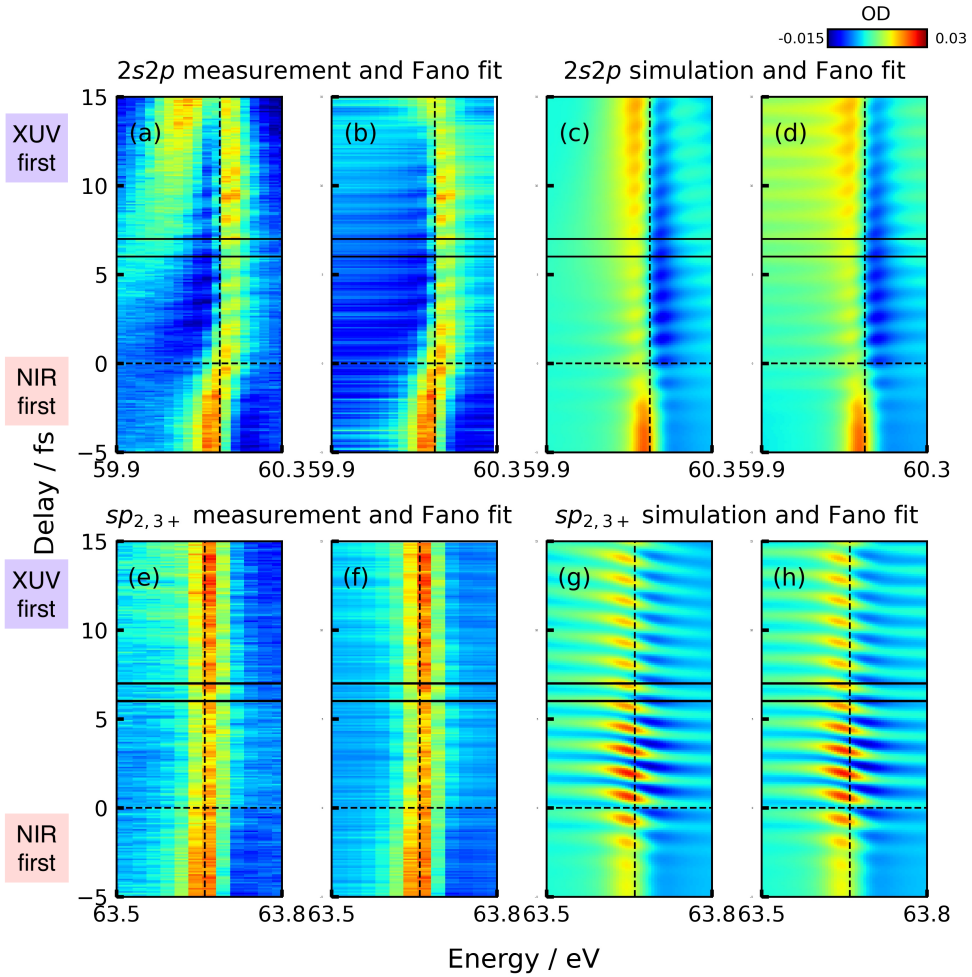

Figure 5.8: (a), (e) Measured and (c), (g) simulated absorption spectra for varying time delay, and next to them on the right are their Fano fit of each individual delay. All subplots share the same colorbar. The horizontal dashed line marks delay zero, solid line marks delay 6 fs and 7 fs. The vertical dashed line are the resonance energy 60.15 eV and 63.66 eV. Note that for subplots (b) and (d), the Fano fit is only applied to energy range 60.1-60.25 eV, for (f) and (h) it is applied to 63.55-63.8 eV.

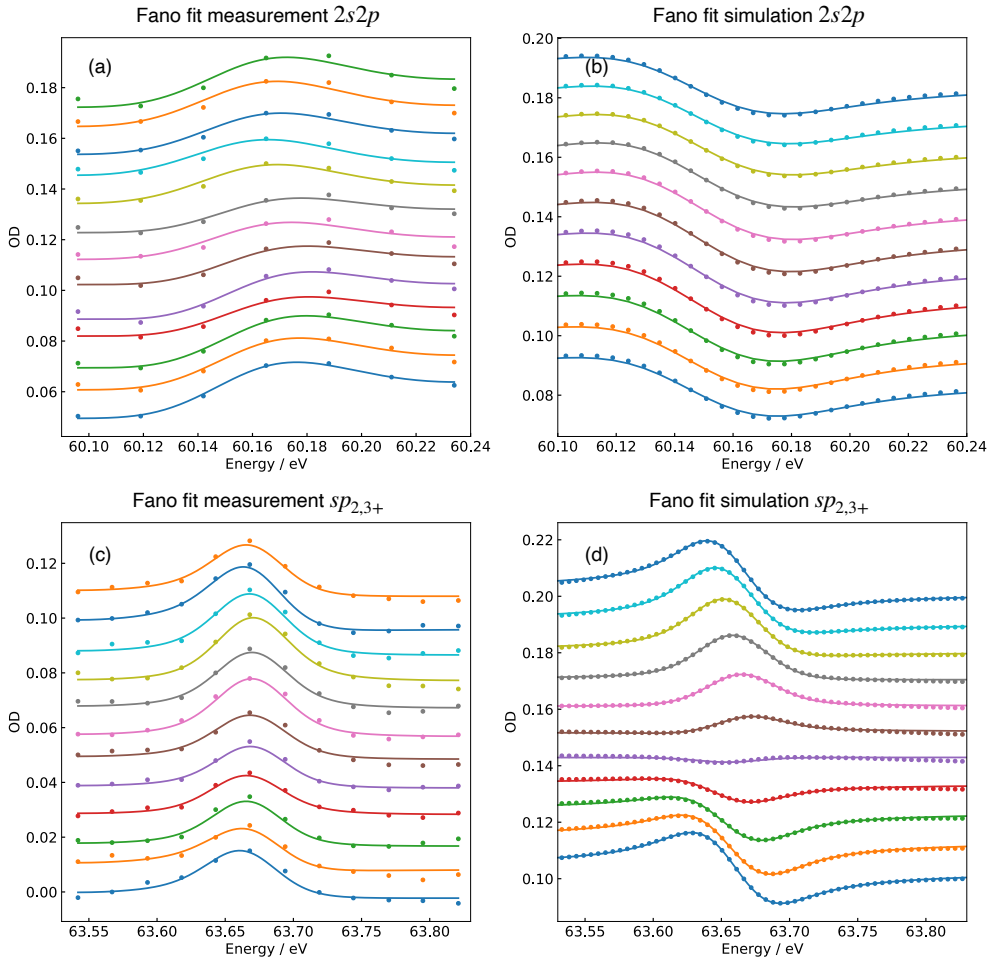

Figure 5.9: Absorption spectrum (dot) and its Fano fit (line) near the helium $2s2p$ and $sp_{2,3+}$ states. Every spectra is plotted with an offset in the y-axis for better visualization. The resonant lineshape changes with time delay τ from 6 to 7 fs of the NIR following the XUV excitation. The fit is performed in the energy region 60.1-60.25 eV for $2s2p$ and 63.55-63.85 eV for $sp_{2,3+}$.

The Fano phase method in a nut shell, starts with a system at time $t = 0$, population from the ground state $|g\rangle$ is excited by the XUV pulse to an excited $|a\rangle$, the wave function at this time is expressed by

$$\Psi(t=0) \propto a_g\,|g\rangle - i a_{ga}\,|a\rangle\,. \tag{5.11}$$

Here, the coefficient $a_g \approx 1$ for all times of a weak excitation, which is the case in our experiment. Then the NIR resonantly couples $|a\rangle$ to $|c\rangle$ by a two photon transition via $|b\rangle$, the expansion coefficient will become

$$\begin{aligned} a^a_{\text{mod}}(\tau) &= A^a_{\text{mod}}(\tau)\, e^{i\varphi^a_{\text{mod}}(\tau)} \\ &= a_{ga} + a_{ab} + a_{ca}(\tau). \end{aligned} \tag{5.12}$$

The different interaction pathways that contributes to state $|a\rangle$ are:

$$\begin{aligned} &a_{ga} : |g\rangle \rightarrow |a\rangle \\ &a_{ab} : |g\rangle \rightarrow |a\rangle \rightarrow |b\rangle \rightarrow |a\rangle \\ &a_{ca} : |g\rangle \rightarrow |c\rangle \rightarrow |b\rangle \rightarrow |a\rangle \end{aligned} \tag{5.13}$$

The first term is

$$\begin{aligned} a_{ga} &= A_{ga}\, e^{i\varphi_{ga}} \\ &\propto -a_g\, E^2_{NIR}\, |\mu_{ga}|^2 \end{aligned} \tag{5.14}$$

The second term describes the laser coupling between the states $|a\rangle$ and $|b\rangle$

$$\begin{aligned} a_{ab} &= A_{ab}\, e^{i(\varphi_{ab}+\pi)} \\ &\propto -a_{ga}\, E^2_{NIR}\, |\mu_{ab}|^2. \end{aligned} \tag{5.15}$$

Population is transferred to state $|b\rangle$ and back to $|a\rangle$ with a small loss of population during this process, which leads to the π phase term. The third term is written out as:

$$\begin{aligned} a_{ca}(\tau) &= A_{ca}\, e^{i(\varphi_{ca}+\pi+\Delta\omega_{ca}\tau)} \\ &\propto -a_{gc}\, E^2_{NIR}\, \mu_{ab}\, \mu_{bc}\, e^{i\Delta\omega_{ca}\tau}, \end{aligned} \tag{5.16}$$

where I_{NIR} is the laser intensity, μ_{ab} and μ_{bc} are the dipole matrix elements. And $\Delta\omega_{ca}$ is the relative phase between $|a\rangle$ and $|c\rangle$, because they are excited by the same XUV but due to NIR coupling, they will evolve differently in time.

The dipole response of $|a\rangle$ after interaction is given by

$$\begin{aligned} \tilde{d}_a(t) &= \langle\Psi(t)|\, r\, |\Psi(t)\rangle \\ &\propto A^a_{\text{mod}}\, e^{i(\varphi^a_{\text{mod}} - \Delta\omega_{gc} t) e^{-\frac{\Gamma}{2}t}} + c.c. \end{aligned} \tag{5.17}$$

with the decay rate $\Gamma = 1/\tau_{life}$. The Fourier transform of $d_c(t)$ is proportional to the absorption cross-section:

$$\begin{aligned} \sigma_{Fano}(\omega) &\propto \mathscr{F}[d_a(\omega)] \\ &\propto \mathscr{F}\left[A^a_{\text{mod}} e^{i\varphi^a_{\text{mod}}} \frac{i - \epsilon(\omega)}{1 + \epsilon^2(\omega)}\right], \end{aligned} \tag{5.18}$$

where $\epsilon = 2(\omega - \Delta\omega_a)/\Gamma$ is the reduced energy. Because of the linearity of the Fourier transformation, $a^c_{\text{mod}}(\tau)$ contributions in the complex factor which is related to the lineshape of absorption spectrum, it is written out as

$$\begin{aligned} A^a_{\text{mod}}(\tau)e^{i\varphi^a_{\text{mod}}(\tau)} &= A_{ga}e^{i\varphi_{ga}} + A_{ab}e^{i(\varphi_{ab}+\pi)} \\ &\quad + A_{ca}\, e^{i(\varphi_{ca}+\pi+\Delta\omega_{ca}\tau)}. \end{aligned} \tag{5.19}$$

From experimental data, one also analyses the absorption lineshape of $sp_{2,3+}$, thus it would be helpful to write out the formula for state c:

$$\begin{aligned} a^c_{\text{mod}}(\tau) &= A^c_{\text{mod}}(\tau)\, e^{i\varphi^c_{\text{mod}}(\tau)} \\ &= a_{gc} + a_{cb} + a_{ac}(\tau). \end{aligned} \tag{5.20}$$

The different interaction pathways that contribute to state $|c\rangle$ are:

$$\begin{aligned} &a_{gc} : |g\rangle \rightarrow |c\rangle \\ &a_{cb} : |g\rangle \rightarrow |c\rangle \rightarrow |b\rangle \rightarrow |c\rangle \\ &a_{ac} : |g\rangle \rightarrow |a\rangle \rightarrow |b\rangle \rightarrow |c\rangle \end{aligned} \tag{5.21}$$

The delay-dependent term reads

$$\begin{aligned} a_{ac}(\tau) &= A_{ac}\, e^{i(\varphi_{ac}+\pi+\Delta\omega_{ac}\tau)} \\ &\propto -a_{ga}\, E^2_{NIR}\, \mu_{ab}\, \mu_{bc}\, e^{i\Delta\omega_{ac}\tau}. \end{aligned} \tag{5.22}$$

Similarly, the dipole response of $|c\rangle$ and its absorption cross-section depends on the coefficient

$$\begin{aligned} A^c_{\text{mod}}(\tau)e^{i\varphi^c_{\text{mod}}(\tau)} &= A_{gc}e^{i\varphi_{gc}} + A_{cb}e^{i(\varphi_{cb}+\pi)} \\ &\quad + A_{ac}\, e^{i(\varphi_{ac}+\pi+\Delta\omega_{ac}\tau)}. \end{aligned} \tag{5.23}$$

From the above equation, one sees the absorption spectrum $\sigma(\omega)$ varies with delay τ. Thus when taken the real and imaginary parts of $d_a(\omega)$ and plot in the complex plane as shown in Fig. 5.10 (a), it forms a circle around a fixed center varying with time delay. In Eq. 5.19, the first and second terms are π out of phase with each other and independent of τ, and the third term has constant amplitude A_{ca} while varying with the phase $\Delta\omega_{ca}$. The complex phase varies in opposite directions for state $2s2p$ and $sp_{2,3+}$ with respect to time delay, because the $\Delta\omega$ term for transition from one excited state to another and the other way around have opposite signs, meaning $\Delta\omega_{ca}(\tau)$ will become $-\Delta\omega_{ac}(\tau)$ in Eq. 5.19, thus data points will rotate in the opposite direction with respect to time delay (see Fig. 5.10(b)).

5.7 Delay-dependent phase

With the theoretical model, one can compare measured and simulated data to quantify the delay-dependent state-specific phases. It is most helpful to first plot the Fano fitted phase and

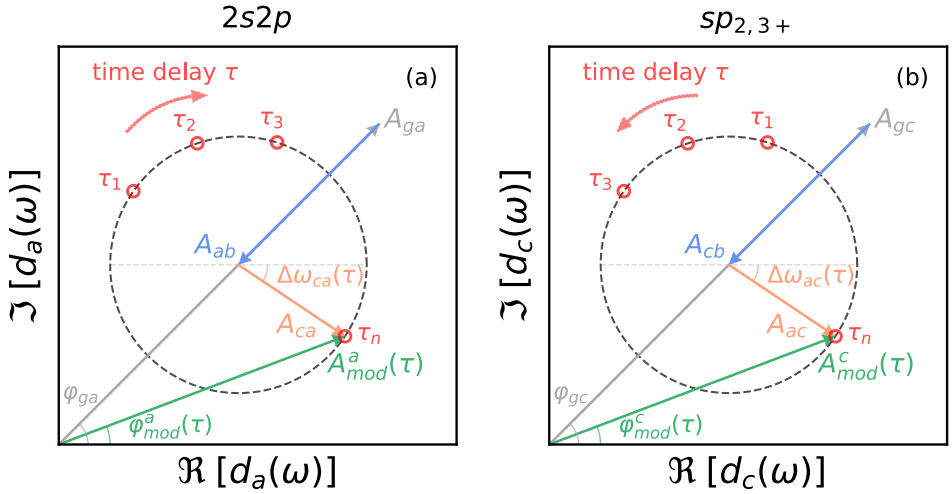

Figure 5.10: Graphical representation of the complex amplitude of the excited states in the complex plane, adapted from [112]. $|a\rangle = 2s2p$ resonantly couples to a dark intermediate state $|b\rangle = 2p^2$ and a coherently excited bright state $|c\rangle = sp_{2,3+}$. The contribution from the coherently excited bright state A_{ca} forms a circle varying with respect to time delay due to the energy difference between the states and their corresponding field-free time-dependent phase evolution. The coupling scheme is similar for $|c\rangle = sp_{2,3+}$.

amplitudes of simulated data over a large delay range to have a general impression. Fig. 5.11 shows the evolution of φ_{Fano} and A_{Fano} from -10 to 20 fs.

In [112], the complex phases and amplitudes of state $sp_{2,3+}$ were studied over a delay range of 1.2 fs (from delay 9.8 to 11 fs) corresponding to half a laser cycle for varying laser intensities, it was found for increasing intensity the radius and ellipticity also increases, while the overall shape over longer delay range was not mentioned. Plotted in Fig. 5.11, the complex phase rotates in opposite directions as discussed in the last paragraph, while their overall evolving trend shows a spiral shape. One can observe from Fig. 5.11 (a), the overall shape is elliptical with varying radii and the center point of rotation shifts in the plane, while in (b) the center shifts in a smaller range and its radius decreases with time delay. The center position is given by values a_{ga} and a_{gc} from 5.12, 5.20, which will be discussed later.

Both the measured and simulated data are discrete in time, therefore to apply the Fano phase formalism one fits the data points with an ellipse using least squares minimization based on [115], and then extracts the phases for comparison. Some of the fitted parameters are listed in the table below.

Fig. 5.12 plots the measured and simulated data from around 6 to 7 fs and their ellipsoidal fits, one can observe data points $2s2p$ and $sp_{2,3+}$ to rotate in opposite directions with delay. This delay range was chosen such that it is not in the time overlap between the NIR and XUV

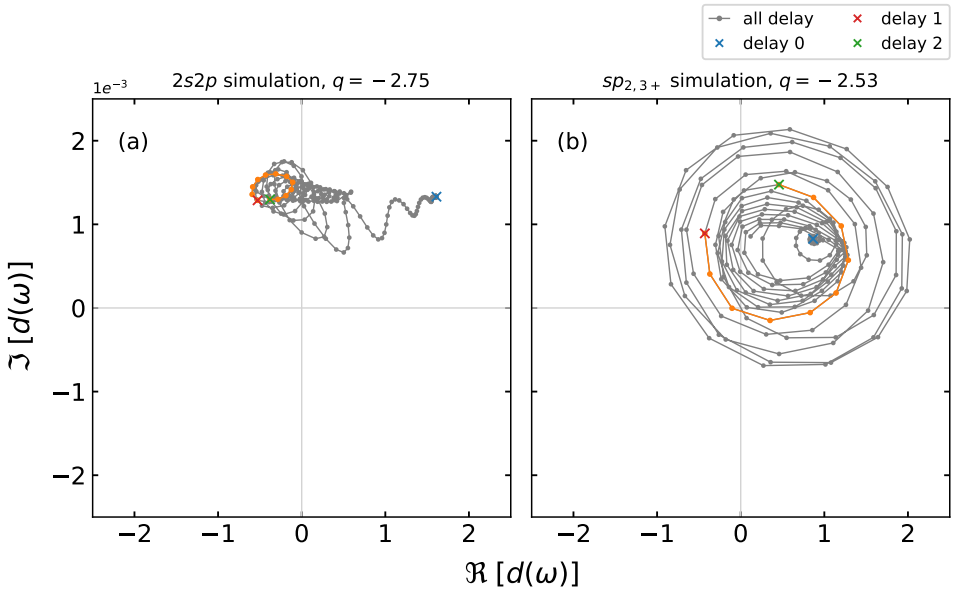

Figure 5.11: Spectral dipole amplitude and phases as a function of time delay from Fano lineshape fit of simulated resonant states. Each subplot represents a complex plane with aspect ratio 1. The grey dots show data from delay range -10 to 20 fs, and are connected with straight lines to better visualize the trend. The first delay data point -5 fs is marked with blue cross. Lines in orange selects a certain delay range (from delay 1 to delay 2) which will be further used to extract delay-dependent phases in the next section. (a) State $2s2p$, time delay ranges from 5.8 to 6.9 fs. (b) State $sp_{2,3+}$, time delay ranges from 6 to 7 fs.

state	center pos. $[x_c, iy_c]$	φ_{ga}	φ_{gc}
$2s2p$ measure.	$[7.3, -9.8i]$	$-53°$	–
$2s2p$ simu.	$[-3.6, 14.4i]$	$104°$	–
$sp_{2,3+}$ measure.	$[15.7, 5.1i]$	–	$18°$
$sp_{2,3+}$ simu.	$[4.0, 6.8i]$	–	$59°$

Table 5.3: Parameters extracted from ellipsoidal fits.

state		slope	displacement $\Delta\omega_{ca}$	displacement $\Delta\omega_{ac}$
$2s2p$	measurement	-5.20 rad/fs (3.42 eV)	1.028-1.120 rad 0.196-0.214 fs	-
	simulation	-5.22 rad/fs (3.44 eV)		-
$sp_{2,3+}$	measurement	5.71 rad/fs (3.75 eV)	-	0.502-0.208 rad 0.096-0.039 fs
	simulation	5.35 rad/fs (3.52 eV)	-	

Table 5.4: Parameters extracted from linear fit in Fig. 5.13.

pulse, also state $2s2p$ has a natural lifetime of 17 fs and the state will not be significantly depleted on the timescale of the laser-driven two-electron dynamics. In subplots (a) and (b), one can see the two ellipses locate in different quadrants of the complex plane, nevertheless, the value of interest is $\Delta\omega_{ca/ac}(\tau)$. From the ellipsoidal fit, one can extract the center, width, height, and angle parameters to obtain the dipole phase information. Data points from the fit on the ellipse $[x_n, i\, y_n]$ and center point $[x_c, i\, y_c]$ is used to calculate the angle in the complex plane

$$\Delta\omega = \text{angle}\left[(x_n + i\, y_n) - (x_c + i\, y_c))\right]. \tag{5.24}$$

In the end, $\Delta\omega_{ca/ac}(\tau)$ is plotted as a function of time delay for both excited states (see Fig. 5.13), then an linear fit is performed to extract the difference in phase. Parameters extracted from the fit are the slope and vertical displacement in phase, the difference in phase is calculated between delay 6 and 7 fs, listed in Table 5.3 below

The slope in rad/fs can be converted into energy by multiplying the Planck's constant, which theoretically should equal to the energy difference between the two coupling bright states 3.51 eV. One observes the difference in phase between simulation and measurement for $2s2p$ is around 0.2 fs while for $sp_{2,3+}$ is 0.1 fs or lower. The signs of their slopes are opposite of each other because of the rotating direction of data points as shown in Fig. 5.10.

To discuss the phase $\Delta\omega_{ca/ac}(\tau)$ and center position, one could return to the formula that describes the complex expansion coefficients $a^a_{\text{mod}}(\tau)$ and $a^c_{\text{mod}}(\tau)$. The delay-dependent term is only $\Delta\omega_{ca/ac}(\tau)$, however Fig. 5.13 indicates a delay-dependent translation or rotation of the data points as a whole. From the formula, the remaining parameters that are determined by experiment are $d_{gc/gc}$ and E_{NIR}, thus two other simulations with different parameters are performed (see Fig. 5.14), and following the same analysis procedure, their spectral amplitude and phase are plotted in the complex plane in Fig. 5.15 and Fig. 5.16).

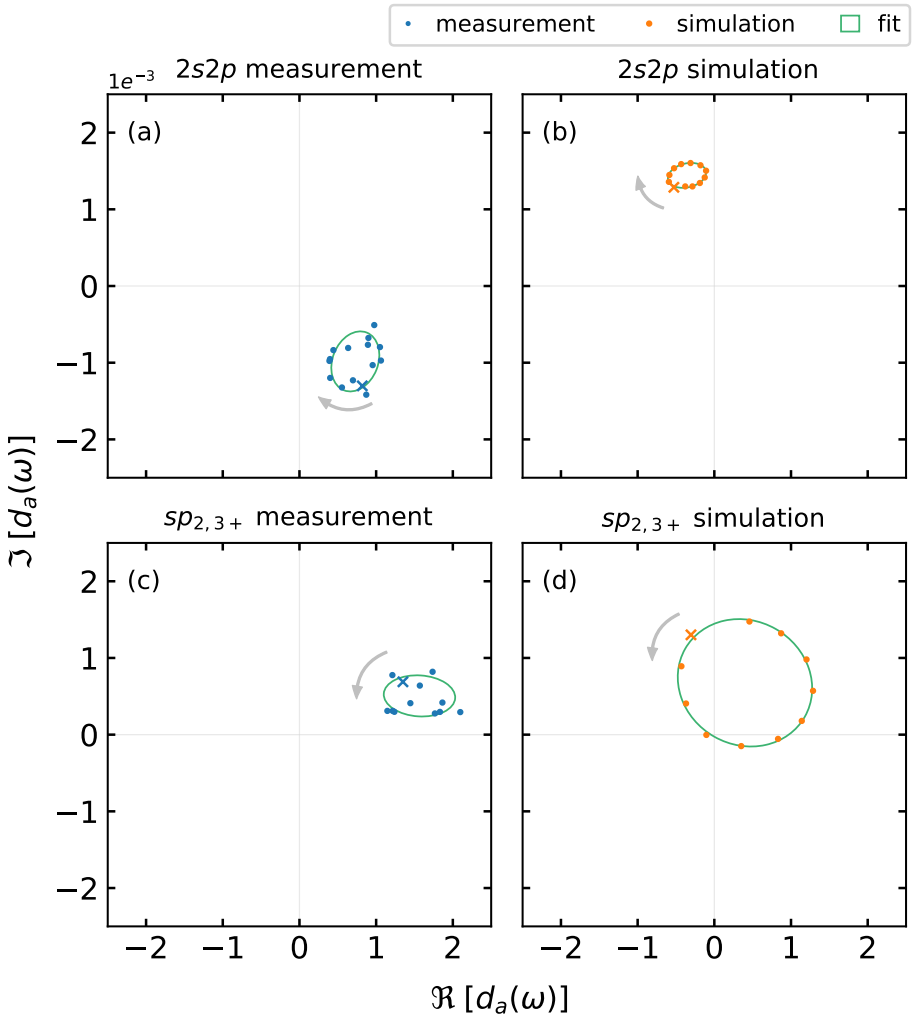

Figure 5.12: Spectral dipole amplitudes and phases as a function of time delay. Each subplot shows the evolution of the dipole moment with its real and imaginary part plotted in the complex plane with aspect ratio 1, the horizontal and vertical grey line marks y=0 and x=0. The dots show (a), (c) measured and (b), (d) simulated data covering delay range of around half the laser cycle, green lines are ellipsoidal fits, the center point and the phase with respect to the center point are extracted from the fit as a function of delay. The first data point of each subplot is highlighted with a cross marker, the order of the subsequent delay dependent complex values are indicated by the grey arrows. In (a) and (b), the delay ranges from 5.8 to 7 fs, in (c) delay ranges from 6 to 7 fs, and in (d) delay ranges from 6.15 to 7.1 fs.

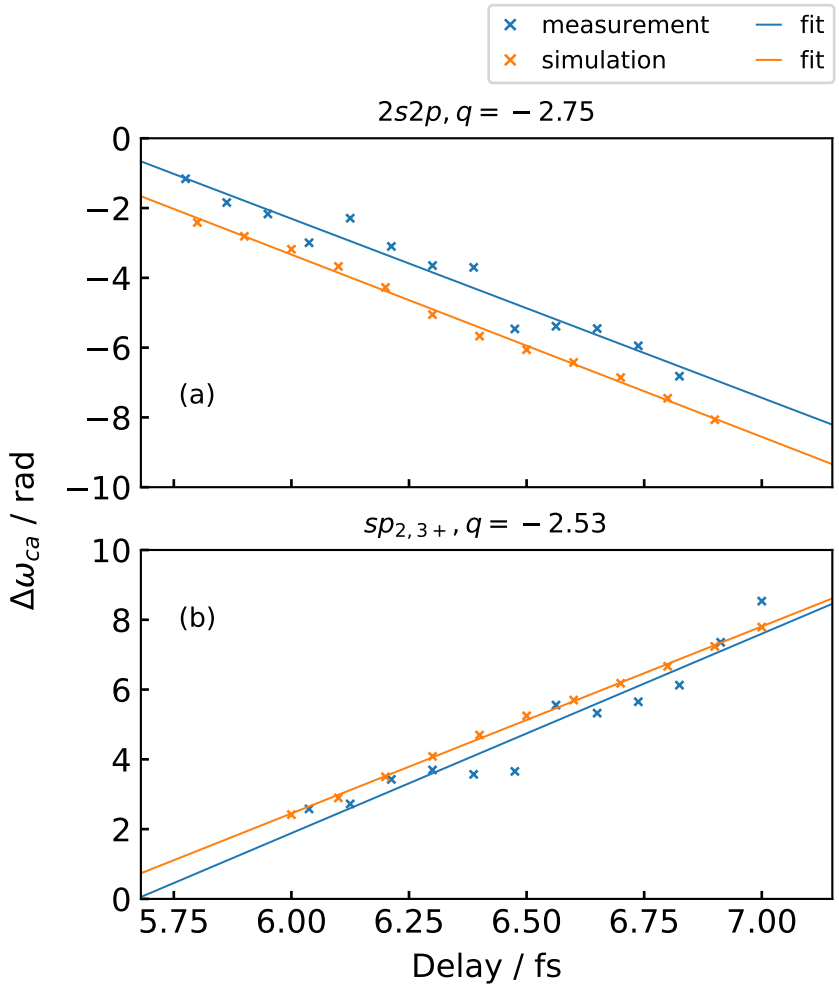

Figure 5.13: Spectral phase as a function of time delay. The data points are presented in cross markers, with their respective linear fits in the same color. (a) and (b) have opposite slopes because the phase rotates in opposite directions in Fig. 5.10. The offset of linear fit between measurement and simulation are listed in Table 5.3. Between delay 6-7 fs, the offset of $2s2p$ is 196 to 214 as, while for $sp_{2,3+}$ is 39 to 96 as.

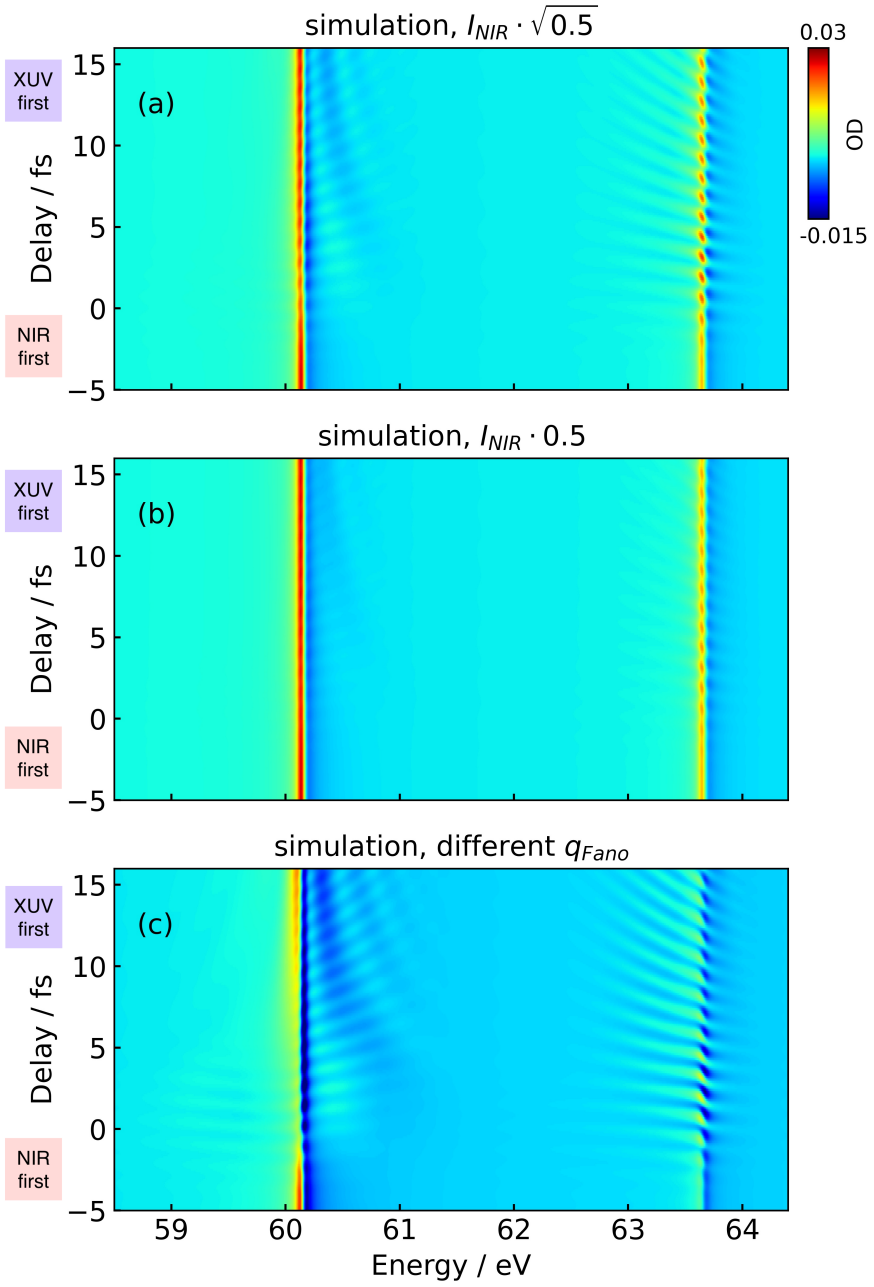

Figure 5.14: Simulated spectra of the helium doubly excited states as a function of time delay, they have different simulation parameters. (a) and (b) have smaller NIR intensity. One can see the lineshape of $2s2p$ is less modulated at time overlap. (c) The field-free Fano parameter is set to $q = -1.7$ and $q = -1$ for $2s2p$ and $sp_{2,3+}$, respectively.

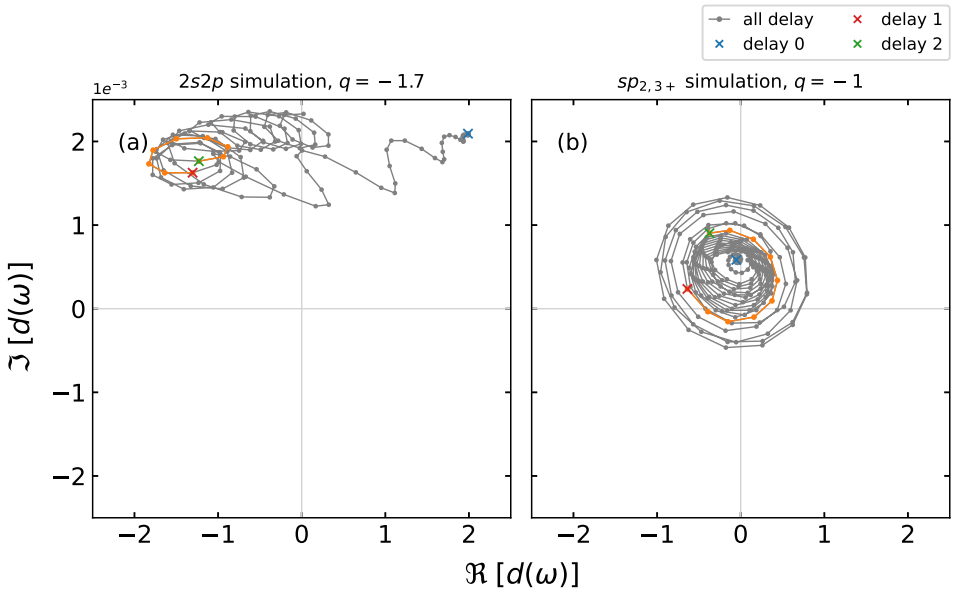

Figure 5.15: Spectral dipole amplitude and phases as a function of time delay from Fano lineshape fit of simulated resonant states, the Fano q parameters are different compared to Fig. 5.13, labeled in the title of each subplot. Each subplot represents a complex plane with aspect ratio 1. The grey dots show data from delay range -10 to 20 fs, and are connected with straight lines to better visualize the trend. The first delay data point -5 fs is marked with a blue cross. Lines in orange selects a certain delay range (from delay 1 to delay 2) which will be further used to extract delay-dependent phases in the next section. (a), (c) State $2s2p$, time delay ranges from 5.8 to 7 fs. (b), (d) State $sp_{2,3+}$, time delay ranges from 6 to 7.1 fs.

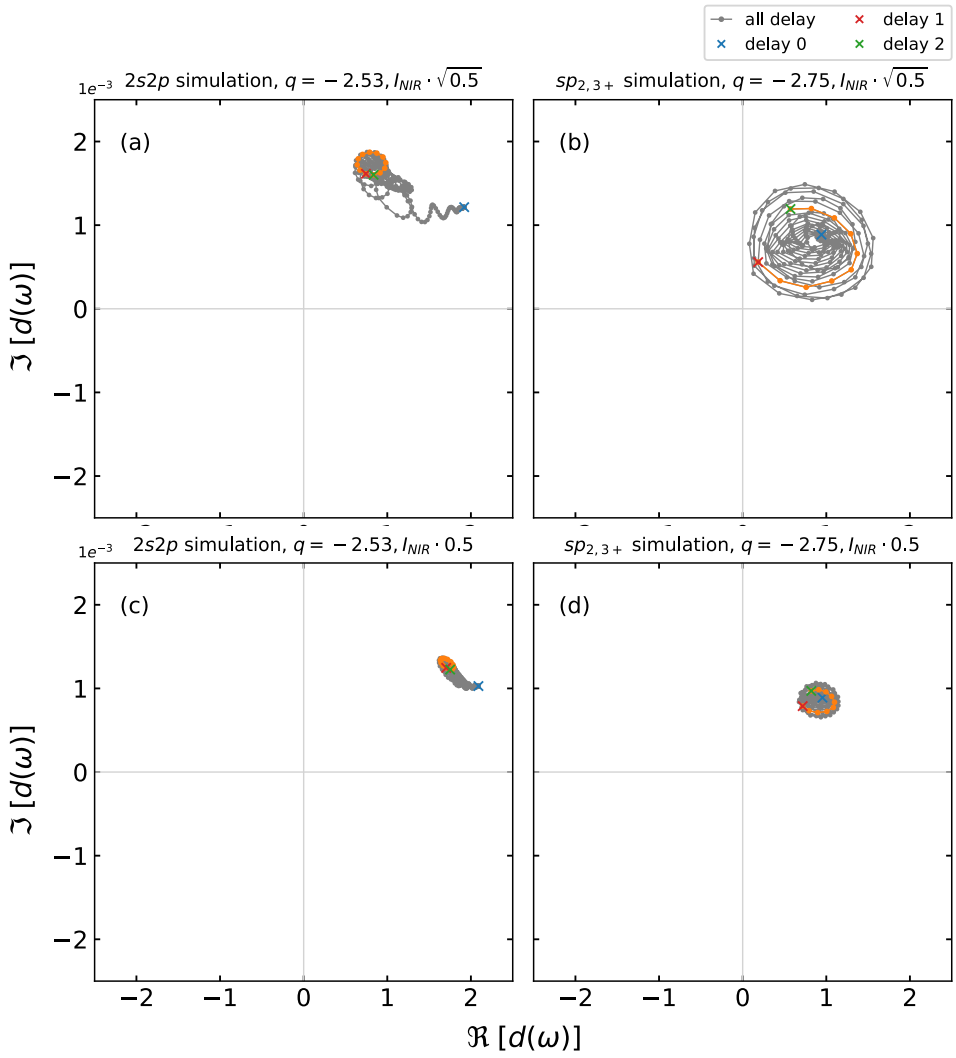

Figure 5.16: Spectral dipole amplitude and phases as a function of time delay from Fano lineshape fit of simulated resonant states, the NIR intensities are different compared to Fig. 5.13, labeled in the title of each subplot. Each subplot represents a complex plane with aspect ratio 1. The grey dots show data from delay range -10 to 20 fs, and are connected with straight lines to better visualize the trend. The first delay data point -5 fs is marked with a blue cross. Lines in orange selects a certain delay range (from delay 1 to delay 2) which will be further used to extract delay-dependent phases in the next section. (a), (c) State $2s2p$, time delay ranges from 5.8 to 7 fs. (b), (d) State $sp_{2,3+}$, time delay ranges from 6 to 7.1 fs.

The simulation with different $d_{gc/ga}$, reflected in the Fano q parameter in Eq. 2.40, which is related to the dipole matrix elements for ground to excited states and ground to continuum states, and the configuration matrix elements. The new q parameters obtained from fitting the simulated spectrum are -1.7 and -1 for $2s2p$ and $sp_{2,3+}$, respectively. The other simulation still used literature q values, while the NIR intensity is multiplied by $\sqrt{0.5}$ and 0.5.

The newly generated figures can be discussed alongside Fig. 5.11 in mainly two aspects, the phase of interest $\Delta\omega(\tau)$ and the phase $\varphi_{ga/gc}$. The first data point is the blue cross marker, for instance its amplitude in vector representation is equal to $\vec{A_{ga}} - \vec{A_{ab}}$, and by observation it depends more on dipole matrix element μ_{ga} rather than I_{NIR}, while its phase changes more with I_{NIR}. At large negative delays, the coupling starts with only XUV excitation, then going over time overlap the absorption lineshapes will become strongly modulated, which is reflected in the data points after the blue marker. Also, it is reasonable that with decreasing I_{NIR}, the absorption lineshape is less modulated, it can be seen in the plots with smaller NIR intensity the range of distribution of data points are more convergent to the blue marker. The phase φ_{ga} varies much more with delay compared to φ_{gc} in all four simulations, for $sp_{2,3+}$ the center of different circles almost remain at the same phase.

From the position of the red cross markers, which is the first data point of delay range 6-7 fs, one could already see the rotation of the ellipse formed by the orange data points is different, this change is reflected in Fig. 5.17. The displacement of the measured and simulated linear fits for $2s2p$ is on the order of 1 rad, while for $sp_{2,3+}$ it is below 0.5 rad.

In the delay-dependent complex coefficients $a_{ca}(\tau)$ and $a_{ac}(\tau)$ (Eqs. 5.16,5.22), the terms $E_{NIR}^2\,\mu_{ab}\mu_{bc}$ are the same, while $a_{ca}(\tau)$ contains the term $a_{gc} \propto |\mu_{gc}|^2$ and $a_{ac}(\tau)$ contains $a_{ga} \propto |\mu_{ga}|^2$. Therefore, in simulations with different q_{Fano}, for state $sp_{2,3+}$ the value changed from -2.53 to -1, using 5.6 to convert to radius is

$$\varphi = 2\arg(2.53 - 1 - i) = 1.15\,\text{rad}. \tag{5.25}$$

This estimation could be the reason of the observed displacement between the linear fit for the case of different Fano q parameter (orange and purple line in Fig. 5.17 (a)).

For the reconstruction of the full temporal dipole response one could refer to the method in [106], where the amplitude and phase of the time-dependent dipole moment of isolated resonances are reconstructed from a single absorption spectrum, with certain constrains such as the initial excitation pulse is much shorter than the system's dynamics. They also investigated different NIR intensities from the weak perturbative regime to strong coupling and strong-field ionization of the autoionizing states.

The phase off-set of fitted lines of $2s2p$ in Fig. 5.13 can be explained by parameters that are chosen in the simulation. We have confirmed this with simulations of different Fano q and NIR intensities. Therefore, state $sp_{2,3+}$ which is less dependent on simulation parameters, is more reliable to quantify the precision of our simultaneous measurement, which is below 100 as.

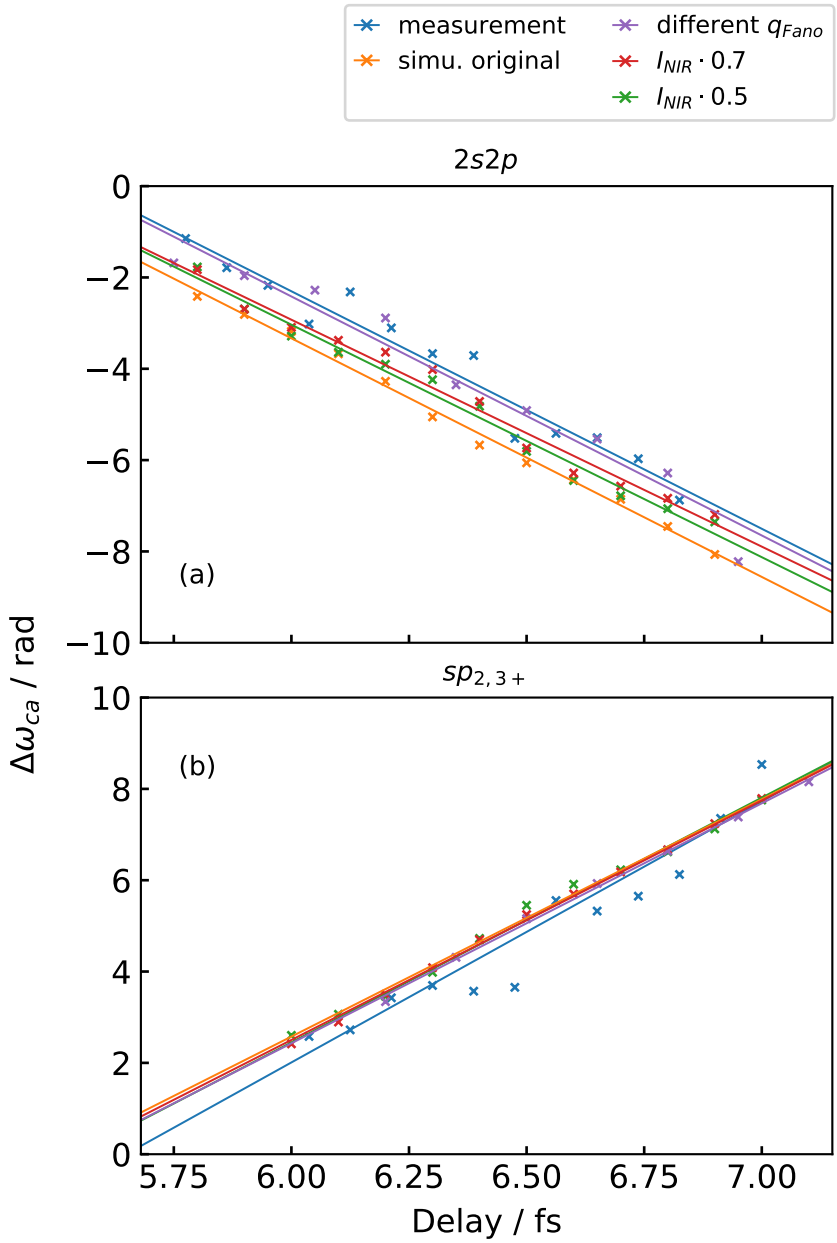

Figure 5.17: Spectral phase as a function of time delay. The phase of $2s2p$ and $sp_{2,3+}$ are compared to simulations with different Fano q and NIR intensities. The data points are presented in cross markers, with their respective linear fits in the same color.

Chapter 6

Conclusion and outlook

The general theme of this thesis revolves around the interferometric observation, understanding, and control of ultrafast electron quantum dynamics. The coupling dynamics within correlated two-electron states in helium were experimentally measured and modeled. We have shown a novel beamline for the simultaneous measurement of both the resonant photoabsorption spectra and streaked photoelectrons in the same gas target. With the attosecond-precision simultaneous measurements, we are able to access delay-calibrated information from the obtained data, which in turn can be applied to enhance our understanding of the two-electron dynamics in external strong fields.

On the experimental side, to make the simultaneous transient absorption and streaking measurement possible, some upgrades were applied to the setup. One is the installation of a new electron time-of-flight spectrometer. Also, with our newly designed and fabricated target cell and time-of-flight tube entrance piece the measurement conditions of both spectroscopic methods are fulfilled, making it possible to operate the electron detector while recording absorption spectra with sufficient signal. To the best of my knowledge, this is the first time such a setup has been realized. For the streaking experiment, it is important to stabilize the carrier-envelope phase (CEP) of the laser, thus, an optical setup to measure and stabilize the CEP inside the amplifier was installed, it provides access to control the CEP within a standard deviation of 200 mrad.

With the experimental methods, we are able to calibrate the absolute time-delay zero of the measurement. It is realized through the streaking measurement, with retrieval algorithms one can reconstruct the time delay zero and the full temporal profile of the interacting XUV and NIR electric fields, from which one can calibrate the absolute time-delay zero in the measured absorption spectra. The algorithm implemented in this analysis is ePIE [79], and simulations were performed to test its robustness to noise.

To understand the dynamics in absorption spectra, a numerical model based on a few-level TDSE simulation of the relevant states is conducted. Instead of simulated XUV and NIR pulses, we are able to directly use the pulses retrieved from streaking measurement for the simulation, as well as the retrieved time-delay axis. Usually, the time-delay calibration of transient absorption spectra is done with separate reference measurements, for instance, model

the Autler-Townes splitting from an intensity scan [83, 99], or phase changes in highly excited states due to ponderomotive shifts in the NIR field [88]. We are able to retrieve the delay axis for transient absorption in the same measurement. Within the numerical model, one can selectively change the signs of dipole matrix elements between bound states, which in turn may result in different absorption resonance lineshapes. By taking delay-dependent lineouts of the resonant states, one observes a π phase shift of the oscillation. However, in theoretical calculations, the signs of the transition dipole elements are usually calculated for individual dipole transitions are non-uniform [109]. By comparing the lineouts of the resonant states between the measured and simulated absorption spectra, it was possible to quantify the signs of the transition dipole matrix elements for the laser-coupled autoionizing states $2s2p - 2p^2$ and $2p^2 - sp_{2,3+}$ to be opposite of each other.

Due to the interferometric principle of transient absorption spectroscopy, the measurement is sensitive to the amplitude and phase of the atomic dipole response. We applied the Fano phase formalism from [112] to the resonant coupling of the two states, and extracted the amplitude and phase modifications by the NIR laser from different quantum pathways that are involved in the coupling dynamics of the autoionizing states. Higher precision measurements and analysis of the different phase contribution will help to better understand the laser coupling of autoionizing states. And with the Fano-phase approach, we have shown the difference between experiment and simulation of the spectral phase of state $sp_{2,3+}$ is below 100 attoseconds.

Further on, one could experimentally measure the exact buildup time of the Autler-Townes splitting in gas targets which theoretically have been calculated to be on the order of few femtoseconds for a few-cycle pulse [116]. With this novel experimental method, one could make full use of the spectral and temporal information, and extract information from the lineshape, time-dependent phase and amplitude induced by resonant laser coupling to study strong-field-induced dynamics, thus opening the possibility for a new class of attosecond experiments in gas targets.

Appendix A

Atomic units

Atomic units (a.u.) are uses in this thesis, it is a system of natural units commonly used in atomic, molecular, and quantum physics to simplify the complexity of calculations and express the physical quantities and equations in a dimensionless manner. In atomic units, fundamental physical constants are set to unity, for instance, $m_e = e = \hbar = a_0 = 1/(4\pi\varepsilon_0) = 1$. Table A.1 gives the basic physical quantities, adapted from [88].

Quantity	Unit	Value
Mass	Electron mass m_e	9.109×10^{-31} kg
Charge	Elementary charge e	1.602×10^{-19} C
Angular momentum	Reduced Planck constant $\hbar$	1.055×10^{-34} Js
Length	First Bohr radius a_0	5.292×10^{-11} m
Velocity	$v_0 = \alpha c_0$	2.188×10^{6} ms^{-1}
Momentum	$p_0 = m_e v_0$	1.993×10^{-24} kgms^{-1}
Time	a_0/v_0	2.419×10^{-17} s
Energy	$E_h = \frac{e^2}{4\pi\varepsilon_0\alpha_0} = \alpha^2 m_e c_0^2$	27.2114 eV
Electric potential	$E_h/e = \frac{e}{4\pi\varepsilon_0\alpha_0}$	27.2114 V
Electric field	$E_0 = \frac{e}{4\pi\varepsilon_0\alpha_0^2}$	5.142×10^{11} Vm^{-1}
Intensity	$I_0 = \frac{1}{2}\varepsilon_0 c_0 E_0^2$	3.509×10^{16} Wcm^{-2}

Table A.1: Relationship between physical quantities in the system of atomic units and the SI.

Bibliography

[1]E. Muybridge, "Sallie gardner at a gallop (the horse in motion)", San Francisco Museum (1878).

[2]A. J. DeMaria, D. A. Stetser, and H.Heynau, "Self mode-locking of lasers with saturable absorbers.", Appl. Phys. Lett. **8** (1966).

[3]U. Keller, G. W.'tHooft, W. H. Knox, and J. E. Cunningham, "Femtosecond pulses from a continu- ously self-starting passively mode-locked ti:sapphire laser", Opt. Lett. **16** (1991).

[4]A. Baltuska, T. Udem, M. Uiberacker, M. Hentschel, E. Goulielmakis, C. Gohle, R. Holzwarth, V. S. Yakovlev, A. Scrinzi, T. W. Hänsch, and F. Krausz, "Attosecond control of electronic processes by intense light fields", Nature **421** (2003).

[5]A. Wirth, M. T. Hassan, I. Grguras, J. Gagnon, A. Moulet, T. Luu, S. Pabst, R. Santra, Z. A. Alahmed, A. M. Azzeer, V. S. Yakovlev, V. Pervak, F. Krausz, and E. Goulielmakis, "Synthesized light transients", Science **334** (2011).

[6]E. Goulielmakis, M. Schultze, M. Hofstetter, V. S. Yakovlev, J. Gagnon, M. Uiberacker, A. L. Aquila, E. M. Gullikson, D. T. Attwood, R. Kienberger, F. Krausz, and U. Kleineberg, "Single-cycle nonlinear optics", Science **320** (2008).

[7]A. McPherson, G. Gibson, H. Jara, U. Johann, T. S. Luk, I. A. McIntyre, K. Boyer, and C. K. Rhodes, "Studies of multiphoton production of vacuum-ultraviolet radiation in the rare gases", J. Opt. Soc. Am. B **4** (1987).

[8]M. Hentschel, R. Kienberger, C. Spielmann, G. A. Reider, N. Milosevic, T. Brabec, P. Corkum, U. Heinzmann, M. Drescher, and F. Krausz, "Attosecond metrology", Nature **414** (2001).

[9]P. M. Paul, E. S. Toma, P. Breger, G. Mullot, F. Auge, P. Balcou, H. G. Muller, and P. Agostini, "Observation of a train of attosecond pulses from high harmonic generation", Science **292** (2001).

[10]M. Drescher, M. Hentschel, R. Kienberger, M. Uiberacker, V. Yakovlev, A. Scrinzi, T. Westerwalbesloh, U. Kleineberg, U. Heinzmann, and F. Krausz, "Time-resolved atomic inner-shell spectroscopy", Nature **419** (2002).

[11]M. Uiberacker, T. Uphues, M. Schultze, A. J. Verhoef, V. Yakovlev, M. F. Kling, J. Rauschenberger, N. M. Kabachnik, H. Schröder, M. Lezius, K. L. Kompa, H.-G. Muller, M. J. J. Vrakking, S. Hendel, U. Kleineberg, U. Heinzmann, M. Drescher, and F. Krausz, "Attosecond real-time observation of electron tunnelling in atoms", Nature **446** (2007).

[12]E. Goulielmakis, Z.-H. Loh, A. Wirth, R. Santra, N. Rohringer, V. S. Yakovlev, S. Zherebtsov, T. Pfeifer, A. M. Azzeer, M. F. Kling, S. R. Leone, and F. Krausz, "Real-time observation of valence electron motion", Nature **466** (2010).

[13]E. R. Warrick, W. Cao, D. M. Neumark, and S. R. Leone, "Probing the dynamics of rydberg and valence states of molecular nitrogen with attosecond transient absorption spectroscopy", J. Phys. Chem. A **120** (2016).

[14]M. Reduzzi, C. Feng, W. C. Chu, A. Dubrouil, F. Calegari, M. Nisoli, F. Frassetto, L. Poletto, C. D. Lin, and G. Sansone, "Attosecond absorption spectroscopy in molecules", CLEO (2013).

[15]P. Birk, "Time-dependent strong-field effects in atoms and molecules observed by attosecond transient absorption spectroscopy", PhD thesis (Heidelberg University, 2016).

[16]A. L. Cavalieri, N. Müller, T. Uphues, V. S. Yakovlev, A. Baltuška, B. Horvath, B. Schmidt, L. Blümel, R. Holzwarth, S. Hendel, M. Drescher, U. Kleineberg, P. M. Echenique, R. Kienberger, F. Krausz, and U. Heinzmann, "Attosecond spectroscopy in condensed matter", Nature **449** (2007).

[17]B. Abbott, "Observation of gravitational waves from a binary black hole merger", Phys. Rev. Lett. **116** (2016).

[18]J. Fourier, *Théorie analytique de la chaleur* (Cambridge University Press, 2010).

[19]J. C. Diels and W. Rudolph, *Ultrashort laser pulse phenomena* (Academic Press, 2006).

[20]http://www.nist.gov/pml/data/periodic.cfm.

[21]L. V. Keldysh, "Ionization in field of a strong electromagnetic wave", Sov. Phys. JETP **20** (1965).

[22]A. M. Zheltikov, "Keldysh parameter, photoionization adiabaticity, and the tunneling time", Phys. Rev. A **94** (2016).

[23]T. Popmintchev, M. C. Chen, D. Popmintchev, P. Arpin, S. Brown, S. Alisauskas, G. Andriukaitis, T. Balciunas, O. D. Mücke, A. Pugzlys, A. Baltuska, B. Shim, S. E. Schrauth, A. Gaeta, C. Hernández-García, L. Plaja, A. Becker, A. Jaron-Becker, M. M. Murnane, and H. C. Kapteyn, "Bright coherent ultrahigh harmonics in the kev x-ray regime from mid-infrared femtosecond lasers", Science **336** (2012).

[24]T. Gaumnitz, A. Jain, Y. Pertot, M. Huppert, I. Jordan, F. Ardana-Lamas, and H. J. Wörner, "Streaking of 43-attosecond soft-x-ray pulses generated by a passively cep-stable mid-infrared driver", Opt. Express **25** (2017).

[25]J. Li, X. Ren, Y. Yin, K. Zhao, A. Chew, Y. Cheng, E. Cunningham, Y. Wang, S. Hu, Y. Wu, M. Chini, and Z. Chang, "53-attosecond x-ray pulses reach the carbon k-edge", Nat. Commun. **8** (2017).

[26]K. Zhao, Q. Zhang, M. Chini, Y. Wu, X. Wang, and Z. Chang, "Tailoring a 67 attosecond pulse through advantageous phase-mismatch", Opt. Lett. **37** (2012).

[27]T. Brabe, *Strong field laser physics* (Springer, 2008).

[28]P. Agostini and L. F. DiMauro, "The physics of attosecond light pulses", Rep. Prog. Phys. **67** (2004).

[29]F. Krausz and M. Ivanov., "Attosecond physics", Rev. Mod. Phys. **81** (2009).

[30]P. Corkum, "Plasma perspective on strong field multiphoton ionization", Phys. Rev. Lett. **81**, 163–234 (1993).

[31]D. J. Tannor, "Introduction to quantum mechanics: a time-dependent perspective", University Science Books (2003).

[32]B. Bransdenand and C. Joachain, *Physics of atoms and molecules*, second edition (Pearson Education, 2003).

[33]M. Domke, K. Schulz, G. Remmers, G. Kaindl, and D. Wintgen, "High-resolution study of $^1P^o$ double-excitation states in helium", Phys. Rev. A (1996).

[34]H. Klar, *Fundamentals of laser interactions* (Springer Berlin / Heidelberg, 1985).

[35]J. W. Cooper, U. Fano, and F. Prats, "Classification of two-electron excitation levels of helium", Phys. Rev. Lett. **10** (1963).

[36]U. Fano, "Effects of configuration interaction on intensities and phase shifts", Phys. Rev. A (1961).

[37]C. Ott, A. Kaldun, P. Raith, K. Meyer, M. Laux, J. Evers, C. Keitel, C. Greene, and T. Pfeifer, "Lorentz meets fano in spectral line shapes: a universal phase and its laser control", Science **340** (2013).

[38]J. Itatani, F. Quéré, G. L. Yudin, M. Y. Ivanov, F. Krausz, and P. B. Corkum, "Attosecond streak camera", Phys. Rev. Lett. **88** (2002).

[39]M. Kitzler, N. Milosevic, A. Scrinzi, F. Krausz, and T. Brabec, "Quantum theory of attosecond xuv pulse measurement by laser dressed photoionization", Phys. Rev. Lett. **88** (2002).

[40]V. S. Yakovlev, F. Bammer, and A. Scrinzi, "Attosecond streaking measurements", Journal of Modern Optics **52**, 2–3 (2005).

[41]Z. Chang, *Fundamantals of attosecond optics* (CRC Press, 2011).

[42]M. Chini, S. Gilbertson, S. Khan, and Z. Chang, "Characterizing ultrabroadband attosecond lasers", Opt. Exp. **18** (2010).

[43]M. Chini, K. Zhao, and Z. Chang, "The generation, characterization and applications of broadband isolated attosecond pulses", Nature Photonics **8** (2010).

[44]J. Gagnon, E. Goulielmakis, and V. S. Yakovlev, "The accurate frog characterization of attosecond pulses from streaking measurements", Appl. Phys. B **92** (2008).

[45]R. Kienberger, E. Goulielmakis, M. Uiberacker, A. Baltuska, V. Yakovlev, F. Bammer, A. Scrinzi, T. Westerwalbesloh, U. Kleineberg, U. Heinzmann, M. Drescher, and F. Krausz, "Atomic transient recorder", Nature **427** (2004).

[46]F. Lücking, A. Assion, A. Apolonski, F. Krausz, and G. Steinmeye, "Long-term carrier-envelope-phase-stable few-cycle pulses by use of the feed-forward method", Optics Letters **37** (2012).

[47]D. Strickland and G. Mourou, "Compression of amplified chirped optical pulses", Optics Communications **56**, 219–221 (1985).

[48]D. J. Kane and R. Trebino, "Single-shot measurement of the intensity and phase of an arbitrary ultrashort pulse by using frequency-resolved optical gating", Opt. Lett. **18** (1993).

[49]C. Iaconis and I. A. Walmsley, "Spectral phase interferometry for direct electric-field reconstruction of ultrashort optical pulses", Opt. Lett. **23** (1998).

[50]K. W. DeLong and R. Trebino, "Improved ultrashort pulse-retrieval algorithm for frequency-resolved optical gating", JOSA A **11**, 2429–2437 (1994).

[51]J. W. Nicholson, F. G. Omenetto, D. . Funk, and A. J. Taylor, "Evolving frogs: phase retrieval from frequency-resolved optical gating measurements by use of genetic algorithms", Optics Letters **24**, 490 (1999).

[52]V. Stooß, M. Hartmann, P. Birk, G. D. Borisova, T. Ding, A. Blättermann, C. Ott, and T. Pfeifer, "Xuv-beamline for attosecond transient absorption measurements featuring a broadband common beam-path time-delay unit and in situ reference spectrometer for high stability and sensitivity", Review of Scientific Instruments **90** (2019).

[53]C. Lemell, X. M. Tong, F. Krausz, and J. Burgdörfer, "Electron emission from metal surfaces by ultrashort pulses: determination of the carrier-envelope phase", Phys. Rev. Lett. **90** (2003).

[54]C. Li, E. Moon, H. Mashiko, H. Wang, C. Nakamura, J. Tackett, and Z. Chang, "Mechanism of phase-energy coupling in f-to-2f interferometry", Appl. Opt. **48** (2009).

[55]R. López-Martens, J. Mauritsson, P. Johnsson, and A. L'Huillier, "Time-resolved ellipticity gating of high-order harmonic emission", Phys. Rev. A **69** (2004).

[56]O. Tcherbakoff, E. Mével, D. Descamps, J. Plumridge, and E. Constant, "Time-gated high-order harmonic generation", Phys. Rev. A **68** (2003).

[57]K. S. Budil, P. Salières, M. D. Perry, and A. L'Huillier, "Influence of ellipticity on harmonic generation", Phys. Rev. A **48** (1993).

[58]M. KovaČev, Y. Mairesse, E. Priori, H. Merdji, O. Tcherbakoff, P. Monchicourt, P. Breger, E. Mével, E. Constant, P. Salières, B. Carré, and P. Agostini, "Temporal confinement of the harmonic emission through polarization gating", Eur. Phys. J. D **26** (2003).

[59]M. Abel, T. Pfeifer, P. Nagel, W. Boutu, M. Bell, C. Steiner, D. Neumark, and S. Leone, "Isolated attosecond pulses from ionization gating of high-harmonic emission", Chem. Phys. **366** (2009).

[60]https://henke.lbl.gov/optical$_c onstants/filter2.html$.

[61]T. Heldt, "Strong-field-driven electron dynamics near an ionization threshold", PhD thesis (Heldelberg University, 2020).

[62]D. Irimia, D. Dobrikov, R. Kortekaas, H. Voet, D. Ende, W. A. Groen, and M. Janssen, "A short pulse (7µs fwhm) and high repetition rate (dc-5khz) cantilever piezovalve for pulsed atomic and molecular beams", Rev. Sci. Instru. **80** (2009).

[63]U. Even, "The even-lavie valve as a source for high intensity supersonic beam", EPJ Techn Instrum **2** (2015).

[64]F. Herzog, "Design and implementation of a gas jet array for ultrafast time-resolved absorption spectroscopy", PhD thesis (Heidelberg University, 2019).

[65]D. Kennedy and S. Manson, "Photoionization of the noble gases: cross sections and angular distributions", Phys. Rev. A **5** (1927).

[66]X. Feng, S. Gilbertson, S. D. Khan, M. Chini, Y. Wu, K. Carnes, and Z. Chang, "Calibration of electron spectrometer resolution in attosecond streak camera", Opt. Express **18** (2010).

[67]https://www.kaesdorf.de.

[68]T. Tsuboi, E. Y. Xu, Y. K. Bae, and K. T. Gillen, "Magnetic bottle electron spectrometer using permanent magnets", Rev. Sci. Instrum. **59** (1988).

[69]A. Wirth, R. Santra, and E. Goulielmakis, "Real time tracing of valence-shell electronic coherences with attosecond transient absorption spectroscopy", Chem. Phys. **414** (2013).

[70]M. Lucchini, S. A. Sato, A. Ludwig, J. Herrmann, M. Volkov, L. Kasmi, Y. Shinohara, K. Yabana, L. Gallmann, and U. Keller, "Attosecond dynamical franz-keldysh effect in polycrystalline diamond", Science **353** (2016).

[71]M. Lucchini, S. A. Sato, F. Schlaepfer, K. Yabana, L. Gallmann, A. Rubio, and U. Keller, "Attosecond timing of the dynamical franz–keldysh effect", J. Phys.: Photonics **2** (2020).

[72]L. Kasmi, M. Lucchini, L. Castiglioni, P. Kliuiev, J. Osterwalder, M. Hengsberger, L. Gallmann, P. Krüger, and U. Keller, "Effective mass effect in attosecond electron transport", Optica **4** (2016).

[73]M. Volkov, S. A. Sato, F. Schlaepfer, L. Kasmi, N. Hartmann, M. Lucchini, L. Gallmann, A. Rubio, and U. Keller, "Attosecond screening dynamics mediated by electron localization in transition metals", Nat. Phys. **15** (2019).

[74]G. Lucarelli, M. Moio, G. Inzani, N. Fabris, L. Moscardi, F. Frassetto, L. Poletto, M. Nisoli, and M. Lucchini, "Novel beamline for attosecond transient reflection spectroscopy in a sequential two-foci geometry", Rev. Sci. Instrum. **91** (2020).

[75]M. Lewenstein, P. Balcou, M. Y. Ivanov, A. L'Huillier, and P. B. Corkum, "Theory of high-harmonic generation by low-frequency laser fields", Phys. Rev. A **49** (1994).

[76]M. Hentschel, R. Kienberger, C. Spielmann, G. A. Reider, N. Miloscvic, T. Brabec, P. Corkum, U. Heinzmann, M. Drescher, and F. Krausz, "Attosecond metrology", Nature **414** (2001).

[77]D. Kane, "Recent progress toward real-time measurement of ultrashort laser pulses", IEEE J. Quantum Electron **35** (1999).

[78]J. Gagnon, E. Goulielmakis, and V. S. Yakovleve, "The accurate frog characterization of attosecond pulses from streaking measurements", Appl. Phys. B **92** (2008).

[79]M. Lucchini, M. Brugmann, A. Ludwig, L. Gallmann, U. Keller, and T. Feurer, "Ptychographic reconstruction of attosecond pulses", Opt. Exp. **23** (2015).

[80]M. Lucchini and M. Nisoli, "Refined ptychographic reconstruction of attosecond pulses", Appl. Sci. **9** (2018).

[81]M. Murari, G. D. Lucarelli, M. Lucchini, and M. Nisoli, "Robustness of the epie algorithm for the complete characterization of femtosecond, extreme ultra-violet pulses", Opt. Exp. **23** (2020).

[82]S. Hu, M. Hartmann, A. Harth, C. Ott, and T. Pfeifer, "Noise effects and the impact of detector responses on the characterization of extreme ultraviolet attosecond pulses", Appl. Opt. **59** (2020).

[83]P. Birk, "The dipole response of an ionization threshold within ultrashort and strong fields", PhD thesis (Heidelberg University, 2020).

[84]H. Wang, M. Chini, S. Chen, C. Zhang, F. He, Y. Cheng, Y. Wu, U. Thumm, and Z. Chang, "Attosecond time-resolved autoionization of argon", Phys. Rev. Lett **105** (2010).

[85]S. L. Sorensen, T. Åberg, J. Tulkki, E. Rachlew-Källne, G. Sundström, and M. Kirm, "Argon 3s autoionization resonances", Phys. Rev. A **50** (1994).

[86]M. Hartmann, V. Stooß, P. Birk, G. Borisova, C. Ott, and T. Pfeifer, "Attosecond precision in delay measurements using transient absorption spectroscopy", Opt. Lett. **44** (2019).

[87]X. Wu, Z. Yang, Z. Shaofeng, X. Ma, J. Liu, and D. Ye, "Buildup time of autler-townes splitting in attosecond transient absorption spectroscopy", Phys. Rev. A **103** (2021).

[88]V. Stooß, "Strong-field spectroscopy: from absorption to time-resolved dynamics in strong fields", PhD thesis (Heldelberg University, 2020).

[89]A. Blättermann, C. Ott, A. Kaldun, T. Ding, V. Stooß, M. Laux, M. Rebholz, and T. Pfeifer, "In situ characterization of few-cycle laser pulses in transient absorption spectroscopy", Opt. Lett. **40** (2015).

[90]A. Blättermann, "Impulsive control of the atomic dipole response in the time and frequency domain", PhD thesis (Heidelberg University, 2016).

[91]J. Samson, Z. He, L. Yin, and G. Haddad, "Precision measurements of the absolute photoionization cross sections of he", J. Phys. B: At. Mol. Opt. Phys. **27** (1994).

[92]R. Santra, V. Yakovlev, T. Pfeifer, and Z. Loh, "Theory of attosecond transient absorption spectroscopy of strong-field-generated ions", Phys. Rev. A **83** (2011).

[93]B. H. Bransden and C. J. Joachain, *Physics of atoms and molecules* (Prentice Hall, Harlow; Munich, 2007).

[94]P. Lambropoulos and P. Zoller, "Autoionizing states in strong laser fields", Phys. Rev. A **24** (1981).

[95]P. J. Hicks and J. Comer, "Ejected electron spectroscopy of autoionizing states excited by low energy electron impact", J. Phys. B (1866).

[96]A. Bürgers, D. Wintgen, and J. M. Rost, "Highly doubly excited s states of the helium atom", J. Phys. B (1955).

[97]M. D. Feit, J. A. Fleck, and A. Steiger, "Solution of the schrödinger equation by a spectral method", J. Comput. Phys. (1982).

[98]C. Ott, A. Kaldun, P. Raith, K. Meyer, M. Laux, J. Evers, C. Keitel, C. Greene, and T. Pfeifer, "Lorentz meets fano in spectral line shapes: a universal phase and its laser control", Science (2013).

[99]C. Ott, "Attosecond multidimensional interferometry of single and two correlated electrons in atoms", PhD thesis (Heidelberg University, 2012).

[100]A. Kaldun, "Fano resonances in the time domain", PhD thesis (Heidelberg University, 2014).

[101]W. Chu and C. D. Lin, "Photoabsorption of attosecond xuv light pulses by two strongly laser-coupled autoionizing states", Phys. Rev. A **85** (2012).

[102]Z. H. Loh, C. H. Greene, and S. R. Leone, "Femtosecond induced transparency and absorption in the extreme ultraviolet by coherent coupling of the he 2s2p (1po) and 2p2 (1se) double excitation states with 800 nm light", Chem. Phys. **350** (2008).

[103]C. Ott, A. Kaldun, L. Argenti, P. Raith, K. Meyer, M. Laux, Y. Zhang, A. Blattermann, S. Hagstotz, T. Ding, R. Heck, J. M. ero, F. Martın, and T. Pfeifer, "Reconstruction and control of a time-dependent two-electron wave packet", Nature **516** (2014).

[104]G. Yuan, S. Jiang, Z. Wang, W. Hua, C. Yu, C. Jin, and R. Lu, "The role of transition dipole phase in atomic attosecond transient absorption from the multi-level model", Struct. Dyn. **6** (2019).

[105]Y. Kobayashi, D. M. Neumark, and S. R. Leone, "Theoretical analysis of the role of complex transition dipole phase in xuv transient-absorption probing of charge migration", Opt. Express **30** (2022).

[106]V. Stooß, S. M. Cavaletto, S. Donsa, A. Blättermann, P. Birk, C. H. Keitel, I. Brezinová, J. Burgdörfer, C. Ott, and T. Pfeifer, "Real-time reconstruction of the strong-field-driven dipole response", Phys. Rev. Lett. **121** (2018).

[107]M. Tarana and C. H. Greene, "Femtosecond transparency in the extreme-ultraviolet region", Phys. Rev. A **85** (2012).

[108]Y. Wang, S. Kar, and Y. K. Ho, "Dipole transition elements and oscillator strengths for the doubly excited states in the helium atom", Chem. Phys. Lett. **774** (2021).

[109]Y. S. Wang, S. Kar, and Y. K. Ho, "Dipole transition elements and oscillator strengths for the doubly excited states in the helium atom", Chem. Phys. Lett. **774** (2021).

[110]Z. Yan, "Calculations of magnetic moments for lithium-like ions", J. Phys. B: At. Mol. Opt. Phys. **35** (2002).

[111]M. Aymar, "Multichannel rydberg spectroscopy of complex atoms", Rev. of Mod. Phys. **68** (1996).

[112]E. Goulielmakis, M. Uiberacker, R. Kienberger, A. Baltuska, V. Yakovlev, A. Scrinzi, T. Westerwalbesloh, U. Kleineberg, U. Heinzmann, M. Drescher, and F. Krausz, "Extracting phase and amplitude modifications of laser-coupled fano resonances", Science **305** (2004).

[113]M. Chini, X. Wang, Y. Cheng, Y. Wu, D. Zhao, D. A. Telnov, S. I. Chu, and Z. Chang, "Sub-cycle oscillations in virtual states brought to light", Sci. Rep. **3** (2013).

[114]P. Mulser and S. Uryupin, "Ponderomotive potential and dynamical stark shift in multiphoton ionization", Phys. Rev. A **48** (1993).

[115]R. Halir and J. Flusser, "Numerically stable direct least squares fitting of ellipses", (1998).

[116]W. Chu and C. D. Lin, "Absorption and emission of single attosecond light pulses in an autoionizing gaseous medium dressed by a time-delayed control field", Phys. Rev. A **87** (2013).

Acknowledgements

At the end of this thesis, I would like to express my heartfelt gratitude to everyone who made this work possible. The accomplishments of a complex and time-consuming project such as a doctoral thesis are always linked to excellent teamwork, good supervision, and a pleasant working atmosphere and is never solely the achievement of an individual.

The most thanks go to my supervisors Christian Ott and Thomas Pfeifer for the opportunity to do my doctorate in this group. Thank you for all your support, the many instructive discussions and advice, and as well as always taking the time to help us when we have problems and questions.

I would like to thank Dr. Wolfgang Quint for being the second referee of this work.

Also, a thank you to the members of our group, especially to the people in the Interatto group: Gergana Borisova, Yu He, Maximilian Hartmann, Paul Birk, Carina da Costa Castanheira, for all the time spent, work done, and challenges overcame in the lab. Thanks to Yu He and Weiyu Zhang for proofreading this thesis and giving me comments.

Last but not least, a big thank you goes to my family for their love and support.

I thank for the things I've learned from my supervisors and colleagues, the time spent in this group, and the privilege of working alongside such wonderful people, thank you all.